Gas Permeation of Graphite Sealed Microcavities

A thesis submitted to the Technical University of Denmark
for the degree of Doctor of Philosophy
in the Department of Physics

By

Yanxin Liu

August 2022

Preface

This thesis is submitted in partial fulfillment of the requirement for the Ph.D. degree from the Technical University of Denmark (DTU). The work presented has been carried out in the ATOMICAR group at DTU Physics, from September 2019 to August 2022.

Acknowledgements

I would like to sincerely thank my supervisor Professor Peter Christian Kjærgaard Vesborg for his guidance, discussion, and inspiration. He taught me not only physics, but also many fun DIY skills, which benefits both my PhD project and my leisure DIY works. I would like also to express my appreciation to other members of the ATOMICAR group: Hjalte Rørbech Ambjørner, Zhongli Wang, Tobias Bonczyk, Edwin Dollekamp, and Lau Kaas. They provided fantastic samples to me for my measurements. Discussions with them were also very helpful in solving research problems. I would also like to thank my ATOMICAR colleagues and Anton Simon Bjørnlund for reading my thesis and giving me a lot of valuable comments and suggestions.

Students Chiara Libera Carnevale and Marcus Oliver Craig worked with me when they took their special courses and final project in the ATOMICAR group. They conducted excellent experiments investigating the leak rates of the sealed cavities. Yunchong Ma took a special course with me and contributed to the initial machine vision work. I would like to thank the mentioned students for their contribution to the ATOMICAR group.

During the second half of my PhD project, the ATOMICAR had a lot of collaboration with the VISION group (Professor Stig Helveg, Associate Professor Christian Danvad Damsgaard, and others). We had fruitful discussions in shaping research ideas and interpreting experiment results.

I want to thank Sanshui Xiao and Nicolas Stenger from DTU Photonics, for their input on my optical setup. I would not be able to build the setup without the help from them.

Abstract

This thesis examines the permeability of ultrathin graphite sealed SiO_2 microcavities, by using a high-speed cavity array chip scanner designed based on the Fabry-Pérot interferometer. This work is a prerequisite for realizing catalytic measurement of single nanoparticles on the cavity array chips.

The high-speed cavity array chip scanner measures the resonance frequency of the graphene or graphite membrane and convert the frequency to the internal pressure of the cavities. The basic optical setup for measuring the resonance frequency has been widely used in previous studies. By integrating machine vision and automation techniques, an automatic scanning function is implemented, which is able to scan the cavity arrays without manual operations. The scanning speed and scanning area are orders of magnitudes higher than other measurement techniques for detecting the cavity internal pressure (e.g., atomic force microscope).

 After measuring the leak rates of different gas species, we observe that the leak rates of water-insoluble gases are correlated to the kinetic diameter of the gas molecules. Water-soluble gases tend to leak much faster than water-insoluble gases, which indicates that water or a water-like interlayer on the leakage path may facilitate the leakage.

Diffusion of He and H_2 through the SiO_2 layer of the cavities are measured at room temperature. It is shown that for certain types of the cavities, the H_2 diffusion through the SiO_2 layer could significantly elevate the overall leak rate. For He, this is a more universal behavior for all types of cavities.

We also investigate the permeability of the cavities at high temperatures up to 175 °C. The leak rates at high temperatures are significantly increased. A temperature threshold is determined by comparing the leak rate at a series

of temperatures. Below the threshold, the sample is impermeable (neglecting a very small leak rate), and above the threshold, the leak rates increase with the temperatures in the measurement temperature interval. Sample-to-sample variation of the threshold is also observed and need to be investigated in the future.

Contents

Chapter 1
Introduction

In the past three years I have worked on the ATOMic Insight Cavity Array Reactor (ATOMICAR) project, whose ultimate goal is to measure the chemical turnover of a single catalytic nanoparticle. The project comprises several different subjects, including micro- and nano-fabrication, 2-D materials, catalysis, optics, transmission electron microscope (TEM), etc.

This thesis is focused on the measurement using laser interferometry, and the original title of my PhD project is "High-speed Cavity Array Chip Scanner for Ultrasensitive Catalytic Measurements". Up to now, we have however not achieved the last step of the ATOMICAR project (i.e., Catalytic Measurements), but we have had a satisfactory understanding of the gas permeation rate of our reactor (i.e., graphene or graphite sealed cavities), which provides an indispensable calibration reference for the catalytic measurements. Hence, this thesis will mainly present the investigation of the gas permeation by using the high-speed cavity array chip scanner (a laser interferometry setup). Other essential aspects related to ATOMICAR will be briefly introduced at a glance.

1.1 Catalysis and a Green(er) World

Since the original motivation of the ATOMICAR project is about investigating catalysts, we will start from an introduction of catalysis and its importance in modern society.

Talking about technologies related to sustainability and environment, many people may think of electrical cars, wind turbines, solar panels, etc. Those are the products that get the most exposure in public media. However,

a hidden hero that many people are not aware of, is catalysts. For many industries that involve chemical reactions, catalysis is a key tool to boost or enable most of the reactions. For many of us, we may have had our first lesson about catalysis in middle school or high school, which is about the hydrogen peroxide decomposition reaction:

$$2H_2O_2 \xrightarrow{MnO_2} 2H_2O + O_2 \tag{1.1}$$

In this reaction, hydrogen peroxide is decomposed to form water and oxygen. Hydrogen peroxide itself is relatively stable at ambient conditions. It is widely used as disinfectant and bleaching agent in our daily life. For example, contact lenses are often cleaned by hydrogen peroxide solutions if they need to be reused. If the decomposition reaction happened spontaneously and rapidly in ambient condition, we would not be able to use it. However, when we put MnO_2 into hydrogen peroxide, we can see oxygen starts to be generated, without changing any initial temperature or pressure conditions [1]. This is the magic of a catalyst, which turns impossible to possible. It is therefore crucial for the reaction that does not happen naturally at feasible conditions, and the quality of the catalyst determines the speed that we can obtain or eliminate something.

So far, we have learnt the role of catalysts in chemical reactions, but how does it actually influence our daily life? The most common thing that we may hear in our daily life (if your study or work is not related to chemistry) about catalysis/catalysts is probably the catalytic converter in our cars, which removes environmentally unacceptable compounds in exhaust gas, such as NO_x, SO_x, and CO [2]. Prior to the era that vehicles are mandatory to be equipped with catalytic converters, serious photochemical smog had happened in several modern cities all over the world [3, 4]. The photochemical smog usually results from NO and hydrocarbons emitted by road traffic and

factories. After a series of reactions, NO_2 and O_3 are generated. NO_2 is a reddish-brown gas that colors a brown sky in photochemical smog. Both the NO_2 and O_3 are odorous and harmful to human health. To remove the pollutions from the source, catalytic converters are installed in vehicles. A catalytic converter can reduce NO_x to N_2, and oxidize CO and hydrocarbons to CO_2 and H_2O. All the products are components of the natural atmosphere.

Clearly, catalytic converters are not the only application of catalysis. In fact, about 85-90% of the products of the chemical industry involve catalysis [5]. Typical applications that highly rely on catalysis are petroleum refining, production of chemicals, and reduction of pollution. Enzymes are sometimes also called biocatalysts [6], which are vital to our body and other organism. However, the structures of enzymes are far more complicated than the catalyst used in the chemical industry. From an energy point of view, a good catalyst can significantly reduce the energy consumption of a process, as the principle of the catalyst is to reduce the energy input that is required to enable a reaction[1]. This is how our energy consumption or carbon footprint benefits from catalysis research for traditional applications. In recent decades, several research fields emerge and start to play more important roles in carbon neutrality [7]. These include energy conversion, sustainable fuel, CO_2 capture, etc. Catalysis is crucial to all of the mentioned techniques.

1.2   Develop Better Catalysts

In the previous section, we have learnt how important catalysis is for our green transition. Now the question is how we can develop a good catalyst for a new application, or better catalysts for existing applications. Historically, the

---

[1] A catalytic process still obeys the conservation of energy, as it is only the energy input that triggers the reaction that is reduced. The total energy change of a catalytic process is the same as that of the same reaction without catalysts.

development process was a bit random, and highly depended on luck in the old times. A famous example is the development of the Haber-Bosch process, which produces ammonia from nitrogen and hydrogen. The best candidate, an iron catalyst, was found after 2500 other different catalysts were tested 6500 times [8]. It was basically a trial-and-error process based on intuition, which consume enormous time and resources. Today modern catalysis theory based on density functional theory allows us to calculate and predict the activity of an unknown catalyst. Meanwhile at the experimental side, advanced scientific instruments cluster sources deposition is now able to produce catalysts in nanometer scale, and we can use different characterization techniques to investigate the new catalysts. All these evolutions have made catalysis research systematic and efficient.

The evolution of the research methodologies also changed the scale of the catalysis research. The earliest scientific catalysis work research dating back to the 17th century, was simply about finding a suitable chemical substance that can accelerate a reaction (despite the word catalyst did not exist at that time). By the beginning of the 19th century, researchers started to realize that, for heterogeneous catalysis, physical absorption on the surface of the catalysts is the correct mechanism to explain the phenomenon [9]. Nowadays, most catalysis research is focused on a scale down to nanometer or sub-nanometer level. Since catalytic processes runs on the surface of catalysts, an ideal catalyst should be small in order to obtain a high specific surface area. This is similar to the reason why cells are small, which is because a small cell has more specific surface area to transport substances across its cell membrane. Therefore, a key branch of catalysis research today is about investigating nanoparticles. For metal particles, which are the most commonly used catalysts in industry, the main focuses are on the size, shape, structure, and composition of the particles

[5]. However, our knowledge about catalytic nanoparticles is mostly based on ensemble-averaged activity measurements of a huge amount of particles (e.g., a million), as the measurement of a single nanoparticle has always been a challenging problem [10]. This motivates the ATOMICAR project, which aims to measure single nanoparticles, find a super active nanoparticle, and characterize why it is active.

1.3 The ATOMICAR Project

Here in this section, we will briefly introduce the concept of the ATOMICAR project. As mentioned before, the goal of this project is to measure the catalytic activity of a single nanoparticle. Additionally, we would be able to find super active nanoparticles from thousands of competitors in a single measurement, if the initial plan becomes reality (we are unfortunately a bit away from the ideal case). Lastly, the design of the sample chip allows us to observe the structure of the nanoparticles, which will help us to understand how the size and shape of a nanoparticle affect its activity.

Figure 1.1 depicts the full process of the ATOMICAR project. The first step is the fabrication of the ATOMICAR chips. In each chip, we define thousands of cylindrical micro cavities on its front surface. Then we deposit single nanoparticles to every individual cavity by using a cluster deposition source. After that, reactant gases are sealed in the cavities by a graphene/graphite membrane or other suitable 2D material.

When the cavities are sealed, the samples are ready to be measured. We developed three different methods for the measurement: atomic force microscopy (AFM), laser interferometry, and electron energy loss spectroscopy (EELS). The first two methods are based on the fact that, for a variety of heterogeneous catalytic processes, there is a change in the number of molecules. According to the ideal gas law ($pv = nRT$), this will lead to a

pressure change in a closed system if other conditions (i.e., temperature and volume) remain the same (or only have a negligible change). The pressure change causes a deflection change of the graphene/graphite membrane. The AFM, which is capable of measuring surface topology with an angstrom resolution, can therefore measure the deflection and then we can calculate the pressure change based on that. When the graphene/graphite membrane deforms, its resonance frequency also changes. This is the principle of the laser interferometry method which is able to measure the resonance frequency. A major advantage of the laser interferometry method is that it can scan a large area (~ 1 mm^2) of cavities in a short time period (~ 5 s / cavity). By contrast, the AFM need approximately 5 minutes for a moderate quality scan, and the maximal area is about 0.01 mm^2. The last method, EELS, utilizes a TEM to measure the energy loss of an electron beam transmitting the sample. The energy loss can be converted to the partial pressure of each gas inside the cavities.

After measuring the activities of the nanoparticles, it is important to investigate their structures in order to understand how the structures affect their performance. This can be done by a TEM, which can provide an image showing the 3D structure of a nanoparticle with an atomic level resolution.

Fabricate cavity array chip

Deposit single nanoparticle
to each cavity

Seal reactant gas in the cavities
with graphene/graphite
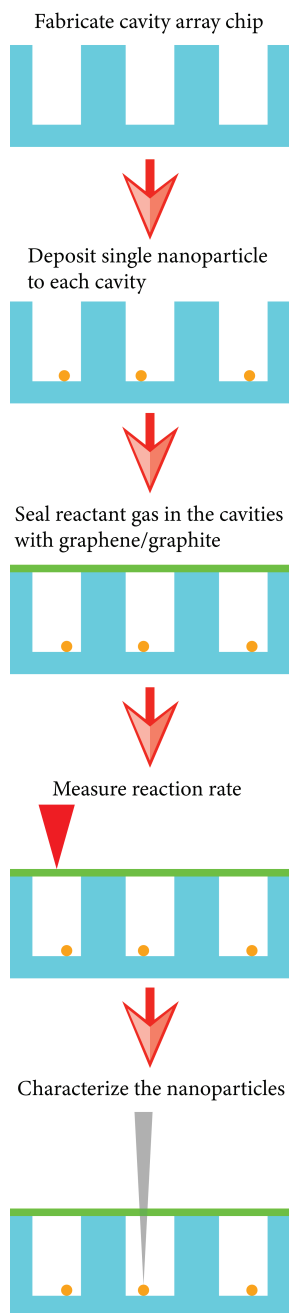
Measure reaction rate

Characterize the nanoparticles

Figure 1.1: Flow chart of the ATOMICAR project. The schematic diagram is not scaled and does not represent the actual structure of the samples.

1.4   Thesis Overview

The contents of this thesis are presented as follows:

- Chapter 1: This chapter.
- Chapter 2: The chip structure and fabrication process of the ATOMICAR chip are presented. A brief introduction to graphene and how we transfer graphene/graphite to the ATOMICAR chip are also presented in this chapter.
- Chapter 3: The design and the mathematical model of the high-speed cavity array chip scanner are described.
- Chapter 4: We present how we map the measured resonance frequencies to the internal pressures of the cavities. Uncertainties of the measurement are also discussed.
- Chapter 5: We present the leak rates of various gas species measured at room temperature. The results reveal the correlation between the gas leak rates of graphite sealed SiO_2 cavities and the kinetic diameter of the gas molecules. We also observe that water-soluble gasses tend to have extraordinarily high leak rates, which indicates that water may exist on the leakage path.
- Chapter 6: We investigate whether the diffusion of small molecules (He, and H_2) through SiO_2 has a significant impact to the overall leak rate. For certain chip structures, the diffusion through SiO_2 can overtake the usual leak path through the graphite-SiO_2 interface.
- Chapter 7: We present leak rates data at different temperatures from 25 °C to 175 °C. The leak rates tend to rise as the temperature increases. We suggest that the change can be caused by thermal stress and a redistribution of the graphite flake at the graphite-SiO_2 interface.
- Chapter 8: Conclusion of this thesis.

Chapter 2
Fabrication and Graphene Transfer

In this chapter, I will first present the structure and fabrication process of the ATOMICAR chip. Then the graphene transfer techniques that were used for the samples will be introduced. The chip fabrication and graphene transfer processes are mostly done by my colleagues but comprise an important part of my work, so I will only briefly present the essential contents about the two disciplines.

2.1   The ATOMICAR Chip

The fabrication of the ATOMICAR chip is based on modern microfabrication technologies. The history of microfabrication dates back to the invention of the transistor in 1947. Although there is no way of calling the first transistor microelectronics, it was the need of fabrication of many transistors on a single piece of semiconductor (i.e., integrated circuits), that boosted the development of microfabrication methods [11]. Today, microfabricated components have become indispensable in our life, as you can find them in almost every electrical or electronic product. Recent development of microfabrication (or nanofabrication as the scale evolves), by 2022, has reached 3 nm resolution for batch production with extreme ultraviolet photolithography [12]. However, if time is unimportant and batch production is unnecessary, electron-beam lithography has provided a similar resolution for decades [13].

For the ATOMICAR chip, since the cavity dimensions in our chips are in the μm scale, we can use the well-established ultraviolet lithography to define our structures. However, certain thin-film deposition and etching

processes are still tricky to be handled. In the ATOMICAR project we mostly have two types of chips: a solid bottom chip and a window chip.

The solid bottom chip (Figure 2.1a and Figure 2.1c) has a typical cavity structure that has been used in many previous studies [14-19]. Briefly, the fabrication only consists of two major steps: growing a SiO_2 layer on the surface of the silicon wafer with a thickness t, and etching the cylindrical cavities whose depth is d. For most of our samples, the SiO_2 layer thickness t varies from 300 nm to 2000 nm, and the cavity depth d varies from 300 nm to 2000 nm as well. Usually d is smaller than t, which forms a pure SiO_2 cavity. For other samples ($d \geq t$), the bottom of the cavity becomes the single crystal silicon substrate, which provides higher reflection of the laser beam when it is measured by the laser interferometry setup. Other than that, there is no significant difference between the two layouts in terms of functions and performance. The solid bottom chips are mainly used to measure the leak rates of the sealed cavities with different conditions (e.g., different 2D material seals, different gases, and different temperatures).
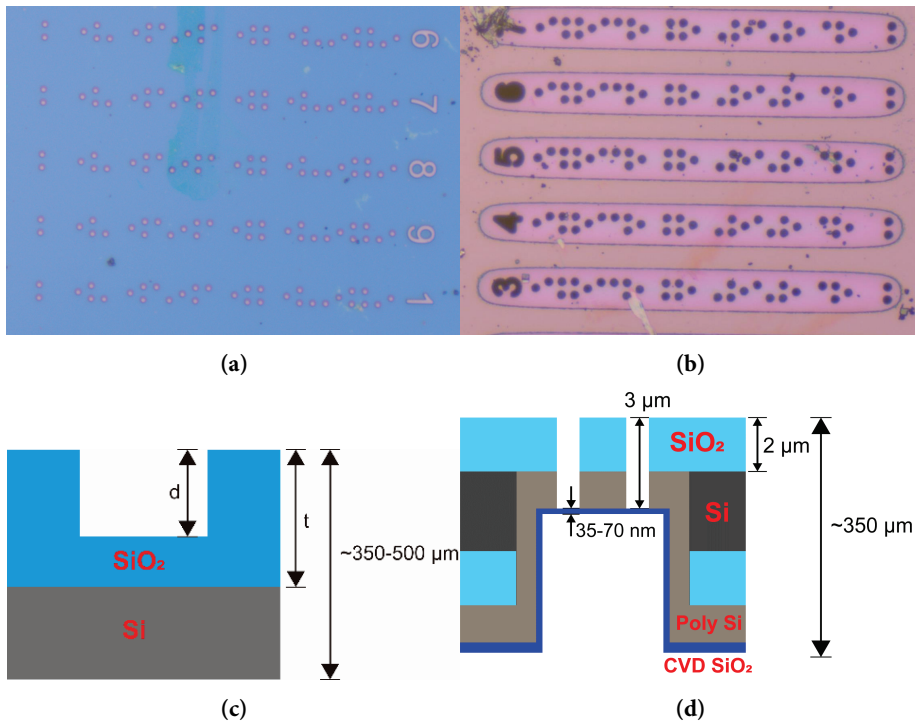
Figure 2.1: The solid bottom chip and the window chip. (a) Optical image of a solid bottom chip. (b) Optical image of a window chip. (c) Schematic diagram of the solid bottom chip. (d) Schematic diagram of the window chip.

The window chip (Figure 2.1b and Figure 2.1d) has a novel design for the ATOMICAR application. It is named after the thin TEM window at the bottom of the cavities. The thin TEM window allows us to detect the gas composition inside the cavity by EELS and observe catalytic nanoparticles in the TEM. In the final structure of the window chips, at the front surface there is a SiO_2 layer similar to the solid bottom chip. Below the SiO_2 layer, for the area around the cavities, there is a polysilicon layer. The polysilicon layer, together with the top SiO_2 layer, form freestanding membranes that support the cavity areas. Lastly, there is a thin chemical vapor deposition (CVD) SiO_2 layer, deposited by either low pressure CVD (LPCVD) or plasma-enhanced CVD (PECVD) techniques, at the back side of the freestanding membranes.

The cavities were fabricated by etching through the SiO_2 layer and the polysilicon layer until the CVD SiO_2 layer (i.e., the TEM window). In order to keep the strength of the freestanding membrane, the thickness of it must be at least about 3 μm. The cavity depth also equals the thickness of the freestanding membrane, which means that the cavities in the windows chips are usually deeper than those of the solid bottom chips. The deeper cavities lead to two major differences for our measurement. The first is the sensitivity. Deeper cavity means greater volume. Assuming two cavities have the same gas leak rate, the one with larger volume will have slower change in pressure. The other difference is the signal strength when using the laser setup. Briefly deeper cavity reduces the signal strength as the bottom of the cavity is further from the focal plan (cavity top) than the solid bottom chips. Details about the principles of the laser setup will be described in Chapter 3.

2.2   Graphene, graphite, and 2D materials

After the discovery in 2004 by Novoselov et al. [20], graphene has become probably the most popular topic in the material science. This popularity, however, also leads to numerous misuses of the word in both business and research. If we type the word graphene in the search bar at Amazon.com, we can see it suggests a number of goods like coating, spray, coat, shampoo, battery etc. (Figure 2.2). None of these items tends to include real graphene, but likely contain graphite instead. Strictly speaking, graphene is defined as a single-atom-thick sheet of carbon atoms. However, this word also prevalently refers to a stack of graphene with different thicknesses. Depending on the number of layers, they are called: bilayer graphene (BLG), few-layer graphene (FLG), or multi-layer graphene (MLG). This is somewhat reasonable since they are mostly used because of their properties as a membrane, or 2D material. A structure thicker than MLG should be categorized as graphite, but in

practice there is no clear and widely accepted threshold to distinguish them. Bianco et al. [21] suggested that the maximal number of layers of FLG and MLG should be about 5 and 10 respectively. Nevertheless, you can still see some literature calling their work as "graphene", despite that their "graphene" is orders of magnitudes thicker than the criteria.
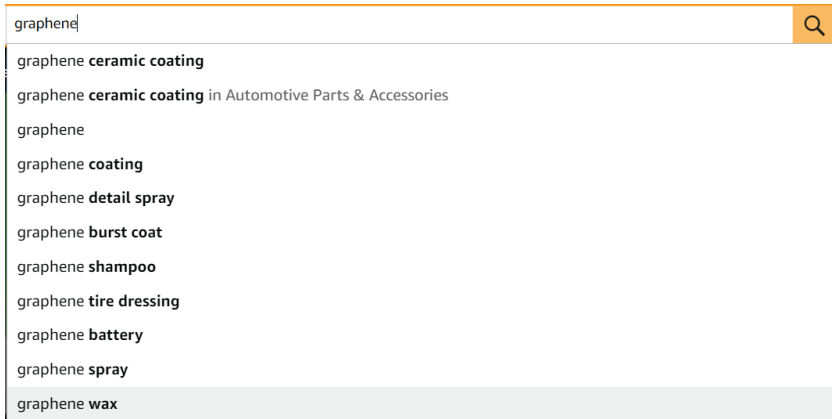
Figure 2.2: Autocompletion of "graphene" from the search bar at Amazon.com.

In this work, the sealing material is mostly flakes exfoliated from natural graphite crystal, with random thicknesses varying from a few layers to ~50 layers. To make the text clear, in the rest of the thesis, the word "graphene" will only refer to single-layer graphene (SLG). Flakes that are thicker than SLG but thinner than ~100 nm will be called ultrathin graphite or graphite membrane. The domain of ultrathin graphite here includes traditional BLG, FLG, and MLG in the guidance [21]. This is due to the fact that many of my samples have a thickness around the threshold between MLG and ultrathin graphite. They do not perform differently when their thicknesses across the threshold, and there is no practical need to distinguish them. Thus, for a more rigorous and consistent expression, ultrathin graphite is used to refer to both of them.

2.2.1   Ultrathin Graphite transfer

There are several different methods to obtain graphene or ultrathin graphite flakes. The traditional way is to mechanical exfoliate the graphene from a natural graphite crystal. Although this is a Nobel prize winning technique, almost every of us can do this in daily life. That is, writing with a pencil. The writing process is essentially an exfoliation process of the graphite, which transfer thin graphite flakes onto the paper. The thickness of the flakes is however a random number. If we are lucky enough, monolayer graphene will appear on the paper, but we have little chance to identify it with the naked eyes. In other words, our distance to the Nobel price is simply some luck plus a pair of super-high-sensitivity eyes which can see the monolayer graphene.

In fact, based on my experience, our actual distance to the Nobel price is probably further than our distance to the practical application of nuclear fusion energy (i.e., 50 years away, no matter whether you are in 1950 or 2022). Therefore, some people who are a bit luckier, smarter, and probably also more fun[1] than us (i.e., Andre Geim's group), shortened the distance by some other office suppliers. They attached a graphite crystal on a piece of Scotch tape, and continuously peeled the graphite with a new piece of Scotch tape, until a monolayer graphene is potentially available on the tape. Then by pressing the piece of tape on a silicon wafer with 300 nm SiO_2 top layer, an optically visible (with microscope) monolayer graphene is obtained [20].

Today the mechanical exfoliation method is still the most commonly used method in our lab, as this method provides the best sealing of the cavity. However, the main disadvantage of this method is that we cannot control

---

[1]Andre Geim won Ig Nobel Prize in 2000

where a flake is transferred and how thick is the flake. The detailed steps of the transfer process are:

1. Clean the chip in an acetone sonication bath.
2. Clean the chip with an oxygen plasma cleaner (Plasma Etch, PE-50) to further remove residuals on the sample surface.
3. Cleave graphite flakes from natural graphite crystals (NGS Graphite, flaggy flakes) by using Scotch tape.
4. Pressing the piece of scotch tape against the sample surface using thumb (directly after the oxygen plasma cleaning process).

As mentioned above, the mechanical exfoliation method is a stochastic process, by which we sometimes cannot get our desired graphite flake. In addition, as the final ATOMICAR chip will have metal nanoparticles deposited in it, the oxygen plasma cleaning process will oxidize the nanoparticles and ruin the future planned catalysis experiment. Therefore, two deterministic transfer methods are also adopted in the ATOMICAR project.

The first deterministic transfer method is a polydimethylsiloxane (PDMS) stamp method [22]. It is an all-dry transfer method, in which the sample is not cleaned by sonication or oxygen plasma. The transfer steps are as follows:

1. A graphene/graphite flake is cleaved from a natural graphite crystal (similar to the mechanical exfoliation method), but with Nitto tape instead of Scotch tape. The Nitto tape is less sticky than Scotch tape.
2. A stamp is made by placing a piece of PDMS gel (Gel-Pak®) on a clean microscope slide.
3. The graphene/graphite flake is exfoliated to the PDMS stamp by contacting the Nitto tape with the stamp.
4. The stamp and the sample are aligned under an optical microscope.

5.   The graphene/graphite flake is transferred to the clean sample substrate by slowly lowering the stamp to the sample surface until a firm contact was formed.

6.   Slowly lift the stamp. Then the graphene/graphite flake is left on the sample surface.

The PDMS stamp method allows us to identify graphite flakes on the PDMS stamp, and transfer the flake to an exact region of interest. However, cavities sealed by the PDMS method are usually much leakier than those sealed by mechanical exfoliation method and the cellulose acetate butyrate (CAB) method, which will be described below. Generally, air can escape from a standard cavity ($v \approx 10$ μm³) for only a few minutes (some good samples however have a time constant for ca. one hour), which makes catalytic experiment unfeasible.

The CAB transfer method is developed based on [23]. The major advantage of it is that SLG can be identified and transferred deterministically. It is similar to the PDMS method, but CAB is used as an extra layer on the stamp. The process comprises the following steps:

1.   Transfer graphene and graphite flakes to a silicon wafer with a 90 nm SiO_2 top layer. This thickness provides the best optical contrast for identifying the flakes.

2.   Use an optical microscope to find a flake of interest. SLG can also be found on the wafer with 90 nm SiO_2 layer (green light, $\lambda \approx 540 \ nm$, is preferable, but white light works as well) [24].

3.   Spin coat 20 g / 100 ml CAB in ethyl acetate solution on the sample wafer (1000 rpm, 1 minute).

4.   Cure the CAB for 6 minutes at 60°C.

5. Identify the flake of interest again, and cut a small piece of the CAB where the flake is located.

6. Place a droplet of ultrapure water (Milli-Q) on the cut. The wetting helps to lift the CAB piece with a tweezer.

7. Place the CAB piece on a PDMS stamp, which is the same as that used in the PDMS method (PDMS gel on a microscope slide).

8. The stamp and a sample chip are aligned under an optical microscope. The chip is placed on a heater at 80-135 °C to make the CAB liquid.

9. Slowly lower the stamp to the sample surface until a firm contact was formed.

10. Cool down the sample and lift the stamp, which leaves the flake and CAB on the sample surface.

11. Dissolve the CAB in acetone.

The CAB transfer process can also be modified with a wet alignment process as below:

1-6. Same as the above original CAB transfer process.

7. Place the CAB piece directly on the sample substrate, with a small droplet of ultrapure water between the CAB piece and the substrate. The water allows us to move the sample freely on the substrate.

8. Align the CAB piece under an optical microscope by poking the CAB with a tweezer.

9. Wait until the water evaporates. Then dissolve the CAB in acetone.

In our experience, the CAB method provides a medium level of sealing of the cavities, usually slightly worse than the mechanical exfoliation, but much better than the PDMS method. The leakage time constant for a 10 μm^3 cavity is usually in a range from an hour to one day. It is a wet transfer method

(CAB is dissolved in solvent), but for the dry alignment version, theoretically no liquid medium reaches catalytic particles inside the cavities. The major disadvantage of the CAB method is the heating process, which leads to two problems. The first is that it may affect certain thermal catalytic reactions. The ideal reaction we want to measure should be inactive at room temperature, and under a heating condition the reaction starts. Therefore, despite that the heating temperature is not very high, the heating process in the CAB method can still trigger some reactions, and leave us nothing to measure. The other issue is that the interferometry signal of a CAB transferred graphite membrane, usually has multiple peaks, which makes auto tracking of the resonance frequency a bit challenging. The problem is also attributed to the heating process because we observed similar phenomena after measuring some samples under heating conditions (see Chapter 7 for details). A possible reason to explain the phenomenon is that the thermal stress during the heating process is not released after cooling down, or the thermal stress dislocates the graphite flake against the substrate (graphene has a negative thermal expansion coefficient [25]).

All the three graphite transfer methods introduced above, essentially are processes cleaving graphite flakes from natural graphite crystals. Today synthetic graphene is also widely available both in laboratories and commercial markets. Typical synthesis techniques include CVD [26-28], reduction of graphite oxide [29, 30], epitaxial growth [31-33], etc. In the ATOMICAR project, we attempted to use the CVD graphene on our ATOMICAR chips, but it was not quite successful. There are mainly two reasons that CVD graphene does not fit the ATOMICAR application. First is that the CVD graphene (usually SLG) is easy to break, as the transfer process involves some wet process, and the surface tension of the liquid can break the

graphene membrane suspended on the cavities. The second reason is that commercially available CVD graphene is mostly polycrystalline, although large-area monocrystalline CVD graphene has been fabricated in some laboratories [34, 35]. Gases can easily leak through the grain boundaries of the CVD graphene, as a single atom lattice vacancy can allow the gases leak out in ca. 1 s [14], which makes catalytic processes impossible in a CVD graphene sealed cavity.

Chapter 3
The High-Speed Cavity Array Chip Scanner

The design of the high-speed cavity array chip scanner (HSCACS) was the initial objective of this PhD project. The adjective "high-speed" is used in comparison with the AFM measurement. With the AFM in our lab (Nanosurf FlexAFM), a measurement usually takes about 5 minutes (medium quality) to 30 minutes (high quality). The maximal scanning area is 100 µm × 100 µm (covering ~20 cavities, for a coarse measurement). Practical scanning area is usually about 5 µm × 5 µm to 30 µm × 30 µm (about 1-5 cavities). By contrast, the HSCACS, which is based on laser interferometry, takes about 1-3 seconds to measure a cavity. Technically, it is capable of scanning a 1 cm × 1 cm area. This has however not been realized, as the graphite coverage on our samples has never reached a mm² scale. Scanning of a single large flake has been demonstrated to be successful.

3.1   The Laser Interferometry Setup

The core of the HSCACS is the optical laser Fabry–Pérot interferometer (the working principle will be explained later), which has been used in many micromachine studies since the 1990s [14, 19, 36-40]. Figure 3.1 shows the full experimental setup. The setup starts from the HeNe laser source, which emits a 633 nm linear polarized red laser beam. The beam passes through a polarizer (P), which is aligned to the same direction as the polarization direction of the beam. The beam then goes through a Faraday rotator (F), which rotates the polarization direction for 45°. The rotated beam goes through a polarized beam splitter (PBS) and a 1/4 waveplate that turns the linear polarized beam

into a circularly polarized beam. The beam can go through a dichroic mirror and reaches an electronic shutter (S). The shutter is connected to a lab computer which controls the entire setup. After passing through a lens (f = 50 mm), the beam enters the Thorlabs CSE2100 epi-illuminator module (Epi, the dash-line square area). Inside the module the beam is reflected by a bandpass dichroic mirror (BDM, 95% reflection band = [365,404] ∪ [458,490] ∪ [530,560] ∪ [619,647]). The BDM allows most of white light to pass through it for imaging purpose, while redirecting the laser beam to the illumination path. Then a lens (f = 120 mm), together with the lens outside the module, forms a Keplerian beam expander, which increases the laser beam radius in order to match the entrance pupil of the objective lens of the microscope. Part of the expanded beam is reflected by a 70/30 beam splitter (BS), and reaches the 50× objective lens. The beam is focused to the sample, which is located inside a sample chamber (SC) that sits on a motorized *xyz* stage.
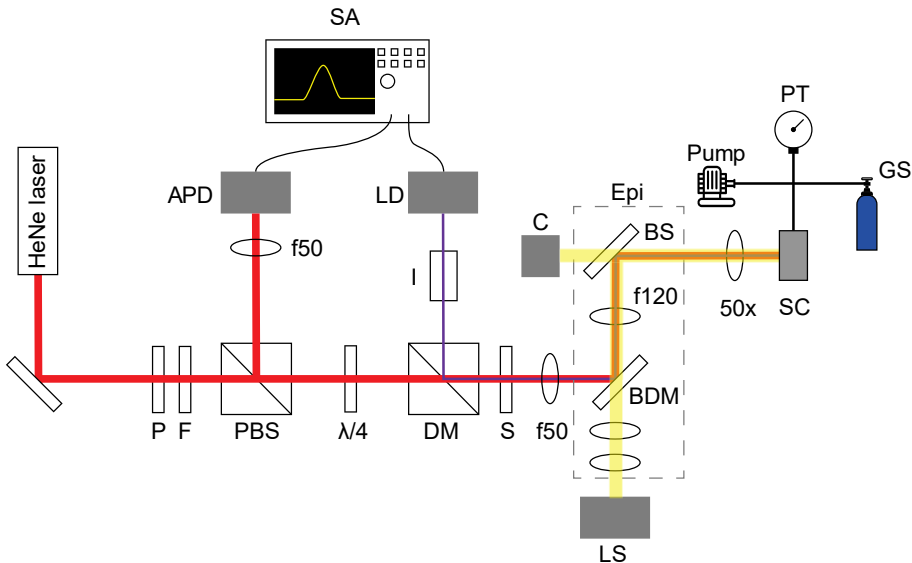

Figure 3.1: The laser interferometry setup. Abbreviations of the individual components are explained in the main text.

The reflected beam (i.e., the interference signal combining the reflection from the graphite membrane and the bottom of the cavity) follows the same path as the incoming beam, until the PBS. The incoming beam was linear polarized before the 1/4 waveplate. After passing the 1/4 wave plate twice (incoming and reflection), the reflected beam becomes linear polarized again but perpendicular to the initial polarization direction. Therefore, the reflected beam is reflected by the PBS towards an avalanche photodetector (APD). A lens (f = 50 mm) in front of the APD focuses the beam to the detector sensing area. The APD converts the optical signal to an electrical signal for a spectrum analyzer (SA). Finally, the SA transfers the time-domain signal to a frequency-domain signal, from which we can obtain a resonance spectrum.

Although the graphite membrane vibrates at their natural frequencies all the time, the amplitude of the vibration, without an external excitation, is usually extremely small. Hence, a second laser is coupled to excite the resonance to increase the readout signal. A laser diode (LD) emits a 405 nm laser beam (it is technically violet, but in most literature [18, 41, 42], it is called blue, so we will also call it blue from here on). The intensity of the blue laser is modulated by the SA. An optical isolator (I) protects the laser diode from the reflection. The blue laser is coupled to the red laser path by the dichroic mirror. When the blue laser hits the graphite membrane, the graphite membrane vibrates following the modulation frequency of the blue laser due to the optothermal effect. The amplitude of the vibration depends on how close the modulation frequency is to the resonance frequency of the graphite membrane is.

To observe the samples and align the laser, a camera (C) is mounted on top of the epi-illumination module. The illumination is provided by a white

light source (LS, 5700K). The epi-illumination module provides a Köhler illumination, which generates an uniform illumination on the sample.

3.2 The Fabry–Pérot Interferometer and Thin Film Optics

The interferometry measurement is based on the Fabry–Pérot interferometer (Figure 3.2). A typical Fabry–Pérot interferometer consist of three mediums separated by two reflecting interfaces. The interferometry pattern is mainly formed by the combination of the reflection from the first interface (R_0) and the reflection from the second interface (R_1). However, part of the reflection from the second interface, is reflected by the first interface. Those reflected by the first interface are reflected by the second interface again and form a secondary reflection (R_2). The multiple reflections between the two interface is repeated again and again until the beam power reaches infinitesimal. Therefore the de facto reflection is $\sum_{j=0}^{\infty} R_j$. If we assume the incident light is normal to the interface, by some calculations we can obtain the total power reflectance [43]:

$$R = \left| \frac{r_{01}e^{ikl} + r_{12}e^{-ikl}}{e^{ikl} + r_{01}r_{12}e^{-ikl}} \right|^2 \tag{3.1}$$

$$r_{pq} = \frac{n_p - n_q}{n_p + n_q} \tag{3.2}$$

$$k = \frac{2\pi}{\lambda} \tag{3.3}$$

where i is the imaginary unit, R is the total power reflectance; r_{pq} is the (amplitude) reflection coefficient between layer p and layer q; n_p refers to the refractive index of layer p, l is the thickness of the middle layer; k is the wavenumber; and λ is the wavelength of the light.
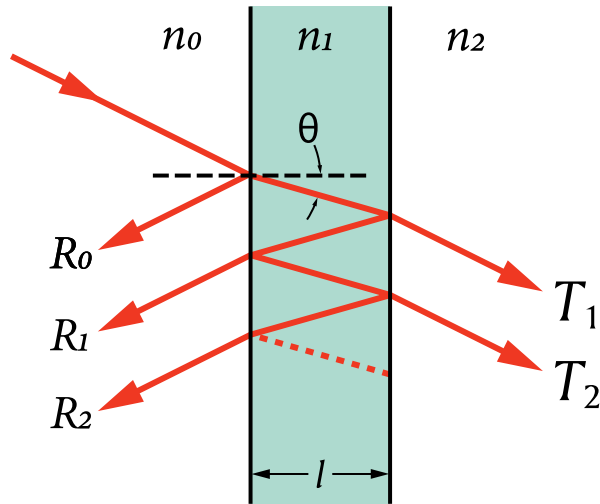
Figure 3.2: Schematic diagram of the Fabry–Pérot interferometer.

When applied to thin film optics, the above equation is also the solution for a single-layer film, such as a simple antireflection coating on glasses (i.e., three-layer structure: air-coating-glass). However, when modelling the ATOMICAR chips, the model becomes a bit more complicated as Figure 3.3 shows. The solid bottom chip is equivalent to a double-layer thin film, and the window chip is equivalent to a triple-layer thin film. Since the structure becomes so complicated, the ordinary method which solves the problem by calculating geometric series layer by layer becomes extremely difficult. Therefore, the transfer matrix method [44] is needed to simplify the calculations.

Solid bottom chip

Air/vacuum

Graphene

Air/vacuum

Si/SiO$_2$

Window chip

Air/vacuum

Graphene

Air/vacuum

SiO$_2$

Air/vacuum

Figure 3.3: Multilayer structure of the ATOMICAR chips.

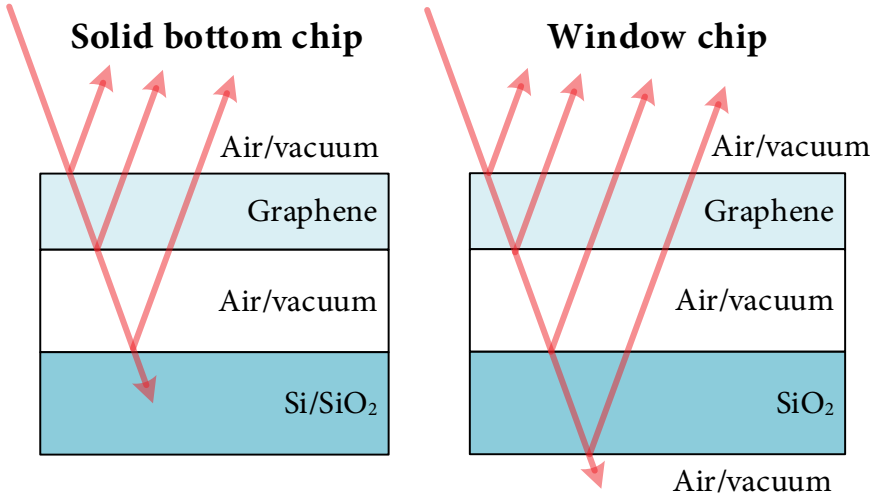The transfer matrix method uses a series of matrices to describe the multilayer structure. Figure 3.4 shows a structure with *m* layers (the 0th layer is the incidence medium, and the (*m*+1)th layer is the final substrate medium). Every transmission matrix (*D*) describes how light passes through an interface, and every propagation matrix (*P*) describes how light passes through a medium layer. The overall structure can be therefore described by the following equation:

$$\begin{bmatrix} E_{in} \\ E_{refl} \end{bmatrix} = D_{01}P_1D_{12}P_2 \dots D_{m-1,m}P_mD_{m,m+1}\begin{bmatrix} E_{trans} \\ 0 \end{bmatrix} \qquad (3.4)$$

where E_{in} is the electromagnetic wave of the incident light; E_{refl} is the total reflected wave; E_{trans} is the total transmission wave.

D$_{01}$ P$_1$ D$_{12}$ P$_2$ D$_{23}$ ... D$_{m-1,m}$ P$_m$ D$_{m,m+1}$

E$_{in}$ → E$_{trans}$

n$_0$ n$_1$ n$_2$ ...   n$_m$ n$_{m+1}$
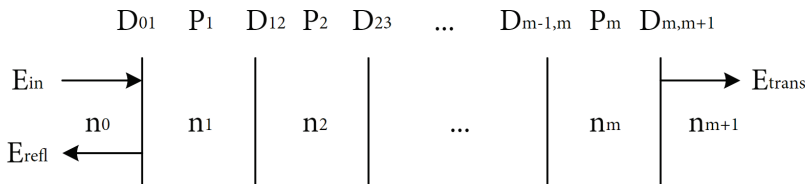
E$_{refl}$ ←

Figure 3.4: Schematic diagram of the transfer matrix method.

The transmission matrix (Figure 3.5a) relates the wave of layer j traveling to the right (E_j^r), the wave of layer j to the left (E_j^l), the wave of layer $j+1$ to the right (E_{j+1}^r), and the wave of layer $j+1$ to the left (E_{j+1}^l):

$$\begin{bmatrix} E_j^r \\ E_j^l \end{bmatrix} = D_{j,j+1} \begin{bmatrix} E_{j+1}^r \\ E_{j+1}^l \end{bmatrix} \tag{3.5}$$

Solving the equation with the Fresnel equations yields:

$$D_{j,j+1} = \frac{1}{t_{j,j+1}} \begin{bmatrix} 1 & r_{j,j+1} \\ r_{j,j+1} & 1 \end{bmatrix} \tag{3.6}$$

The propagation matric (Figure 3.5b) relates the waves traveling in and out at the left interface of a layer (E_{jA}^r and E_{jA}^l), and the waves traveling in and out at the right interface of a layer (E_{jB}^r and E_{jB}^l):

$$\begin{bmatrix} E_{jA}^r \\ E_{jA}^l \end{bmatrix} = P_j \begin{bmatrix} E_{jB}^r \\ E_{jB}^l \end{bmatrix} \tag{3.7}$$

We can solve the equation with the wave propagation formula:

$$E_{jA}^r = E_{jB}^r e^{i \cdot k L_j} \tag{3.8}$$

$$E_{jA}^l = E_B^l e^{-i \cdot k L_j} \tag{3.9}$$

which yields:

$$P_j = \begin{bmatrix} e^{i \cdot k L_j} & 0 \\ 0 & e^{-i \cdot k L_j} \end{bmatrix} \tag{3.10}$$

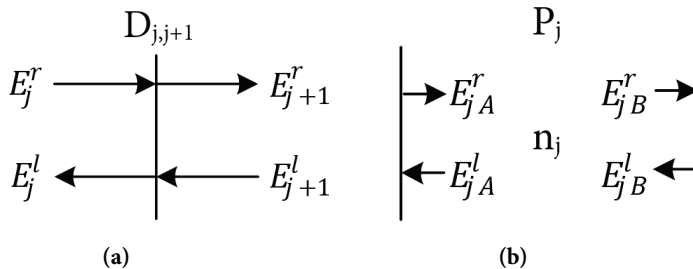Here, k is the wave number, and L_j is the thickness of layer j.

Figure 3.5: Schematic diagram of the transmission matrix and the propagation matrix. (a) The transmission matrix of the interface between layer j and layer j+1. (b) The propagation matrix of layer j.

After obtaining all the D matrices and P matrices, we can multiply them together as a matrix M, and equation (3.4) becomes:

$$\begin{bmatrix} E_{in} \\ E_{refl} \end{bmatrix} = M \begin{bmatrix} E_{trans} \\ 0 \end{bmatrix} \tag{3.11}$$

Now we can solve the simple equation and get the reflection coefficient:

$$r = \frac{E_{refl}}{E_{in}} = \frac{M_{21}}{M_{11}} \tag{3.12}$$

3.3 Optimization of the Cavity Structure

Based on the transfer matrix method described in the last section, we can obtain the reflectance from our sample as a function of the cavity depth, thickness of the graphite, and the thickness of the SiO_2 window (for the window chip). The resonance signal is generated from an oscillation of the total reflectance, which results from an oscillation of the cavity depth when the graphite membrane vibrates. Therefore, we can tune the cavity structure based on the thin-film model, in order to optimize the signal strength of the resonance spectrum.

For the solid bottom chips, as shown in Figure 3.3, there are two layers, graphite and the cavity, that affect the reflectance. Figure 3.6a shows the calculated reflectance as a function of the graphite thickness and cavity depth for a solid silicon bottom chip. Taking a partial derivative of the function of the cavity depth, we obtain the responsivity (Figure 3.6b, also presented by Davidovikj et. al. in 2016 [19]), which indicates how much the reflection light intensity changes when the graphite membrane deforms for a unit distance. Note that it is the absolute value of the responsivity determining the signal strength, as for a vibration, the motion goes in both directions. From the results we can conclude a suitable cavity depth that provides high responsivity can be about 220 nm or 380 nm.

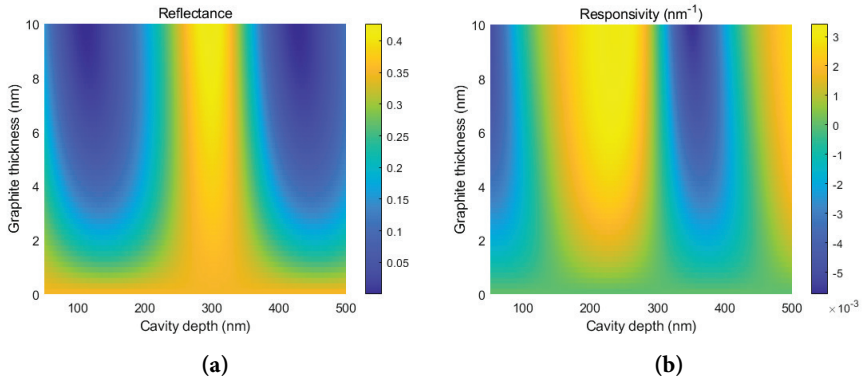**(a)**   **(b)**

Figure 3.6: Optimization of the solid bottom (Si bottom) chip. (a) Reflectance versus graphite thickness and cavity depth. (b) Responsivity versus graphite thickness and cavity depth.

For the window chips, a similar calculation can be performed. However, in the case of the window chips, we have three variables (graphite thickness, cavity depth, and window thickness). It is difficult to visualize the function by a 2D plot. We can assume a 10-layer graphite flake (a common average result for the random mechanical exfoliation process we have obtained), and simplify the function, which yields the results in Figure 3.7. In this calculation, the interval of cavity depth is [2500 nm, 4000 nm], instead of [50 nm, 500 nm] in the case of the solid bottom chip. This is because, as described in Section 2.1, the freestanding membrane needs extra thickness to keep its strength. From the result, we can see the difference between each two adjacent optimized cavity depth (from light yellow to deep blue) is approximately 160 nm, which roughly equals to 1/4 of the laser wavelength (633 nm). In terms of the window thickness, it can be seen that thicker windows provide better responsivity. However, for the TEM measurement, thinner windows provide better signal and resolution. Therefore, a good trade-off between the laser and TEM measurement has to be considered.
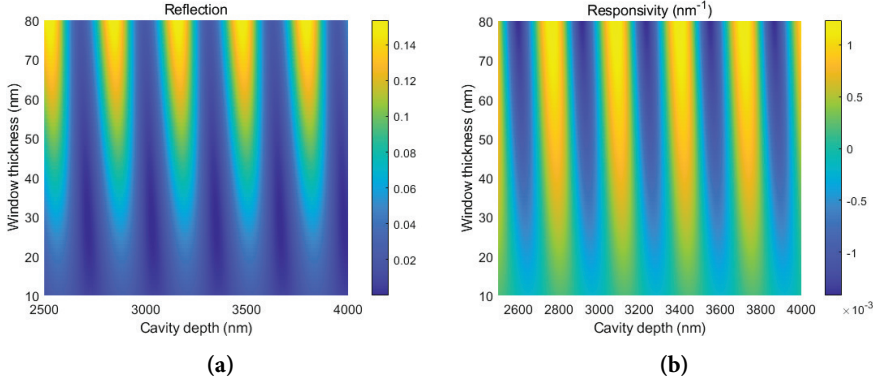
(a)   **(b)**

Figure 3.7: Optimization of the window chip. (a) Reflectance versus window thickness and cavity depth. (b) Responsivity versus window thickness and cavity depth.

The above calculations provide a useful reference of how the cavity structure should be optimized in order to receive maximal resonance signals. In practice, the influence from tuning the thickness of each layer is actually limited for two reasons. The first reason is that under different pressure differences across the graphite membrane, the membrane can deflect for up to about 100 nm, which may cause a change of the responsivity from a maximum to a nearly minimal value. The second reason is about the fabrication accuracy of the chip, especially for the window chip. With the current fabrication process it is not possible to control the window thickness at a nm resolution.

3.4 Vibration Model

The resonance of the graphite membrane can be modelled as a stretched circular membrane with a uniform surface tension T. The natural frequency of the membrane is [45]:

$$f_{m,n} = \frac{x_{m,n}}{2\pi a} \sqrt{\frac{T}{\rho_A}} \tag{3.13}$$

where m and n are the mode numbers (m for the circumferential direction and n for the radial direction), T is the surface tension, ρ_A is the areal mass density of the membrane, a is the radius of the circular membrane, and $x_{m,n}$ is the nth

non-trivial solution of the mth–order Bessel function. Our measurement is mostly based on the fundamental mode $f_{0,1}$. In this case, $x_{0,1}$ = 2.405 [46].

The surface tension can be related to the strain ε of the membrane by the following equation:

$$T = \frac{Et}{1-\nu}\varepsilon \qquad (3.14)$$

where E is the Young's modulus, t is the thickness of the membrane, and ν is the Poisson's ratio.

The surface tension can also be expressed as the sum of two components, the initial pretension T_0 and the pressure-induced tension T_p:

$$T = T_0 + T_P \qquad (3.15)$$

T_0 is usually 0.1-0.7 N/m [47, 48]. When there is a sufficiently large Δp (> 300 mbar), the strain related to T_p can be calculated by the extended Hencky solution [49]:

$$\varepsilon = \frac{1}{4}\left(\frac{\Delta pa}{Et}\right)^{\frac{2}{3}}\sum_{k=0}^{\infty}[[1-(2k+1)\nu]A_{2k}] \qquad (3.16)$$

where A_{2k} is a series of coefficients, which can be found in [49].

Combining equation (3.13)-(3.16), we can see that the resonance frequency f is proportional to the cubic root of Δp. However, it is not practical to predict the resonance frequency with this model because our current knowledge about the mechanical properties of graphene and graphite contains a lot of uncertainty. For example, the Young's modulus of SLG reported in the literatures varies from ca. 1 TPa to 2.4 TPa [50-53]. For a thin graphite flake with an uncertain thickness, the parameter becomes even more random. Nevertheless, the model together with experiment data, allows us to estimate the properties of a measured graphite flake.

3.5 Automatic Scanner

In order to track multiple cavities automatically, we need to localize the chip, and align the laser spot to the cavities. A low-cost solution is to use computer vision with the microscope camera.

3.5.1 Recognition of the cavities

Since all the cavities in the ATOMICAR chips have cylindrical shapes, they can be easily identified from a microscope image as circles. We use the circular Hough transform (CHT) algorithm to find the cavities [54, 55]. Briefly the process consists of three steps:

1. Pixels on the edge of a shape (the edge can be determined by a high gradient or simply the boundary of a black and white binary image) are selected to cast 'votes' (i.e., increase voted variables by one) in an accumulator array. The pixels vote for other pixels around them that forms a full circle (Figure 3.8a).

2. The votes of pixels belonging to an image circle tend to accumulate at the center of the circle. Therefore, we can find the center by detecting a local maximum in the accumulator. Figure 3.8b shows an example of accumulating the votes from 6 pixels. The red point is the local maximum in the accumulator, and also the center of the circle.

3. Calculate the radius of the detected circle, and check if it is within the searching interval.
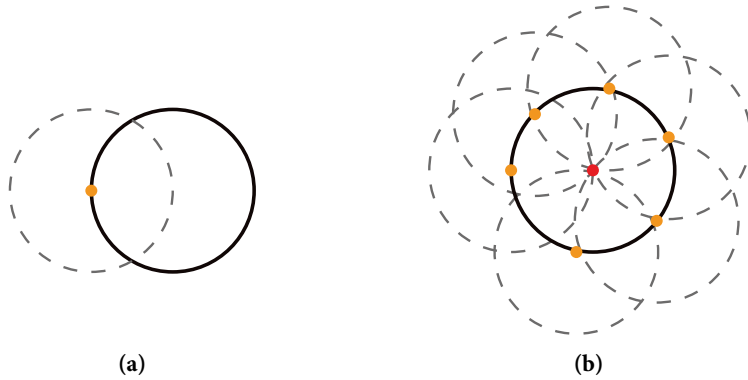
Figure 3.8: The CHT algorithm. The solid black circle is the edge of the object. (a) a pixel (orange point) on the edge "votes" for the pixels around it (grey dash line circle). (b) The results after counting the "votes" from 6 edge pixels. The red point has the most votes in the accumulator.

3.5.2 Coordinate Transformation

After detecting the cavities in the image, we need to align the cavities to the laser spot. This requires a coordinate conversion from the image to the motorized stage where the sample chamber sits. The conversion can be expressed as follows:

$$p_s = Rp_i + kd \tag{3.17}$$

where $p_s = (x_s, y_s)$ is the coordinate in the stage frame; $p_i = (x_i, y_i)$ is the coordinate in the image frame; k is a scale factor mapping the pixel size to the actual distance; $d = (d_x, d_y)$ is a translation vector; and R is a rotation matrix based on the angle between the two frames θ:

$$R = \begin{bmatrix} cos\theta & -sin\theta \\ sin\theta & cos\theta \end{bmatrix} \tag{3.18}$$

The parameter k can be calculated by combining the magnification of the objective lens and the pixel size of the camera. Therefore, we only need to find d and θ. We can calculate them by comparing the coordinates of the cavities in the image with their coordinates on a map (i.e., the design layout). It is impossible to calculate rotation if we only have the coordinate of a single point

(cavity), so we can connect the cavities with lines and calculate the transformation of the lines. Figure 3.9 depicts the transformation of three cavities a, b, c on the map, to their counterpart A, B, C in the image. Take line AB as an example, we can find the rotation angle as:

$$\phi_{ab} = arctan \frac{y_b - y_a}{x_b - x_a} \tag{3.19}$$

$$\phi_{AB} = arctan \frac{y_B - y_B}{x_A - x_A} \tag{3.20}$$

$$\theta_{m \to i} = \phi_{AB} - \phi_{ab} \tag{3.21}$$

Similarly we can calculate the rotation angle for lines AC and BC. Then by taking an arithmetic mean we obtain the final θ. The translation vector can now also be obtained by plugging all the cavity coordinates into the equation (3.17).
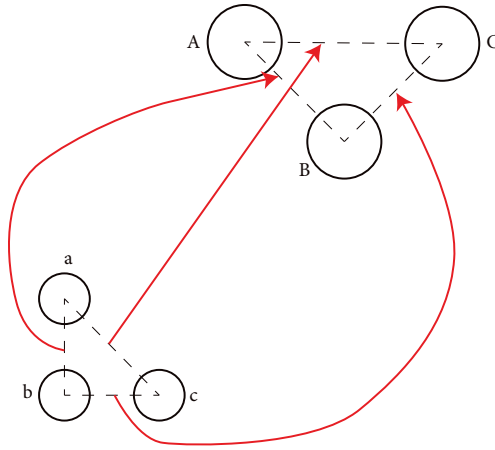
Figure 3.9: Example of transforming three cavities on the map to the image. A, B, and C are the cavities in the image and a, b, and c are the cavities on the map.

After calculating the d and θ, they are stored in the program. When the scanner moves from cavity A to cavity B, the input to the stage controller u_{AB} is modified from the displacement vector on the map δ_{AB}^M with the rotation matrix:

$$u_{AB} = R^{-1} \delta_{AB}^M \tag{3.22}$$

After each movement, the d vector is updated accordingly:

$$d' = d + \frac{u_{AB}}{k} \qquad (3.23)$$

3.5.3 *Image Preprocessing*

To achieve higher precision in the image recognition process, we need to preprocess the image as the image may contain noise, aberrations, and unexpected residues on the sample surface.

The first step is to remove the noise by the low-pass Wiener filter, which smooths each pixel x based on its neighborhood as:

$$b(x) = \mu + \frac{\sigma^2 - v^2}{\sigma^2}(x - \mu) \qquad (3.24)$$

where μ is the local mean of the neighborhood around the pixel, σ^2 is the variance of the neighborhood, and v^2 is the noise variance estimated by taking the average of all the local neighbourhood variance of the image.

The next step is to correct nonuniform illumination. A perfect Köhler illumination system should provide a uniform illumination on the sample as described in Section 3.1. This is achieved by focusing the illumination light on the back focal plane of the objective lens. However, the lenses in our objective set (4×, 10×, 20×, and 50×) have different back focal planes, so the focal point of the illumination light is set between the back focal planes. In addition, the actual light source is naturally not an ideal light source, which creates nonuniformity at the source. Fortunately, this issue can be easily corrected by subtracting the background from the image. The background can be obtained by a morphological closing operation of the image, which removes small dark patterns (i.e., cavities) of the image. Usually the corrected image tends to have lower contrast than the original, so the intensity values of the image have to be adjusted to saturate the dynamic range of the data type.

In Figure 3.10 we can see an example of the preprocessing and its effects. The original color photo (Figure 3.10a) is first converted to a grey image

(Figure 3.10b). Then the Wiener filter smoothed the photo (Figure 3.10c). After removing the background (Figure 3.10d), the patterns on the photo have a good contrast. In the final binary image (Figure 3.10f), all the cavities can be seen clearly. By contrast if we binarize the unprocessed grey image (i.e., Figure 3.10b), some cavities at the boundary or covered by graphite are lost (Figure 3.10e).
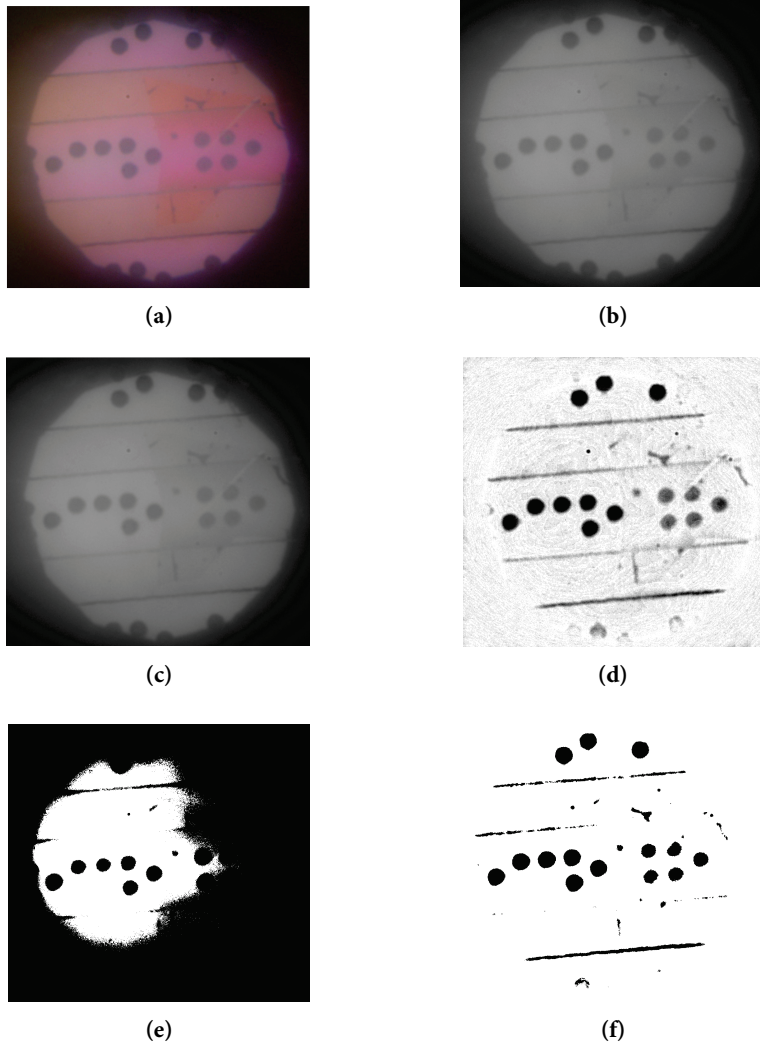
Figure 3.10: The preprocessing of an image. (a) Original image. (b) Grey image. (c) Image after processed by the Wiener filter. (d) Image after correcting the nonuniform illumination. (e) Binary image converted from the original image. (f) Binary image converted from the preprocessed grey image.

3.5.4   The Overall Scanning Processes

In sections 3.5.1-3.5.3, we have introduced the techniques we used to detect cavities in the microscope image and achieve an automatic scan of the cavity

array. Here we summarize the techniques and illustrate the full program in Figure 3.11. The first step is to mark the laser spot in the image so that the program can know where the cavities should move to. Then we need to manually select two cavities from the image and match them in the map, which provides an initial set of transformation parameters (i.e., rotation angle and displacement). With the transformation parameters, the program matches the cavities in the image to the map and calculated the actual transformation parameters. Then the scanner aligns each cavity to the laser spot and measures the cavities in a loop. After all the cavities are measured, the program checks if the finish criteria (time limit, number of loops, or manual termination) are met. If the scanning continues, it goes back to the image calibration process to get a new set of the transformation parameters in order to cope with sample drift, and repeats the loop until the finish criteria are finally met.
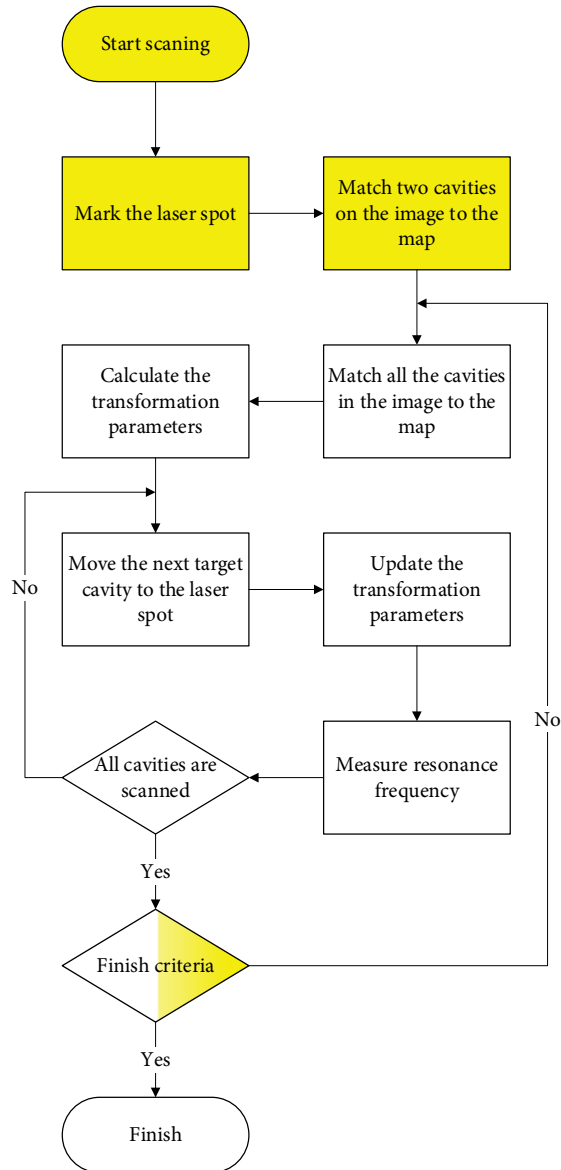
Figure 3.11. Flow chart of the scanning program. Yellow blocks indicate that the process requires manual input.

3.5.5   Autofocusing

The cavity array scanner includes an autofocus function, which controls the z-axis of the motorized stage based on the image. The autofocus function is not a regular part of the auto scanning processes, as we mostly perform scanning of small areas at room temperature. The autofocus is utilized when we need to scan a large area or at an elevated temperature: when scanning for a large area, as the sample may not be perfectly perpendicular to the illumination light, the sample will be out of focus after moving a long distance. As for the heating condition, the thermal expansion also causes a drift in z direction, and thus requires autofocusing.

To evaluate the relative degree of focus (i.e., sharpness) of the images, we use the Gaussian derivative method [56], whose focus score is given by:

$$F(\sigma) = \frac{1}{NM} \Sigma_{x,y} (f_{x^2} + f_{y^2}) \tag{3.25}$$

where N and M are the number of pixels in the x- and y-direction respectively. f_{x^2}, f_{y^2} are the image filtered by a Gaussian derivative convolution filter in the x- and y-direction respectively as follows:

$$f_{x^2} = [f(x,y) * G_x(x,y,\sigma)]^2 \tag{3.26}$$

$$f_{y^2} = [f(x,y) * G_y(x,y,\sigma)]^2 \tag{3.27}$$

Here $f(x,y)$ is the image grey value, and $G_x(x,y,\sigma)$, $G_y(x,y,\sigma)$ are the first-order Gaussian derivative at scale σ in the x- and y-direction respectively:

$$G_x = \frac{-x}{\sqrt{2\pi}\sigma^3} e^{-\frac{x^2+y^2}{2\sigma^2}} \tag{3.28}$$

$$G_y = \frac{-y}{\sqrt{2\pi}\sigma^3} e^{-\frac{x^2+y^2}{2\sigma^2}} \tag{3.29}$$

In short, the Gaussian derivative convolution removes the noise in the image and evaluates the gradient at each pixel. Figure 3.12 shows the focus curve of a window chip sample. The curve is well monotonic before and after the focus position (z = 0 μm), and therefore we can use a simple hill-climbing algorithm

(i.e., move towards the direction in which the focus score increases, until reaching the local maximum) to search for the maximum position. Figure 3.13 illustrates how the Gaussian derivative convolution filter evaluates the images from this sample, at the focal plane (z = 0 μm), and an out of focus position (z = -10 μm). Patterns in the focused image (Figure 3.13d and Figure 3.13e) are much brighter than those in the out of focus image (Figure 3.13c and Figure 3.13d). This indicates that the focused image is sharper, and the sum of the filtered image values generates a higher focus score in equation (3.25).
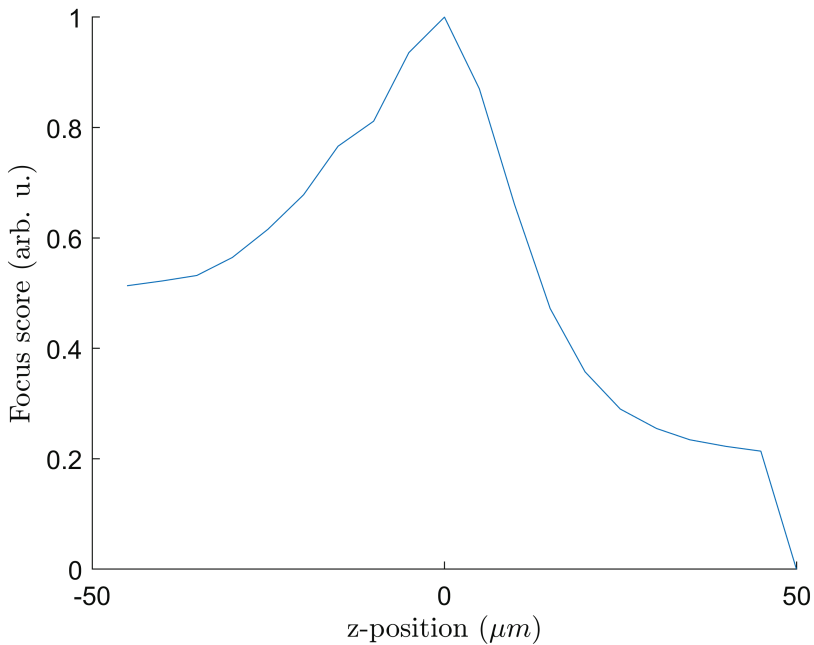
Figure 3.12: Focus score as a function of the z-position measured on a window chip. z = 0 μm is the focal plane.

(a)

(b)

(c)

(d)

(e)

(f)
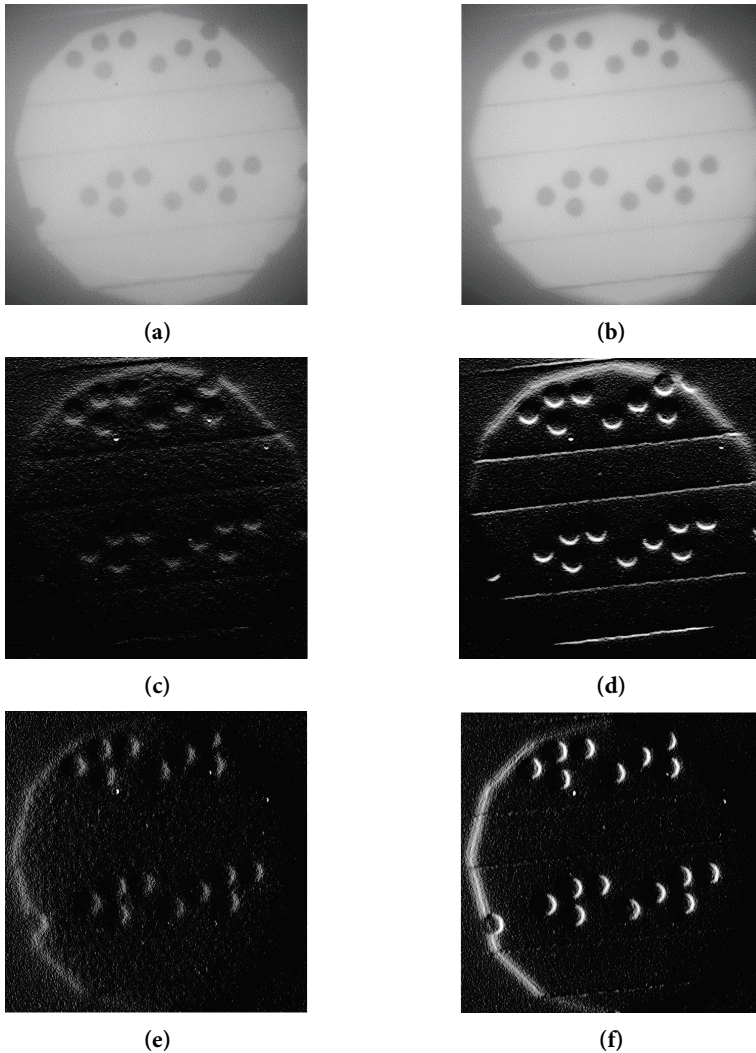
Figure 3.13: Comparison of an out of focus image (z = -10 μm) and a focused image (z = 0 μm). (a) The grey out of focus image. (b) The grey focused image. (c) f_{y^2} of the out of focus image. (d) f_{y^2} of the focused image. (e) f_{x^2} of the out of focus image. (f) f_{x^2} of the focused image.

Chapter 4

Measurement of the Internal Pressure of the Graphite Sealed Cavities

As mentioned in Chapter 1, to achieve the measurement of the activity of a single nanoparticle, we need to track the pressure inside the cavities. In this chapter, we will demonstrate how we can convert the resonance spectra to the internal pressures.

4.1 Resonance Spectra

The solid bottom chips produce typical resonance spectra as Figure 4.1 shows. The frequency at the peak is the resonance frequency of the graphite membrane. The spectrum is similar to those in previous studies [19, 39, 42].
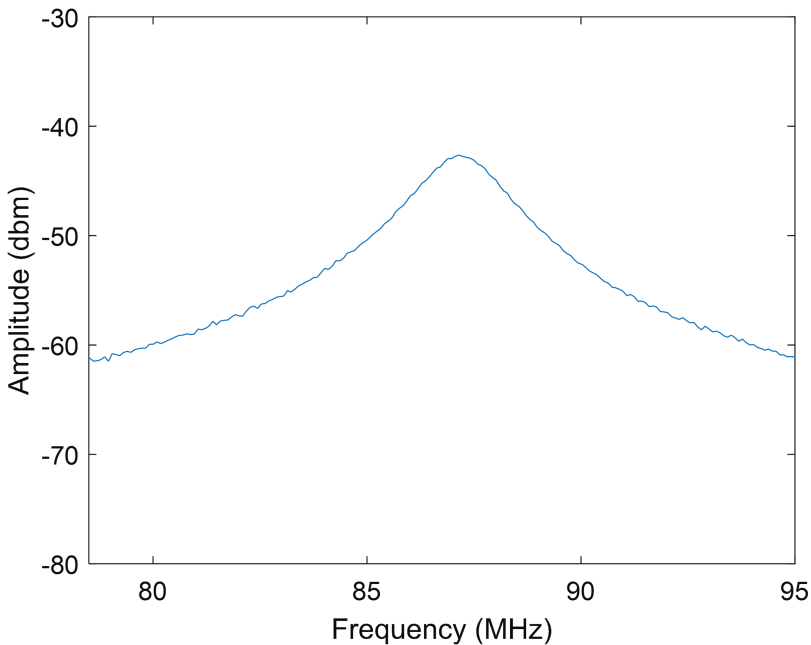
Figure 4.1: The spectrum of a solid bottom chip.

The spectra of the window chips have a unique double peak pattern. In the example in Figure 4.2, we can see two peaks. The peak at about 40 MHz, with a high quality factor (Q factor, describing how underdamped an oscillator is), is associated with the vibration of the SiO_2 window. The peak at about 115 MHz has a lower Q factor, and it is related to the graphite membrane, similar to the peak of the solid bottom chips.
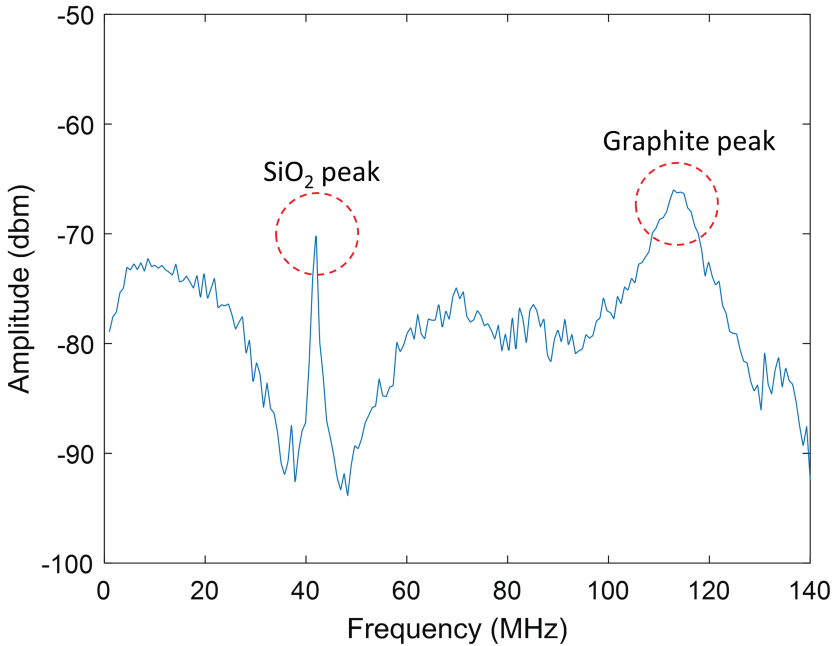
Figure 4.2: The spectrum of a window chip.

4.2   Pressure Sweep

As described in Section 3.4, converting the resonance frequency to the pressure difference across the membrane Δp with the theoretical model leads to a large error due to the uncertainty of the mechanical properties (i.e., Young's modulus and Poisson's Ratio) of the graphite membrane. Thus, we use a regression calibration to map the frequency-pressure relation. We evacuate the sample chamber to a series of pressures between 0 bar to 1 bar

absolute. The set of pressure-resonance frequency data is collected for the calculation. For most of our mechanical exfoliation samples, the time constants of their leakage are days, and therefore the leak during the calibration period (~10 minutes) is negligible. Assuming the internal pressure is 1 bar, we can get the nominal Δp by calculating the difference between the chamber pressure and the internal pressure.

Figure 4.3 shows an example of the pressure sweep of a solid bottom chip. It can be seen that there is an inflection point at about $\Delta p = 300$ mbar. When the Δp is above 300 mbar, the membrane tension is mainly dominated by the pressure-induced part in the equation (3.15) and (3.16), and we can see a third-order fit matches the data well in the interval [300 mbar, 1000 mbar]. For the interval [0 mbar, 300 mbar], the frequency mainly depends on the initial tension of the graphite membrane and thus the slope is relatively flat.
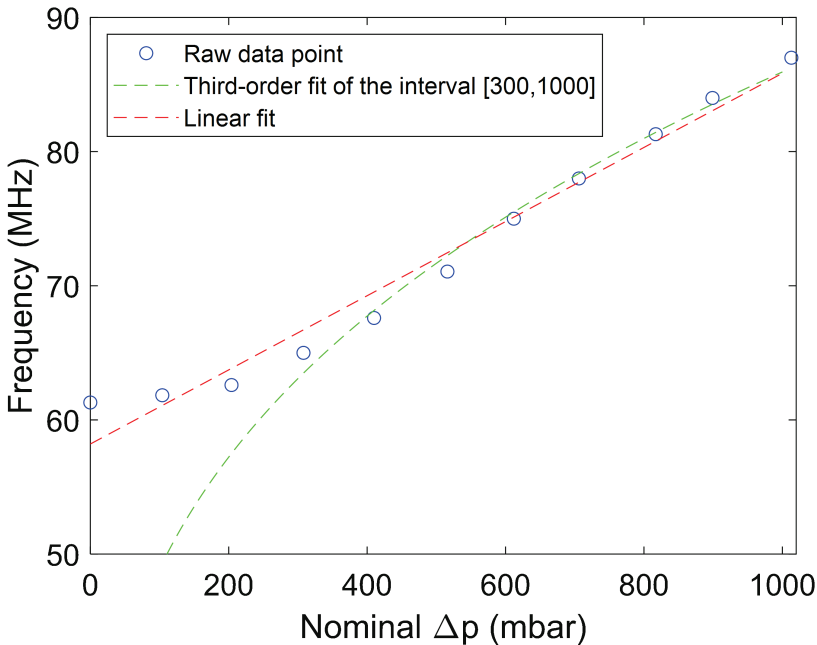
Figure 4.3: Pressure sweep of a cavity in a solid bottom chip.

For the windows chips, we have both a graphite resonance peak and a SiO$_2$ peak in their spectra. Figure 4.4 show an example of the pressure sweep of a PECVD window chip. The graphite pressure-frequency response is similar to that of the solid bottom chips, with two regions where the frequency mainly depends on the initial tension and the pressure-induced tension respectively. The SiO$_2$ pressure-frequency response has an unusual negative slope. The vibration model of the SiO$_2$ window is slightly different from the graphite, as it is thicker and a thin plate model with bending stiffness should fit it better than a membrane model. However, in both cases, the frequency should increase with Δp. In our newer batch of the window chips, whose SiO$_2$ windows were fabricated by a LPCVD process, the pressure-frequency response became positive. We conclude that a possible reason causing the inverse response is the residual thermal stress from the deposition process. The PECVD process is at 200 °C, whilst the LPCVD process is at 700 °C. After cooling down to room temperature, the temperature difference leads to a large difference in residual stress. Due to the lack of understanding of the physics behind the SiO$_2$ frequency, we only calculate pressure from the graphite frequency for the window chips.
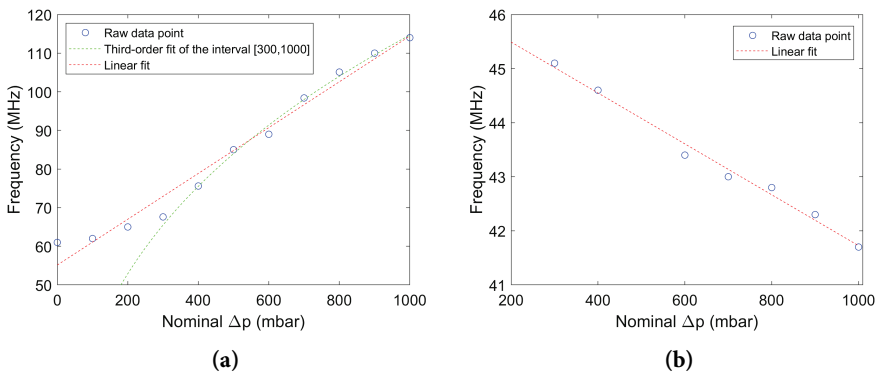
Figure 4.4: Pressure sweep of a cavity in a window chip. (a) Graphite frequency. (b) SiO$_2$ frequency.

4.3 Uncertainty of the Measurement

The uncertainty of the resonance measurement can be estimated by a regression fitting of the spectrum data. The curve can be fit by the Cauchy distribution (Figure 4.5) as follows:

$$p(f) = \frac{k}{\pi\gamma}\left[\frac{\gamma^2}{(f-f_0)^2+\gamma^2}\right] + d \tag{4.1}$$

where k is a scale factor; γ is the half-width at half-maximum; f_0 defines the location of the peak; and d specifies the vertical position of the curve. The uncertainty of the measurement is then given by the 95% confidence interval of the parameter f_0 from the curve fitting. Note that this only represents the uncertainty of a single measurement. That is, where the peak should be when we read the given data. There is also inter-measurement uncertainty, which indicates how the peak position varies from one measurement to another measurement. This kind of uncertainty needs to be evaluated by taking multiple measurements and observing the variance. Based on our experience, this is usually below 0.5 MHz.
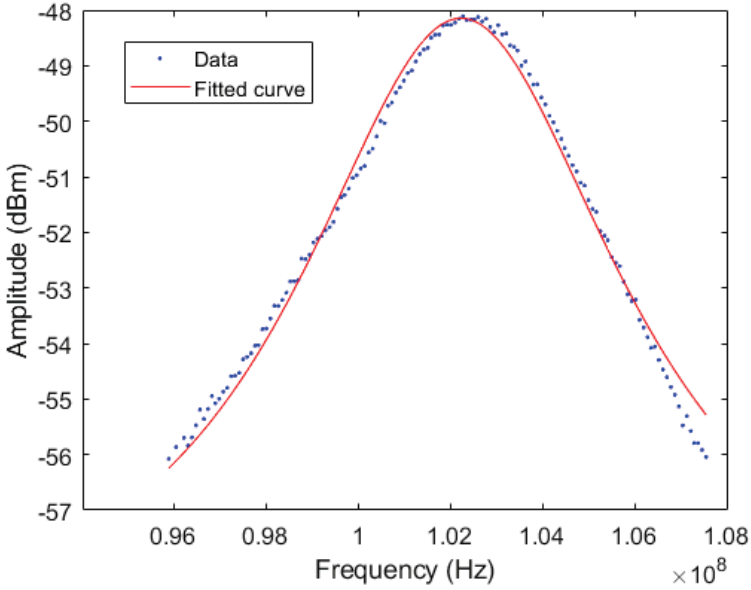
Figure 4.5: A spectrum fitting with Cauchy distribution.

4.4   Effect of Laser Heating

Heating by the laser may affect the accuracy of the measurement, as heated gas inside the cavity has a higher pressure according to the ideal gas law. In addition, when conducting catalysis research, the raised temperature can also significantly change the activity and create bias in the measurement.

Here we can investigate the heating effect by observing how the resonance frequency changes with input laser power. Considering a small element at the laser spot at the bottom of the cavity, the heat transfer equilibrium of the gas captured inside the cavity can be described as:

$$hA_{spot}(T_{spot} - T_{gas}) - hA_{wall}(T_{gas} - T_0)=0 \qquad (4.2)$$

Here we assume the area of the laser spot is A_{spot} and the temperature there is T_{spot}. For the rest part of the cavity surface (including the graphite membrane), the total area is A_{wall}, and the temperature is T_0. h is the heat transfer coefficient for the convection between the gas and cavity. The

temperature of the gas captured inside the cavity is T_{gas}. The equation reveals a linear relation between T_{spot} and T_{gas}.

To model the element at the laser spot, by simplifying the thermal conduction to a 1D case, we have:

$$Q_{laser} = hA_{conv}(T_{spot} - T_{gas}) + kA_{cond}\frac{dT}{dx} \qquad (4.3)$$

where Q_{laser} is the laser power absorbed by the element; A_{conv} is the area exposed to the gas for convection; k is the thermal conductivity of the element material (Si or SiO₂); A_{cond} is the cross section area of the 1D conduction model; and $\frac{dT}{dx}$ is the temperature gradient. Since the laser spot is a relatively small point compared with the entire chip, we can assume the bulk chip is an ideal heat sink at a constant temperature T_0, and at Δx from the laser spot, which modifies equation (4.3) to:

$$Q_{laser} = hA_{conv}(T_{spot} - T_{gas}) + kA_{cond}\frac{T_{spot}-T_0}{\Delta x} \qquad (4.4)$$

Combing equation (4.2) and (4.4), we can see that $\Delta T_{gas} \propto Q_{laser}$. Since ΔT_{gas} is also proportional to the pressure change inside the cavity Δp_{in}, the overall relationship means that the percentage change of the input laser power should be roughly linear correlated to the percentage change of the resonance frequency.

We examined three samples with different structure to investigate the heat effect, a SiO₂ solid bottom chip, a Si solid bottom chip, and a window chip as described in Section 2.1. All of the measured cavities on the chips capture 1 bar absolute air inside. Resonance frequencies are measured with two different laser powers: the maximal power that the setup can deliver (5.6 mW red laser and 1.2 mW blue laser), and the minimal power that allows us to measure the resonance frequency (0.8 mW red laser and 0.3 mW blue laser). The laser power is measured after passing through the objective lens, and there is a viewport between the measurement point and the sample. Since the quartz

viewpoint is coated with an antireflection coating, we can anticipate approximately 97% of the measured power delivered to the sample surface.

For the SiO_2 solid bottom chip and window ship, no change in resonance frequency was observed when switching from the low laser power to high laser power. Considering a 0.5 MHz uncertainty of the frequency measurement, the ΔT_{gas} should be less than 2 °C. For the Si solid bottom chip, the frequency change is 2 MHz, which corresponds to about 10 °C temperature change. Taking the linear relation between the laser power and ΔT_{gas} into account, we can obtain the following equations:

$$\frac{P_{max}}{P_{min}} = \frac{\Delta T_{max}}{\Delta T_{min}} \tag{4.5}$$

$$\Delta T_{max} - \Delta T_{min} = 10 \text{ °C} \tag{4.6}$$

where $P_{\max}$ and P_{min} are the maximal and minimal laser power respectively; ΔT_{max} and ΔT_{min} are the temperature increse at the maximal and minimal laser power respectively. By soliving the simple equations we see the total temperature rising should be approximately 12 °C.

The results of the heating test indicates that when the cavity bottom is made of SiO_2, the heating effect is generally negligible, and for the Si bottom cavities, a reduced laser power should be used. The different heat effects of different materials can also be reflected by their extinction coefficient of the refractive index. For Si the figure is 0.43 [57] at 633 nm, and for SiO_2, it is 1.67×10^{-3} [58].

Chapter 5

Investigation of the Leakage along the Graphite-SiO₂ Interface

5.1 Introduction

In the past decade, several studies have shown that a graphene membrane is impermeable to most standard gases [14, 16, 17, 60-62], except for H_2 which may transfer through monolayer graphene [60]. When a cavity with gas is sealed by graphene on a SiO_2 substrate, with a typical mechanical exfoliation transfer method, the gas leakage path is most likely through the interface between the graphene membrane and the SiO_2 substrate [14, 18, 63, 64], although we note that for He and H_2, it may also diffuse through the SiO_2 substrate [14, 65].

Previous experiments showed initial evidence that the leak rates of different gas species depend on the kinetic diameter (denoted by d) of the gas molecules [16, 17]. Koenig et al. [16] measured the leak rates of H_2, CO_2, Ar, N_2 and CH_4. There was a leak rate difference of a factor of ~100 between N_2 (d = 364 pm) and H_2 (d = 289 pm). Wang et al.[17] presented data of He, Ne, H_2, N_2O, CO_2, and Ar. The maximal selectivity in their dataset was between He (d = 260 pm) and Ar (d = 340 pm), which was about three orders of magnitudes. Here we expand the set of investigated gasses (N_2, O_2, CO, CO_2, Ar, H_2, He, CH_4, C_3H_6, NH_3, and SO_2) and make two primary findings: 1) For highly leak-tight samples there is a spread of multiple orders of magnitude from the least leaky gasses to the most leaky gasses, but they all scale in a deterministic way

---

[1] The chapter is adapted from the included manuscript submitted to the Journal of Chemical Physics [59].

so a measurement of one gas allows estimation of the rest. 2) Water-soluble gasses tend to have enhanced leak rates and "memory effects". Sometimes exposure to reactive gasses can affect the future leak rate of unreactive gasses.

5.2   Methods

In this study, we present four solid bottom chip samples (referred to as sample 1-4), with a 300 nm SiO_2 layer and 300 nm deep cavities. The diameter of the cavities of sample 1, 2, and 4 is 5 μm, and that of sample 3 is 4 μm.

The graphite membrane on sample 1, 2, and 3 were deposited by the mechanical exfoliation method, and for sample 4 the graphite was deposited by the PDMS method as described in Chapter 2.

Figure 5.1 illustrates our experimental process. After sealing in ambient air, the sample was measured in external vacuum, and a resonance frequency f_1 is obtained (Figure 5.1a). Then the samples were stored under vacuum for sufficiently long time (varying from days to a month, depending on their leak rates) in order to fully evacuate the cavities. A resonance frequency f_2 was then measured at 1 bar absolute external pressure (Figure 5.1b). Cavities must be essentially empty (i.e., full internal vacuum) if f_2 and f_1 are roughly identical since in both cases there is 1 bar pressure difference across the graphite membrane. After this confirmation, the sample chamber was filled with the gas of interest to 1 bar absolute pressure. As the gas subsequently leaks in, the pressure difference, and thus the resonance frequency, is reduced. The total amount of gas leaked into the cavity can be calculated as a function of time from the frequency change $f_2 - f_3(t)$ (Figure 5.1c). Between the measurement of the leak rate of different gases from the samples, the samples were stored under vacuum for a sufficiently long time to ensure that the cavities were essentially empty at the start of each measurement.
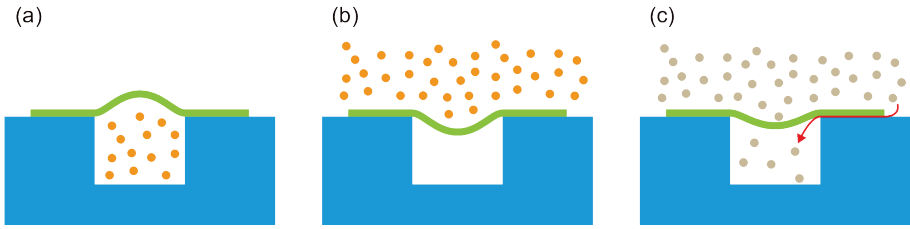
Figure 5.1: Schematic of the experiment process. (a) The initial state of the cavity, with 1 bar internal pressure where measurement of the resonance frequency under external vacuum gives f_1 corresponding to 1 bar Δp. (b) After evacuating the cavity, the cavity is measured with 1 bar external pressure, which yields a resonance frequency $f_2 \approx f_1$. (c) As time passes, gas leaks into the cavity and a new frequency f_3 is measured as a function of time.

In Figure 5.2, we present the experimental result for N_2 of sample 1 to illustrate how we calculated the leak rates from the raw data. Figure 5.2a shows how the resonance frequency changed over time. Figure 5.2b shows the leak rates calculated by both the first order fit and third order fit described above. Here, two different methods of calculating changes of pressure are also compared. The thin curves represent leak rates calculated from the pressure changes of adjacent points, and thus indicate real-time leak rates. The thick curves are calculated from the pressure difference from the start point to the moment that the point was measured, which indicates an average leak rate over the period. The leak rates of such a diffusion process are expected to be proportional to the (partial) pressure difference [17, 64, 66], and thus there should be an exponential decay of the pressure difference when gas leaks into the cavity. However, from Figure 5.2b we can see that there is generally little change of the real-time leak rate as Δp covers the interval from 1000 mbar to 700 mbar. The average leak rate goes more smoothly than the real-time leak rate, while providing basically the same figure as the real-time leak rate. Furthermore, the results calculated for the first order fit and third order fit are comparable for the first 20 minutes (corresponding to the working pressure

interval), which implies that it is reasonable to use the first order fit. The leak rates were calculated based on the average pressure change from t_0 as it provides a noise-free result.

(a)   (b)
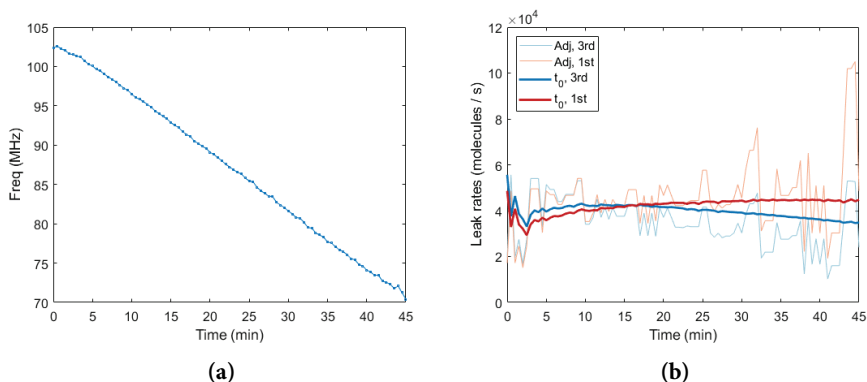
Figure 5.2: Measurement of N_2 leak rate of cavity 1. (a) The raw resonance frequency over time. (b) Calculated leak rates based on the frequency data. Adj, 3rd: calculated based on differences between adjacent data points with the third order fit. Adj, 1st: calculated based on differences between adjacent data points with the first order fit. t_0, 3rd: calculated based on differences from t_0 to the current data point with third order fit. t_0, 1st: calculated based on differences from t_0 to the current data point with first order fit.

5.3   Comparison of the Leak Rates of the Measured Gases

Figure 5.3 shows the leak rates measured from the four samples. For sample 1, measurement of the leak rate of air (ca. 1.000 molecules/s, green point in Figure 5.3) before and after exposure to NH_3 showed a significant increase in leak rate for air (to ca. 40.000 molecules/s). At this point all gasses (N_2, O_2, etc.) were measured (blue points in Figure 5.3). Then the sample was exposed to an SO_2/O_2 mix which again caused an increase in the leak rate of all gasses (orange points in Figure 5.3). Hence, both the leak rates before and after the O_2/SO_2 exposure are plotted here [1]. This memory effect of NH_3 or SO_2 exposure, however, is not universal since the other samples did not exhibit a

---

[1] The SO_2 leak rate data shown in Figure 5.3 is from 99.98% SO_2 after the exposure of the O_2/SO_2 mixture.

significant change in leak rate after the same exposure. Details of the exposures and re-measurement will be described in Section 5.4.

For an overview of all the samples, by taking N_2 as a reference, we can see sample 1 (Figure 5.3a) is initially medium leaky ($\sim 10^4$ molecules/s), sample 2 (Figure 5.3b), sample 3 (Figure 5.3c) are barely leaky (~ 100 molecules/s), and sample 4 (Figure 5.3d) is highly leaky ($\sim 10^6$ molecules/s). For the barely leaky samples, the leak rates of gases generally drop exponentially with increasing kinetic diameters of the gas molecules, except for the outlier SO_2 which exhibits much higher leak rates than the kinetic diameter-trend would suggest. Furthermore, we can also see a large span of leak rates (approximately 4 to 5 orders of magnitude) from the least leaky gas to the leakiest gas. For the medium leaky sample 1, the correlation between leak rates and kinetic diameters is much weaker as NH_3, CO_2, SO_2, CH_4, and C_3H_6 leak faster than their counterparts with similar diameters or the general trend. In comparison with the barely leaky samples, the leak-rate span of sample 1 is reduced to 2 orders of magnitude. Lastly, for the highly leaky sample 4, the correlation between leak rates and kinetic diameters is further weakened by some outliers, such as SO_2, CH_4, and especially C_3H_6, which despite having the largest kinetic diameter of the gases tested. It somehow has the second-highest leak rate on this sample. In general, the leak-rate span of sample 4 is the lowest among all the samples with every gas equal to within a factor of 4.
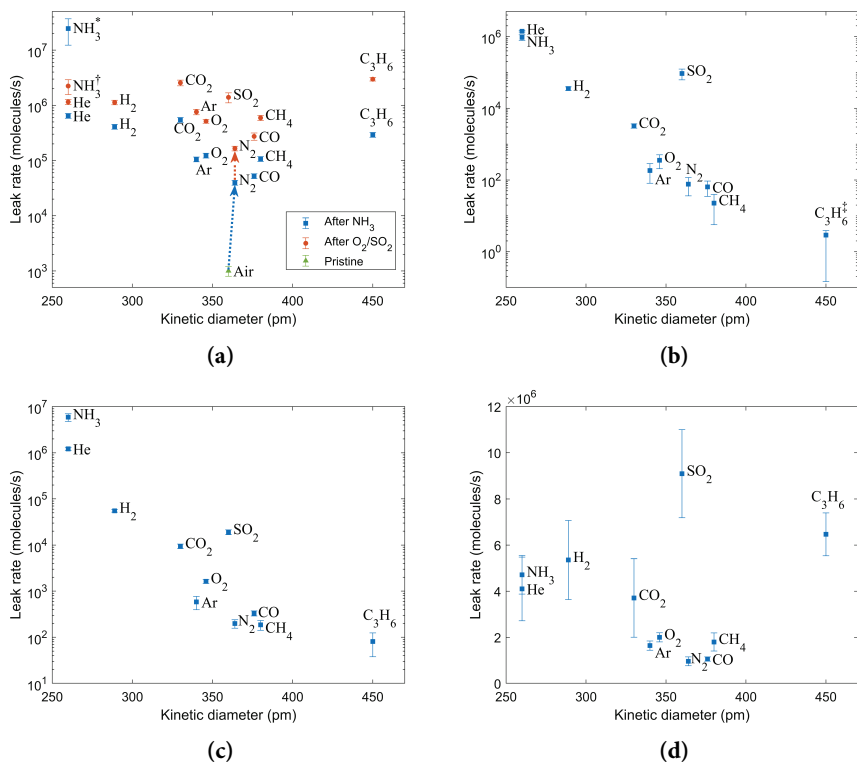
Figure 5.3: Leak rates of measured gases. Error bars are calculated based on the uncertainty of the frequency measurement. (a) Sample 1 (mechanical exfoliation). The leak rates changed significantly after being exposed to NH_3 and the O_2/SO_2 mixture. (b) sample 2 (mechanical exfoliation), (c) sample 3 (mechanical exfoliation), (d) sample 4 (PDMS).

Notes for special data points:

*: When measuring the NH_3 leak rate of sample 1 (before O_2/SO_2 exposure), the ΔP changed 1 bar in less than the sampling time (~3s). Thus the plot represents a leak rate corresponding to 1 bar / 3 s.

†: The NH_3 leak of sample 1 (after O_2/SO_2 exposure) has an induction period. The leak rate was calculated based on the slope after the induction period.

‡: For the C_3H_6 leak rate of sample 2, we could detect no frequency change for 5 days. The point on the plot thus is based on the maximal uncertainty of the resonance frequency measurement and it is possible that the true leak rate is zero.

Limited data about the molecular leak rate selectivity of graphene/graphite sealed cavities can be found in literature [16, 17], as a benchmark of porous graphene sheets for molecular sieving studies. In these previous works, however, only a single cavity or cavities covered by a single flake were presented so sample-to-sample variation could not be assessed. Here, by comparing the results of four individual samples with different baseline leak rates (N_2), we can see a cavity whose N_2 leak rate is low tends to provide higher molecular selectivity for insoluble gases, and vice versa. We use N_2 as the baseline because it is inert and leaks relatively slowly. Although leaking faster than N_2, we see that O_2 also has a stable relative position in the trend line for relative leak rates. This means that for a freshly sealed new sample, a simple measurement of the air leak rate should be able to provide a good prediction of its leak rates for the standard gases.

The correlation between the leak rates and the kinetic diameters also indicates that the leakage may follow the molecular sieve mechanism [16, 17, 64, 67]. The permeability coefficient of the molecular sieve mechanism can be described by the following equation [64, 67]:

$$P = k_0 \left(\frac{8}{\pi MRT}\right)^{\frac{1}{2}} e^{\frac{-E_{gas}}{RT}} \tag{5.1}$$

where k_0 is the structural parameter related to the geometry of the pores and the sizes of the molecules (i.e., kinetic diameters), E_{gas} is the activation energy of the gas, which describes the interaction between the gas molecule and the pore wall (i.e., graphite and SiO_2), M is the molecular mass, T is the temperature, and R is the gas constant. In fact, the permeability coefficient is highly dominated by the parameters k_0 and E_{gas}. When the equation is applied to thin, porous membranes, E_{gas} can be estimated by the density functional theory calculations [66, 68]. In the case of leakage through the graphite-SiO_2 interface, it is however extremely challenging to calculate both

k_0 and E_{gas}, as the leakage path can be long (a few μm), and the structure is unknown.

5.4 Measurement Chronology and Consistency

The measurements of all the samples and gases were taken over a period of four months. To ensure the leak rates are consistent over time, we repeated the measurements of certain gases.

Table 5.1 shows the full sequence of our measurement of all the gases. The O_2/SO_2 mixture was made by heating sulfur in O_2 at 250 °C for 60 minutes. The actual proportion of the mixture was not examined but we verified that a significant amount of SO_2 was generated by testing the pH of the product gas in a water solution. Figure 5.4 shows the leak rates of the gases that were measured multiple times. Sample 2, 3, and 4 have generally no drift of the leak rates over the period, whereas sample 1 has significant change as described in the last section. However, all samples tend to produce a lower resonance signal after the final NH_3 and SO_2 measurement. This might result from the reaction of NH_3 and SO_2 with moisture, which deposited ammonium sulfite on the graphite membrane and damped the resonance.

Table 5.1. Measurement sequence of the gases and samples. Experimental chronology is from top to bottom. Dataset 1 is the original sample. Dataset 2 is after NH₃ exposure. Dataset 3 is after O₂/SO₂ mixture exposure (same gas mixture from a single production is used for all the four samples). Dataset 4 is after SO₂ exposure.

		Sample			Dataset
	1	2	3	4	
	air	C_3H_6	He	N_2	
		CH_4	H_2	CO	
		CO_2	N_2	O_2	
		N_2	C_3H_6	CO_2	
		O_2	CH_4	Ar	1
		CO	O_2	CH_4	
		Ar	CO	H_2	
		He	Ar	He	
		H_2	CO_2		
	NH₃	**NH₃**	**NH₃**	**NH₃**	
	Air				
	N_2	He	He	C_3H_6	
	O_2			N_2	
	CO				
	CO_2				
Gas	Ar				2
	H_2				
	He				
	CH_4				
	C_3H_6				
	O₂/SO₂	**O₂/SO₂**	**O₂/SO₂**	**O₂/SO₂**	
	N_2	NH_3	NH_3	N_2	
	NH_3	He	CO_2		
	O_2	H_2			
	CO				
	CO_2				
	Ar				3
	H_2				
	He				
	CH_4				
	C_3H_6				
	SO₂	**SO₂**	**SO₂**	**SO₂**	
	N_2	NH_3	H_2	N_2	
	NH_3		NH_3	NH_3	4

Figure 5.4: Comparison of the leak rates from different measurements. S*x* in the legend represents sample *x*.

5.5   Induction Behavior of NH_3 Leakage of Sample 1

Sample 1 showed a special phenomenon which differs from other samples shown here. As mentioned above, it initially had a relatively low air leak rate (~1000 molecules/s). However, after it was exposed to NH_3, its leak rate was increased by about an order of magnitude (taking N_2 and O_2 for comparison with the air leak rate). We were not able to track its exact NH_3 leak rate because NH_3 filled the cavity too fast, in less than 3 seconds, which is a comparable time for filling the sample chamber and performing the first measurement. After it was exposed to SO_2, we observed that the leak rate of NH_3 was reduced into a range that we can measure, whereas the leak rates of other gases had increased dramatically. The relative leak rates (i.e., the ratio of one gas to another gas) of all gases (other than NH_3) are, however, still comparable to

their original rates. Such lasting effects of NH_3 and/or SO_2 exposure could perhaps be explained by a residual species inside the graphite-SiO_2 interface which are affected by NH_3 and SO_2. The alkaline or acidic gasses might for example interact with hydroxyl species on the SiO_2 surface and affect the van der Waal interaction between the chip and ultrathin graphite. Another noteworthy behavior of sample 1 is an induction period when NH_3 leaks into the cavity, which can be seen in Figure 5.5a. This was also observed in sample 2, after the O_2/SO_2 exposure. In Figure 5.5a, which shows data from sample 1, we can see that after the chamber was filled with NH_3, the resonance frequency of sample 1 (i.e., the internal pressure) remained stable for about 1.5 minutes (the induction period) before starting a rapid decline. After the cavity was filled with 1 bar NH_3, we pumped down the chamber at $t = 4$ minutes. The NH_3 then started to leak out of the cavity, but in this case, there was no induction period so NH_3 starts to leak out immediately. When we repeated this experiment, again filling the sample chamber with NH_3 shortly after the first experiment, the induction period for NH_3 ingression was reduced very significantly as Figure 5.5b shows. However, if instead of repeating the NH_3 exposure quickly, the sample is first kept under vacuum for an extended period (days), the original induction period occurs again. Clearly, the sample "remembers" the NH_3 exposure for some time, possibly due to NH_3 remaining bound under the graphite sheet interacting with the SiO_2 surface.
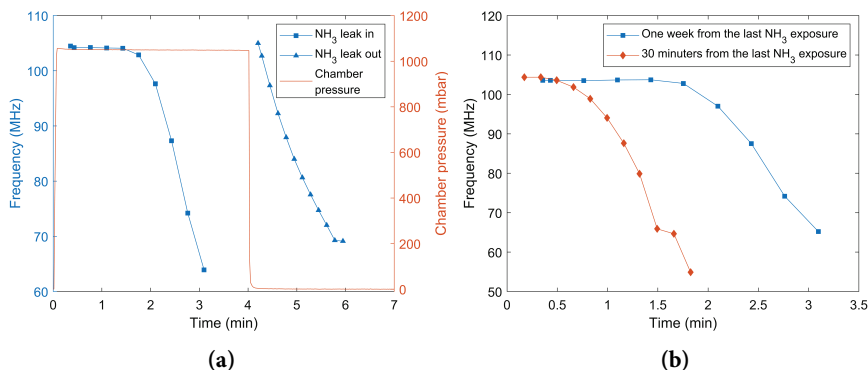
(a)   (b)

Figure 5.5: Induction behavior of sample 1 under NH$_3$ exposure. (a) co-plot of frequency and chamber pressure showing that (the first time after vacuum storage) there is a 1.5-minute delay from NH$_3$ exposure before frequency drop starts. (b) Comparison of the induction period recovery phenomenon for two different recovering times (vacuum storage). t=0 refers to the introduction of NH$_3$ in the sample chamber.

5.6   Discussion

The enhanced leak rates of NH$_3$ and SO$_2$ (i.e., much higher than those of other gases with similar kinetic diameters), and the induction period of NH$_3$ could indicate that some kind of water-like interlayer or conduit network exists at the graphite-SiO$_2$ interface. At the time of graphite sealing, the SiO$_2$ surface is almost certainly hydrophilic due to the oxygen plasma treatment. As we can see in these samples, water soluble gases (i.e., NH$_3$, SO$_2$ and perhaps CO$_2$) have higher leak rates than the non-soluble gases with similar kinetic diameters. Such gases might be able to "dissolve" into the graphite-SiO$_2$ interlayer at the chamber side of the water network, and re-evaporate at the cavity side facilitating mass-transport into the cavity. Such a water-like interlayer could explain the induction period seen for NH$_3$ leaks into the cavity and the changes of the leak rates. Once SO$_2$ is dissolved in water, it is mostly dissociated as HSO_3^- ($pK_a = 1.85$) [69], which means that a significant amount of SO$_2$ is dissolved permanently and does not evaporate when the SO$_2$ gas

concentration or pressure is reduced within the relevant time scale. By contrast, the dissociation constant of NH$_3$ is $pK_b = 4.75$ [69], so only a small fraction of NH$_3$ is converted to NH_4^+, and therefore NH$_3$ molecules can evaporate much faster under extended vacuum storage (explaining the recovery seen in Figure 5.5b). To recap the induction behavior, we start from the initial NH$_3$ leakage (Figure 5.6a). When the water layer is exposed to NH$_3$, NH$_3$ is dissolved at the chamber side, diffuses to the cavity side through the water, and evaporates at the cavity side. After the sample was exposed to SO$_2$, HSO_3^- stays in the water layer (Figure 5.6b). When NH$_3$ is dissolved in the water layer, the acidic solution drives its dissociation balance ($NH_3 + H_2O \rightleftharpoons NH_4^+ + OH^-$) to the NH_4^+ side. During the induction period, most of the dissolved NH$_3$ molecules are converted to NH_4^+, which cannot evaporate into the cavity. Once all the sulfurous acid has been neutralized, the NH$_3$ concentration in the water network rises, and enhanced diffusion into the cavity can therefore be established (Figure 5.6c).
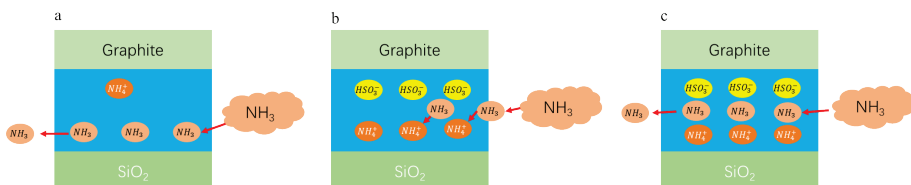
Figure 5.6: The interaction between NH$_3$ and SO$_2$. (a) The initial NH$_3$ leakage mechanism. NH$_3$ is dissolved at the chamber side and evaporates at the cavity side. Only a small amount of NH$_3$ is converted to NH_4^+. (b) After the SO$_2$ exposure, a significant amount of HSO_3^- stays in the water layer. Dissolved NH$_3$ is converted to NH_4^+, which causes the induction behavior. (c) When a balance between HSO_3^- and NH_4^+ is reached, NH$_3$ starts to evaporate at the cavity side.

5.7   Conclusion

In conclusion, we observed that the leak rates of most gas molecules permeating into graphite sealed SiO$_2$ cavities correlate with the kinetic

diameters of the gas molecules. The molecular selectivity can be correlated with the N_2 leak rates, which implies that the selectivity can be tunable by adjusting the baseline leak rate, for instance by changing graphite transfer method. In addition, we observe that water soluble molecules tend to have enhanced leak rates, which indicates that hydrated channels likely exist at the graphite-SiO_2 interface. Whether the water assists the sealing should be investigated in future research. Finally, hydrocarbon gases which ordinarily have very low leak rates showed high leak rates in certain cases. The reason for the occasional high hydrocarbon leak rate is unclear.

Chapter 6

Investigation of the Leakage through the SiO₂ Substrate

6.1 Introduction

In this chapter, we will present two experiments. One measured the He and H_2 leak rates on two windows chips, and the other measured the H_2 leak rate on a solid bottom chip. The motivation is to investigate whether the small molecules have significant diffusion through the SiO_2 substrate, namely the TEM window and the thermal SiO_2 layer. However, since the small molecules also leak through the graphite-SiO_2 interface quickly, we cannot credibly distinguish a leak rate from the two leakage mechanisms, and the results only provide tentative evidence that the diffusion through SiO_2 has a significant impact on the overall leak rate.

6.2 The Leakage through the TEM Window

The leak rates of He and H_2 were measured from two window chip samples, one with a PECVD SiO_2 window and the other with a LPCVD SiO_2 window. The graphite flakes on both samples were transferred by the mechanical exfoliation method. Figure 6.1 illustrates the experimental process. Initially the sample captured 1 bar absolute air inside the cavity, and a frequency f_1 was measured with a vacuum pressure outside (Figure 6.1a). Then the sample chamber was filled with 1 bar absolute tested gas. We assume that the leak is driven by the partial pressure of each gas species, which means the captured gas would not slow down the flow of the tested gas into the cavity and vice versa. Since the leak rate of the air (mainly N_2 and O_2) is much slower than those of the measured gases, we can neglect the leak of the air out of the cavity

for the short experiment period. Therefore, after the experiment period t, the total pressure inside the cavity becomes the sum of the initial air pressure and the leaked gas into the cavity (Figure 6.1b). Then the chamber was quickly pumped down to vacuum again and a new frequency f_2 was measured. The difference from f_1 to f_2 can corresponds to the partial pressure of the gas leaked into the cavity.
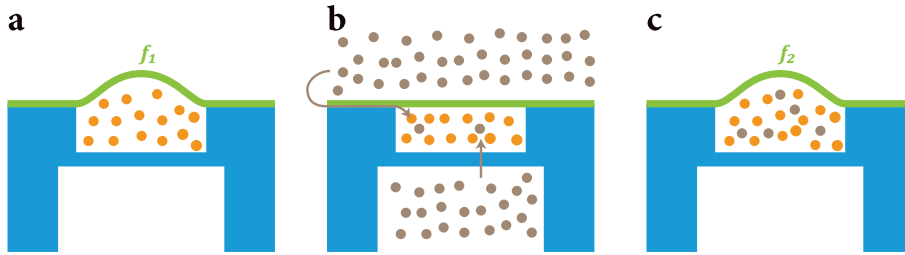

Figure 6.1: Schematic of the experiment process. (a) The initial state of the cavity, with 1 bar internal pressure where measurement of the resonance frequency under external vacuum gives f_1 corresponding to 1 bar Δp. (b) The sample chamber is filled with 1 bar absolute tested gas. The gas leaks into the cavity through the graphite-SiO$_2$ interface and the SiO$_2$ window. (c) The sample chamber is pumped down to vacuum, which gives a Δp corresponding to the sum of the air partial pressure and the tested gas partial pressure ($\Delta p = p_{air} + p_{gas}$). A new frequency f_2 is measured for calculating the leak rate.

The results of the measurements are shown in Figure 6.2. The leak rates of the two solid chips (referred to as solid chip 1 and 2, which corresponds to sample 1 and 3 in Chapter 5 respectively) is also plotted here for comparison. First, we compare the leak rate of solid chip 2 and the PECVD sample. The air and H$_2$ leak rates of the two samples are generally similar, but the He leak rate of the PECVD sample is 10 times faster than that of the solid chip 2. The result indicates that the extra He leak rate may be the He diffusion through the PECVD SiO$_2$ window. H$_2$ is also possible diffuse through SiO$_2$ [65, 70], but here the diffusion is negligible in comparison with the leak through the graphite-SiO$_2$ interface.

The LPCVD sample gave extraordinarily high H_2 and He leak rates. Its air leak rate is slightly higher than those of solid chip 2 and the PECVD sample, but much lower than that of solid chip 1. However, the H_2 leak rate of the LPCVD sample is even greater than that of the leaky solid chip 1 by a factor of 10. For the He leak rate the LPCVD sample is one and two orders of magnitudes faster than the PECVD sample and the solid chips respectively. This may imply that both He and H_2 can diffuse through the LPCVD SiO_2 window, and the diffusivities are much higher (one or two orders of magnitudes) than the PECVD SiO_2.
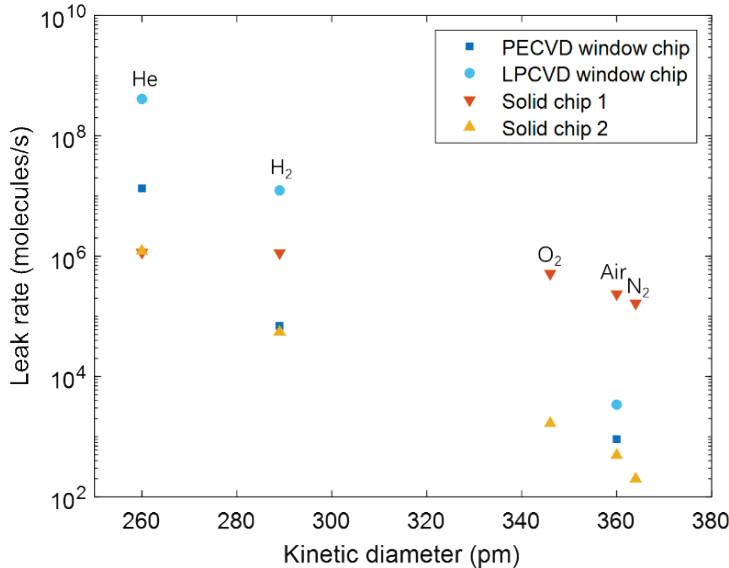
Figure 6.2: Comparison of the leak rates of the two window chips and two solid chips (sample 1 and 3 in Chapter 5). The kinetic diameter of air is estimated as $d_{air} = 0.8d_{N_2} + 0.2d_{O_2}$.

In conclusion, the experiment reveals that the diffusion of He (for both LPCVD and PECVD) and H_2 (for LPCVD) through the SiO_2 windows can significantly affect the leak rate of the cavities. However, the inference is based on single samples and several unconfirmed assumptions, a more rigorous

protocol (e.g., emptying the cavities like the experiment in Chapter 5) and statistical analysis are needed in future investigation. He is an inert gas which the ATOMICAR project will not use. H_2 is however an important gas in many reactions (e.g., hydrogen oxidation and hydrogen evolution), which are critical to the green hydrogen industry for the green transition. Therefore, it is of importance to understand the H_2 diffusion for further ATOMICAR research.

6.3 H_2 Leakage through the SiO_2 Substrate

To investigate the potential H_2 leakage through the SiO_2 substrate, we measured the leak rates from six cavities on a solid chip, whose optical image and scanning electron microscope (SEM) image are shown in Figure 6.3. The cavities are 380 nm deep. The diameters of cavities 1, 3, 5 are 4 μm, and the diameters of cavities 2, 4, 6 are 5 μm. The sample is one of the most leak tight samples we have measured (air leak rates are about 100 molecules/s for the measured cavities), which minimize the H_2 leakage through the graphite-SiO_2 interface and allow us to observe the diffusion through the SiO_2 substrate. The experiment protocol is similar to the one in Section 6.2 (see Figure 6.1), but after measuring f_2, the frequencies were kept being tracked for a period.
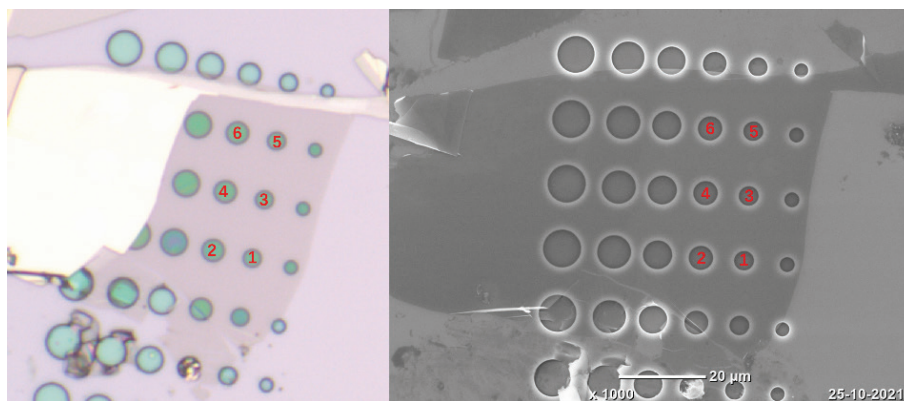

Figure 6.3: Optical image and SEM image of the sample.

Figure 6.4 shows the result of the experiment. The initial frequencies f_1 were measured at $t = 0$ min. Then the sample chamber was filled with 1 bar absolute H_2 for 4 hours. After the period, we observed that the frequencies of cavities 1, 2, 3, 5, 6 were increased, whereas the frequency of cavity 4 did not have a significant change. These frequency increases indicates that H_2 leaked into the cavities and led to a greater Δp across the membrane. After the chamber was pumped down to vacuum, we would expect that the frequencies drop as the gases (both air and H_2) leak out. However, we can see the frequencies actually kept on increasing for a period and then started to drop. This phenomenon may be attributed to the H_2 diffusion through the SiO_2 substrate. Figure 6.5 depicts the process. When the chamber was filled with 1 bar H_2, H_2 leaked into the cavity both through the graphite-SiO_2 interface and the SiO_2 substrate (Figure 6.5a). With the H_2 diffusion through the SiO_2 substrate, the H_2 molecules were dissolved into the SiO_2 substrate. Then when the chamber was pumped down to vacuum, the dissolved H_2 still stayed in the SiO_2 substrate, and outgas into the chamber and the cavities with a rate faster than the H_2 leak through the graphite-SiO_2 interface, which resulted in an increase of the resonance frequency. As the H_2 concentration in SiO_2 was reduced, the rate of the outgas was reduced. When the rate of the outgas is lower than the leak rate through the graphite-SiO_2 interface, the resonance frequency started to reduce.
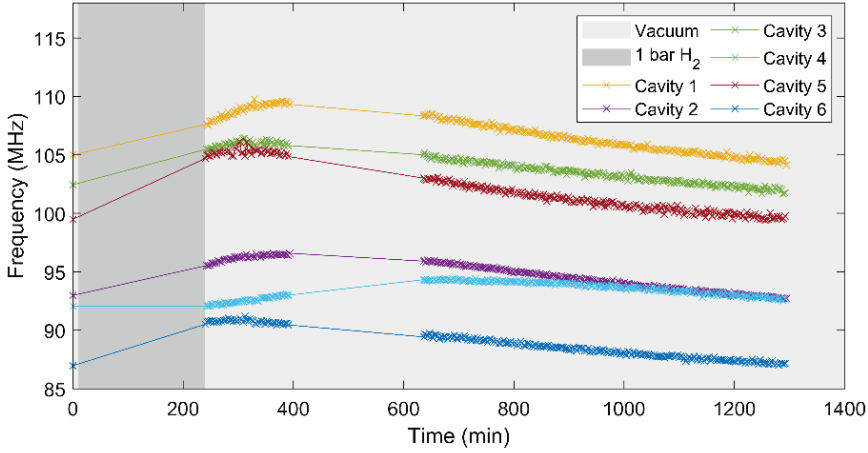
Figure 6.4: Frequency versus time. The chamber was in vacuum at the interval $t/\min = [0, 10] \cup [240, 1400]$. The chamber was filled with 1 bar H_2 at the interval $t/\min = [10, 240]$.
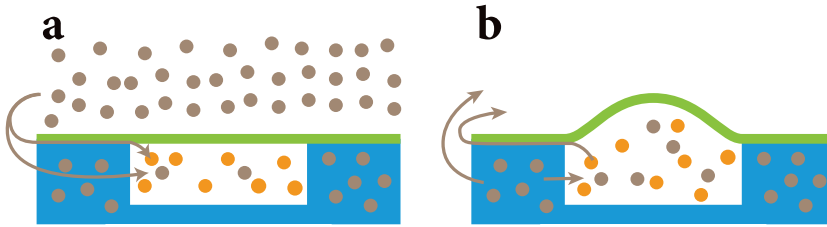
Figure 6.5: Schematic diagram of the H_2 diffusion in SiO_2. (a) H_2 leaks into the cavity through the graphite-SiO_2 interface and the SiO_2 substrate. (b) When the chamber is pumped down to vacuum, H_2 in the cavity leaks out through the graphite-SiO_2 interface, and part of the residual H_2 is released to the cavity.

To verify the diffusion hypothesis, we can compare the frequency change during the 1 bar H_2 period Δf, and the peak time of the cavities, with the diffusion distance (the distance from the ambient H_2 to the cavity) of each cavity. Unfortunately, the frequencies at the interval $t/\min = [400, 620]$ were not tracked because the spectrum analyzer lost connection, but we can still estimate when the frequency of each cavity reached its maximum based on the recorded data. The Δf and the peak time dependences of the diffusion

distance are plotted in Figure 6.6. The trend lines reveal that as a cavity is located further from the H_2 source (i.e., the nearest uncovered SiO_2 surface), its frequency increased less after the 4-hour H_2 exposure, and it took a longer time to reach its maximal frequency. This trend matches the diffusion hypothesis, as the H_2 diffusion in SiO_2 is a relatively slow process at room temperature, and it takes time for the H_2 molecules to reach a far cavity.
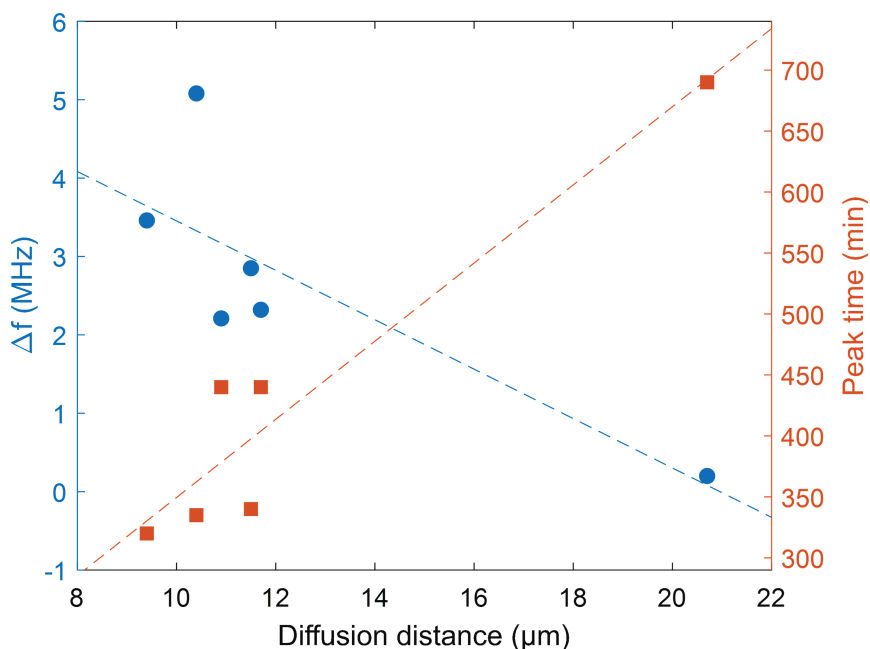
Figure 6.6: The change in frequency from $t = 0$ min to $t = 240$ min, and the peak time versus diffusion distances. The diffusion distances are measured from the optical image and SEM image as the distance from a cavity to the edge of the graphite flake or the nearest partially covered cavity. The trend lines are linear fits of the data.

In conclusion, we demonstrated that H_2 could leak into the cavities through the SiO_2 substrate. However the experiment has several limitations:

● The cavities have different sizes, which leads to different frequency-pressure responses (about 20% error).

- A piece of data was not recorded.
- The leak rate through the graphite-SiO_2 interface is unclear and may affect the interpretation of the result.

A more rigorous experiment, with cavities of the same size in an array, can be conducted in the future to verify the results. Despite the limitations, the observed leak rate is relatively slow. For window chips, the leak through the SiO_2 window should be much higher than the substrate as the diffusion path is much shorter. Consequently, the H_2 leakage through the SiO_2 substrate could be neglected in further ATOMICAR catalysis research.

Chapter 7

Measurement of the Cavity Leak Rates at High-Temperature Condition

7.1   Background

Previous studies have shown that graphite/graphene-sealed SiO_2 cavities are generally impermeable to air [14-18, 63], in spite of a small leak rate which is likely through the graphite-SiO_2 interface [14, 18, 63]. All the previous studies were conducted at room temperature, and to our knowledge, there is currently no report about the impermeability of the graphite/graphene-sealed SiO_2 cavities under high-temperature conditions.

Here we present the leak rate data of a graphite-sealed SiO_2 solid bottom cavity at up to 175 °C. The sample was relatively leak tight (with a leak rate ca. 100 molecules / s) at room temperature (25 °C), and the leak rate became about 100 times faster than its initial leak rate. The sample became leak tight again after it was cooled down.

7.2   Methods

The sample was fabricated from a (100) silicon wafer. Firstly, a 2000 nm SiO2 layer was grown by a wet thermal oxidation process. Then the structures of the cavities (5μm-diameter circle) were defined by a UV lithography process and the cavities were fabricated by a 380 nm deep reactive ion etching through the SiO2 layer. The graphite membrane was deposited by the typical mechanical exfoliation method [20, 71], as described in Chapter 2.

To examine the leak rate, we used the laser interferometry setup to measure the resonance frequency of the graphite membrane. In a previous study [72], Davidovikj et. al. showed that, after heating a FLG nanodrum 25 K

above ambient temperature, due to the increased membrane tension, the sample can get about 1.5 MHz increase in the resonance frequency. Therefore, considering the change in frequency and also the increased internal pressure after heating (ideal gas law), converting the resonance frequency to the internal cavity pressure may be inaccurate. We will only compare the frequency change over time instead of calculating the leak rate at elevated temperatures.

7.3   Temperature Calibration

The heater structure is shown in Figure 7.1. The sample is placed on a small invar plate (1 cm × 1 cm). On the back side of the invar plate, a resistance wire and a type K thermocouple are spotwelded on it. The resistance wire generates heat and transfer the heat to the invar plate. Since the invar plate is small, we can presume it has an even temperature distribution. The thermocouple measures the temperature of the invar plate and provides a signal to the heater controller for regulating the temperature.

Figure 7.1: The heater structure.
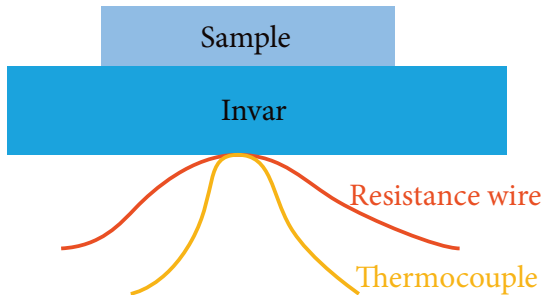
Obviously, the sample does not have the same temperature as the invar plate, due to limited thermal conductivity between them. We therefore used a forward-looking infrared (FLIR) camera to calibrate the temperature. First, we placed a silicon wafer with the same SiO_2 layer thickness as the sample, on a hotplate (Figure 7.2). A thermocouple was attached on the wafer surface to

probe its temperature. We used the FLIR camera to observe the wafer through a germanium window. The germanium window was used because it is transparent to infrared and we used it as a viewport in the next step. By calibrating the FLIR camera with the thermocouple readout, we obtained an emissivity of 0.65 for the silicon wafer through the germanium window.
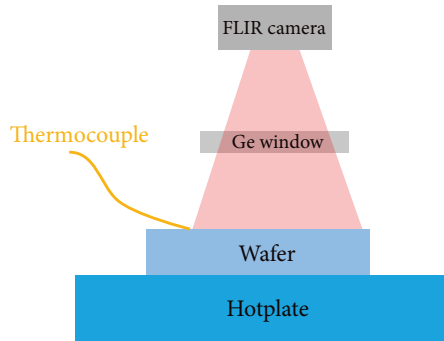
Figure 7.2: Calibrate the emissivity.

After calibrating the emissivity, we used the germanium window to close the sample chamber and pump down the chamber to vacuum (Figure 7.3). We tuned the invar plate at different temperatures and measures the corresponding sample temperature by the FLIR camera. The results of the measurement are shown in Table 7.1, which allows us to convert the thermocouple readout to the actual sample temperature. Note that in the rest of the chapter, we will use the controller setpoint to present our experiment temperatures (unless otherwise stated), and the controller regulated the temperature based on the thermocouple readouts. This is because we were not able to use the FLIR camera to measure the sample during the experiment (for the laser measurement we use a quartz viewport, which is opaque to infrared, instead of the germanium window). However we can refer to Table 7.1 when we need to know the actual temperature of the sample.
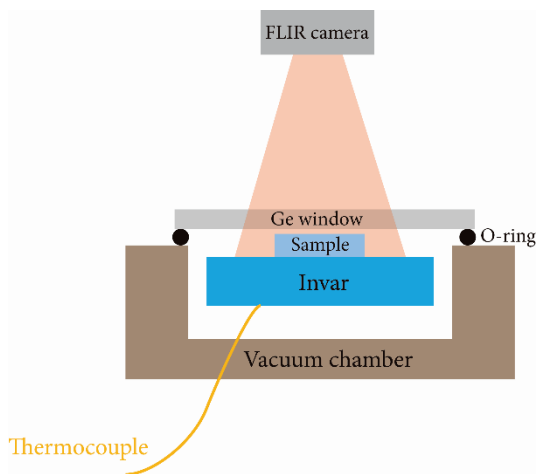
Figure 7.3: Mapping the thermocouple readout to the FLIR measurement.

Table 7.1: The temperature measured by the thermocouple and the FLIR camera.

Thermocouple (°C)	FLIR (°C)
100	80
110	86
120	91
130	99
140	105
150	113
160	120
170	127

7.4 Measurement of the Leak Rate at Room Temperature and 160 °C

We first measured the leak rate at room temperature for a reference. Prior to the measurement, the sample had not been heated after transferring the graphite flake on it by the mechanical exfoliation method. The sample, which captured about 1 bar air, was placed in the vacuum chamber (<1 mbar) during the measurement. This leads to 1 bar pressure difference across the membrane, and we can observe that the resonance frequency dropped while the air leaked out. The result is shown as the blue curve in Figure 7.4. The leak rate is about 0.01 MHz/min ($\approx$ 100 molecules / s).
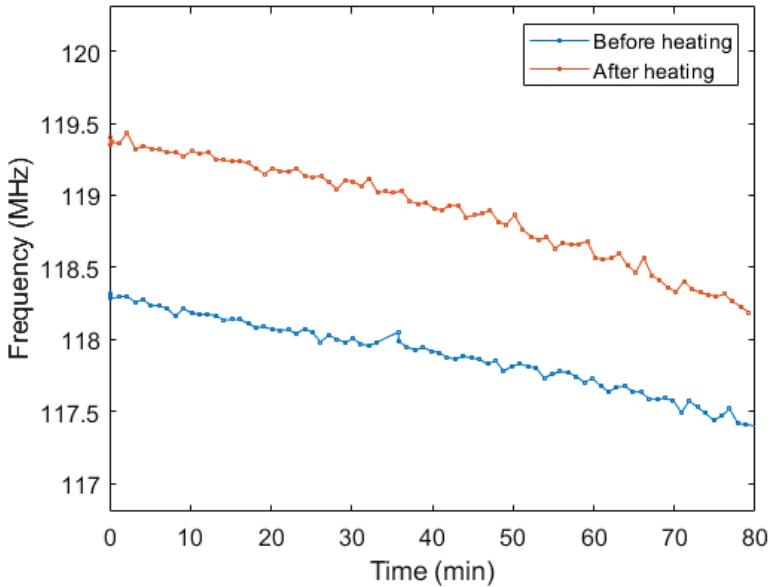
Figure 7.4: Comparison of the leak rates before and after the heating experiment.

Figure 7.5 shows the frequency change of the sample at 160 °C controller setpoint. At t = 0 min, the sample was at 25 °C, and at t = 4 min, the invar plate reached 160 °C. We can observe a small increase in the resonance frequency due to expanded gas and the thermal stress of the graphite membrane. Note that graphite/graphene has a negative in-plane thermal expansion coefficient ($-8 \times 10^{-6}\ K^{-1}$ for SLG) [73], which results in a significantly increased tension when heated up, as it deforms against the SiO_2 substrate which has a positive thermal expansion coefficient. After the temperature became stable at 160 °C, the resonance frequency started to decline quickly. For the interval t/min = [4, 25], the average change rate of the frequency was about 1.2 MHz/min, which is roughly 100 times faster than the rate at room temperature. The total amount of gas leaking out during the period is approximately 0.4 bar. At t = 27 min, we filled the chamber with 1 bar air while keeping the temperature at 160 °C. Then the resonance frequency reflected a $\Delta p \approx$

0.4 bar. For the period t/min = [27, 75], air leaked back into the cavity and the frequency gradually reduced to the value corresponding to $\Delta p \approx 0\ bar$. The experiment reveals that the heating condition can significantly increase the leak rate of the graphite-sealed cavity, and the leak can happen in both ways (in and out) with similar rates.
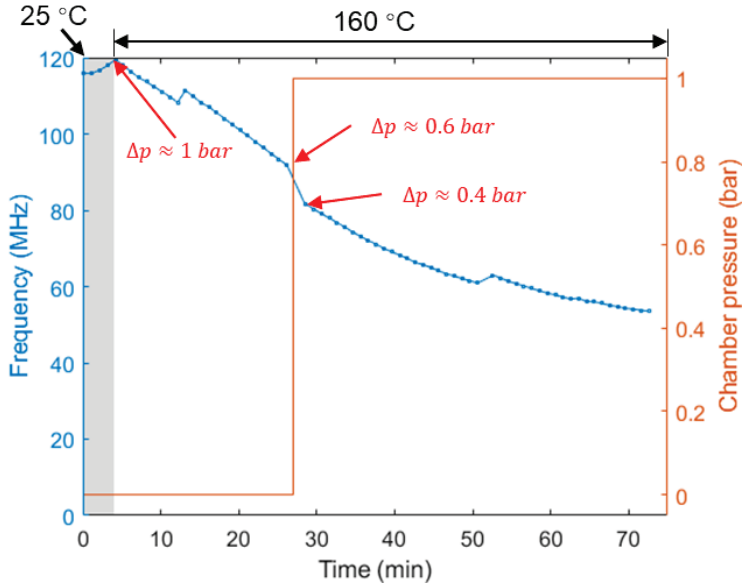
Figure 7.5: Frequency versus time at 160 °C. The grey background indicates the heating up period, from 25 °C (t = 0 min) to 160 °C (t = 4 min). The temperature in the white background area was constant at 160 °C.

After this heating experiment, we let the sample cool down and store it in ambient conditions so that the internal pressure can recover to 1 bar. Then we repeat the leak test at room temperature (red curve in Figure 7.4). The leak rate was generally comparable to that before the heating experiment. However, we observed changes in its resonance spectra although the fundamental frequency changed at the same rate. Figure 7.6 shows the spectra before and after the heating experiment. The pristine spectrum consists of generally a clear fundamental peak, and a secondary peak at a higher frequency. For the

spectrum after heating, we can see three extra peaks with frequencies lower than the fundamental frequency. This may indicate that ripples or wrinkles were formed during the heating process, which leads to an uneven tension distribution over the membrane and creates multiple peaks. The phenomenon can be attributed to the negative graphite thermal expansion coefficient described previously, which resulted in dislocations at the graphite-SiO_2 interface. We observed the same behavior in most of our samples that had been heated. For the samples whose graphite/graphene flakes were transferred by mechanical exfoliation or PDMS method, they usually initially had clean single peak spectra. After heating, multiple peaks can be observed. However, samples made by CAB transfer method usually have initially multi-peak spectra. As the CAB transfer comprises a heat treatment process (up to 135°C), this further proves that heating processes cause the multi-peak spectra.

(a)   (b)
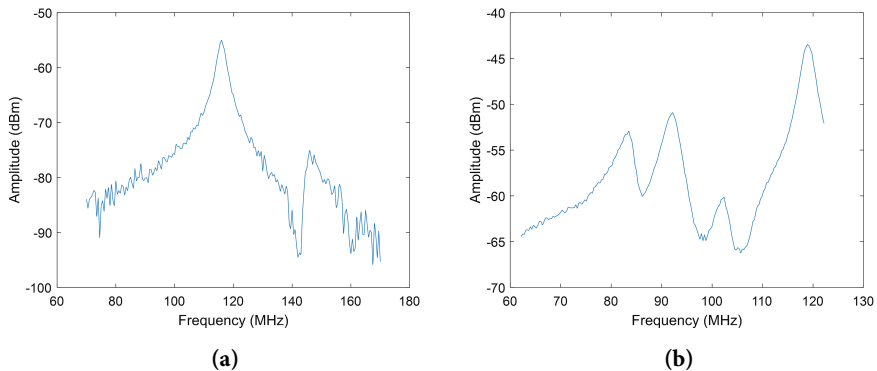
Figure 7.6: The spectra before and after the sample was heated at 160 °C. (a) The spectrum before the heating experiment. (b) The spectrum after the heating experiment.

7.5   Comparison of the Leak Rate at Different Temperatures

To investigate how the leak rate changes with the temperature, we measured the leak rates at a series of temperatures (50°C to 175 °C). The result is shown in Figure 7.7. When the invar heater temperature is below 100 °C, the frequency curve was generally flat. When the heater temperature reached

125 °C (the sample was approximately 95 °C, according to Table 7.1), the leak rates started to increase significantly. After this critical temperature, the leak rates further increased as the temperature increased. The frequency change rates were 0.05, 0.08, and 0.11 MHz/min at 125, 150, and 175 °C respectively.
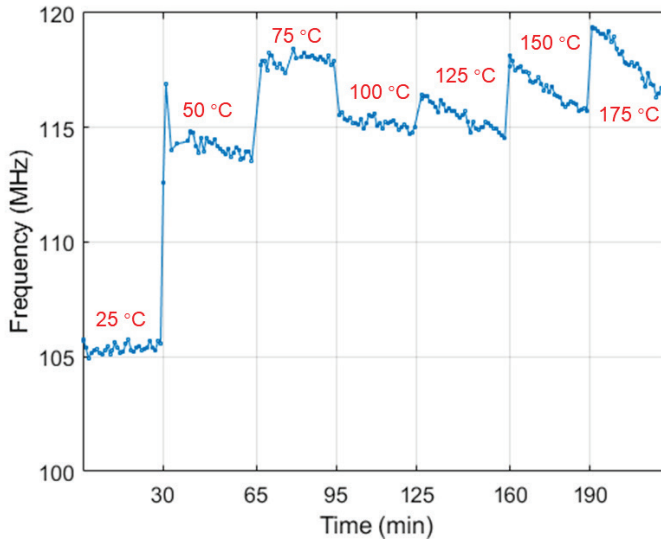
Figure 7.7: Frequency versus time at different temperatures.

Note that the frequency change rates in the second heating test at 150 and 175 °C, were approximately one tenth of the value in the first measurement at 160 °C, but were still larger than the rate at room temperature by a factor of 10. We therefore repeated the leak test four times to verify the repeatability. The results of all the six measurements are compiled in Figure 7.8. After a significant drop from the first to the second measurement, the leak rates became generally stable but with a small trend to decrease as the number of heating times increased. When the sample was heated for the first time, the thermal stress could create considerable dislocation at the graphite-SiO_2 interface, which became gas channels for the leakage. However, from the second time that it was heated, the graphite flake might be redistributed and

had a better fit to the SiO$_2$ surface at high temperatures. Consequently, the leak rates at high temperature were reduced as the improved graphite adhesion removed the leak channels.
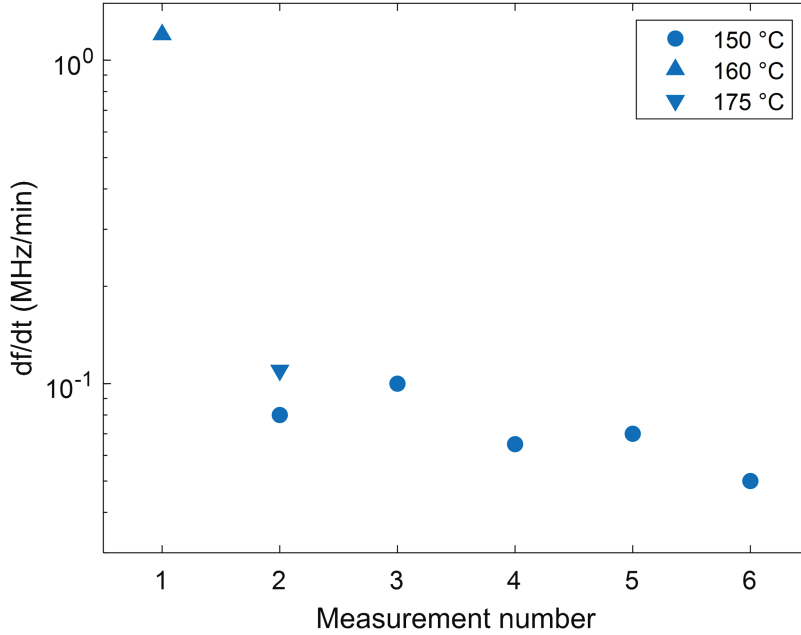
Figure 7.8: Compilation of the measured frequency change rates $\frac{df}{dt}$.

7.6 Conclusions

In this chapter, we have presented leak rate data of a solid bottom chip at room temperature and elevated temperatures at up to 175 °C. The leak rates in the heated condition (around 150 °C to 175 °C), were 10 to 100 times faster than the leak rate at room temperature for the same cavity. The leak rates at the high temperature also reduced, from 100 times of the room temperature leak rate in the first heating measurement, to 10 times and lower as it was heated multiple times. The actual mechanism behind the increased leak rates is unclear, but might be caused by the dislocation at the graphite-SiO$_2$ interface.

We also checked the leak rates at different temperatures between 50 °C to 175 °C, with a step of 25 °C. The result reveals that the leak rates increased significantly at about 125 °C (corresponding to ca. approximately 95 °C sample temperature) for the measured sample. This threshold is however not universal as we observed different thresholds from some of other samples that we have measured at high temperature. Most of the thresholds were around 100 °C to 200 °C, and the highest record is 300 °C, detected by the EELS measurement on a window chip. These leak rate data provide important information for the further ATOMICAR research about thermal catalysis, as most of the reactions need to be activated by heat.

Chapter 8
Conclusion

8.1   Summary

This thesis explored the permeability of graphite sealed SiO_2 cavities by using the HSCACS. Chapter 1-4 included the basic concepts, principles, and techniques related to the experiments presented in the thesis. Chapter 1 introduced the ATOMICAR project. Chapter 2 described the structure of the ATOMICAR chips and how we transfer graphene and graphite flake to the chips. Chapter 3 showed the design and theories of the HSCACS, which is able to track the resonance frequencies of cavities in an array automatically. Most experiments were however based on single cavities, but the scanning function was utilized in the experiment in Section 6.3. Chapter 4 introduced the methods about the measurement of the internal pressures of the cavities.

The results of the experiments were presented and discussed in Chapter 5, 6, and 7. The experiments in Chapter 5 measured leak rates of a number of gasses (N_2, O_2, CO, CO_2, Ar, H_2, He, CH_4, C_3H_6, NH_3, and SO_2) at room temperature. The results revealed that the gas leak rates can be correlated to the gas kinetic diameters, except for the water-soluble gases and hydrocarbons. Furthermore, the selectivity for gas leak rates can be correlated to a reference gas leak rate (e.g., N_2) for each sample. This finding would allow us to predict the selectivity of a new device by a single measurement of the reference gas. We also observed that water-soluble gasses tend to have extraordinarily high leak rates, which indicates that water may exist on the leakage path. The water hypothesis provides important information for further investigation of the leaking mechanism.

The experiments in Chapter 6 investigated the He and H_2 diffusion through the SiO_2 layer (both the TEM window and the cavity wall) of the ATOMICAR chips. The measurements of the window chips implied that He could diffuse through the TEM window quickly and the diffusion rates were higher than the leakage through the graphite-SiO_2 interface. For H_2, elevated leak rates were observed from the LPCVD window chip, but not the PECVD window chip. H_2 leak rates were also measured from a solid bottom chip in Chapter 6. The sample performed a delayed filling effect. That is, after stored in 1 bar H_2 for 4 hours, we observed that the internal pressure of the cavities slightly increased for a period, while the sample chamber was in vacuum. The behavior can be explained by an outgassing process of the H_2 dissolved in the SiO_2 substrate. The time scale and diffusion rate are however relatively trivial, and would have little effect on the catalysis experiments.

In Chapter 7, we integrated a heating element into the sample chamber and measured the gas leak rate at high temperatures up to 175 °C (heater temperature). We first observed that the leak rate at about 160 °C was increased by a factor of 100 in comparison with the room temperature leak rate, and the leak tightness was recovered when the samples were cooled down to room temperature. When we repeated the heating experiment, the leak rates at high temperature were reduced to about 10 times of that at room temperature, and tended to slightly further reduce. These changes might be due to the negative thermal expansion coefficient of the thin graphite membrane, which resulted in high thermal stress and dislocation at the graphite-SiO_2 interface when the sample was heated. We also conducted experiments at a series of temperatures between 50 °C to 175 °C, with steps of 25 °C. We discovered that the threshold where the sample became leaky is 125 °C (heater temperature, corresponding to about 95°C sample

temperature). The threshold is however not consistent when we measured other samples (not presented here), and our highest record is about 300 °C.

8.2 Outlook

The thesis presented promising results about the impermeability of the graphite-sealed cavities. However, the ultimate ATOMICAR goal (i.e., measuring catalytic activity of a single nanoparticle) is still somewhat in the distance. The main issue is the leakage at elevated temperatures and unpredictable graphite seal behavior. Extra experiments under heating conditions need to be performed in order to obtain statistically significant answers about the correlation between the leak rates and the temperatures. Whether different graphite transfer methods affect the performance at a high temperature is also unclear and should be investigated.

In Chapter 5, we have shown the correlation between the gas leak rates and the kinetic diameters of the gas molecules. Each measurement in the study was based on a single gas species. Therefore an important future work is to investigate the leak rates of gas mixtures, because for heterogeneous catalytic research, gas mixtures are almost certainly inevitable. If the leaking mechanism is based on the partial pressure of each individual gas, the leak rate of a mixture should be simply a weighted arithmetic mean of the leak rate of each gas component based on their kinetic diameters. However, we need further experiments to verify this hypothesis.

The results in Chapter 5 also indicates the possibility to predict the leak rates of different gases of a new sample, by a single measurement of a reference gas. The ideal reference gas is N_2. Since the cavities are usually sealed in air, air can be a more convenient choice, if we can confirm the leak rates of gas mixtures scale in the same way as pure single gases. Future work about this part will be to evaluate the accuracy of the prediction (either by N_2 or air). A

successful prediction will provide a convenient way to calibrate the leak rate of a cavity array in the catalytic measurements. There are some cavity-to-cavity variations in the leak rates, observed both in our experiments and previous studies [14, 63]. A catalytic measurement without calibration would not allow us to distinguish whether the change of the internal pressure in a cavity is due to an active nanoparticle or the native leakage of the cavity. Hence, it is necessary to know the leak rate of each reactant gas and product gas prior to a catalytic measurement. Measuring the leak rates of the reactant gases and product gases is risky as a super active nanoparticle (this is also what ATOMICAR is looking for) may drive the reaction even at room temperature. Therefore, predicting the leak rates of the reactive gases by measuring an inert gas will be very useful for the calibration work.

The HSCACS used for measuring the gas leak rates is capable of scanning a cavity array automatically. Currently the laser spot marking and the initial cavity matching steps have to be done manually but can be easily upgraded to automatic functions in future versions. To find the laser spot, we can simply extract the red component from the color picture and identify a circle on it in the same way as finding the cavities. The initial cavity matching is a slightly challenging task, even for the robotics and automation industry [74]. My old robotic vacuum cleaner bought in 2019 is not even able to know its initial position if I place it at a random location instead of its charger, although it has a navigation function which creates a map of my apartment automatically (I see newer advanced robotic cleaner can detect initial position now). The way to localize the initial location of the chip is to extract the cavity features from the image and match them with the cavity layout on the map. The actual implementation can be done by several different algorithms [75-79], but all the concepts are generally based on minimizing the "distance" between the

actual features and features on the map, which usually takes expensive computational cost. An alternative solution is to define some "landmarks" (e.g., triangles and squares) on the chips, and the task is simplified to recognize these simple shapes.

Lastly, to reach the initial ATOMICAR goal (i.e., scanning thousands of cavities and find active nanoparticles), we will need a 2D material transfer method which can cover a large area and make a satisfactory seal. Graphene or ultrathin graphite from natural graphite crystals can hardly produce a good yield, and CVD graphene is highly leaky. We are currently attempting to use CVD MoS_2 membrane in collaboration with Associate Professor Scott Bunch at Boston University. The CVD MoS_2 can cover a mm^2 size area and the initial measurements have shown promising leak rates at room temperatures. Some further measurements will be conducted to verify the feasibility of using the MoS_2 membrane.

References

[1]   J. J. Dolhun, "Observations on manganese dioxide as a catalyst in the decomposition of hydrogen peroxide: a safer demonstration," *Journal of Chemical Education,* vol. 91, no. 5, pp. 760-762, 2014.

[2]   S. Wacławek, V. V. Padil, and M. Černík, "Major advances and challenges in heterogeneous catalysis for environmental applications: a review," *Ecological Chemistry and Engineering S,* vol. 25, no. 1, pp. 9-34, 2018.

[3]   G. Tiao, G. Box, and W. Hamming, "Analysis of Los Angeles photochemical smog data: a statistical overview," *Journal of the Air Pollution Control Association,* vol. 25, no. 3, pp. 260-268, 1975.

[4]   H. Güsten, "Formation, transport and control of photochemical smog," in *Air Pollution*: Springer, 1986, pp. 53-105.

[5]   I. Chorkendorff and J. W. Niemantsverdriet, *Concepts of modern catalysis and kinetics.* John Wiley & Sons, 2017.

[6]   A. Schmid, J. Dordick, B. Hauer, A. Kiener, M. Wubbolts, and B. Witholt, "Industrial biocatalysis today and tomorrow," *nature,* vol. 409, no. 6817, pp. 258-268, 2001.

[7]   F. Wang, J. D. Harindintwali, Z. Yuan, M. Wang, F. Wang, S. Li, Z. Yin, L. Huang, Y. Fu, and L. Li, "Technologies and perspectives for achieving carbon neutrality," *The Innovation,* vol. 2, no. 4, p. 100180, 2021.

[8]   S. Chen, S. Perathoner, C. Ampelli, and G. Centi, "Electrochemical dinitrogen activation: To find a sustainable way to produce ammonia," in *Studies in surface science and catalysis*, vol. 178: Elsevier, 2019, pp. 31-46.

[9]   J. Wisniak, "The history of catalysis. From the beginning to Nobel
        Prizes," *Educación química,* vol. 21, no. 1, pp. 60-69, 2010.

[10]   J. B. Sambur and P. Chen, "Approaches to single-nanoparticle
        catalysis," *Annual Review of Physical Chemistry,* vol. 65, pp. 395-422,
        2014.

[11]   S. Franssila, *Introduction to microfabrication*. John Wiley & Sons, 2010.

[12]   Y. Fang and Y. He, "Resolution technology of lithography machine," in
        Journal of Physics: Conference Series, 2022, vol. 2221, no. 1: IOP
        Publishing, p. 012041.

[13]   P. Rai-Choudhury, *Handbook of microlithography, micromachining,
        and microfabrication: microlithography*. SPIE press, 1997.

[14]   J. S. Bunch, S. S. Verbridge, J. S. Alden, A. M. Van Der Zande, J. M.
        Parpia, H. G. Craighead, and P. L. McEuen, "Impermeable atomic
        membranes from graphene sheets," *Nano letters,* vol. 8, no. 8, pp. 2458-
        2462, 2008.

[15]   S. P. Koenig, N. G. Boddeti, M. L. Dunn, and J. S. Bunch, "Ultrastrong
        adhesion of graphene membranes," *Nature nanotechnology,* vol. 6, no.
        9, p. 543, 2011.

[16]   S. P. Koenig, L. Wang, J. Pellegrino, and J. S. Bunch, "Selective
        molecular sieving through porous graphene," *Nature nanotechnology,*
        vol. 7, no. 11, pp. 728-732, 2012.

[17]   L. Wang, L. W. Drahushuk, L. Cantley, S. P. Koenig, X. Liu, J.
        Pellegrino, M. S. Strano, and J. S. Bunch, "Molecular valves for
        controlling gas phase transport made from discrete ångström-sized
        pores in graphene," *Nature nanotechnology,* vol. 10, no. 9, pp. 785-790,
        2015.

[18]   M. Lee, D. Davidovikj, B. Sajadi, M. Sˇisˇkins, F. Alijani, H. S. van der Zant, and P. G. Steeneken, "Sealing graphene nanodrums," *Nano letters,* vol. 19, no. 8, pp. 5313-5318, 2019.

[19]   D. Davidovikj, J. J. Slim, S. J. Cartamil-Bueno, H. S. van der Zant, P. G. Steeneken, and W. J. Venstra, "Visualizing the motion of graphene nanodrums," *Nano letters,* vol. 16, no. 4, pp. 2768-2773, 2016.

[20]   K. S. Novoselov, A. K. Geim, S. V. Morozov, D.-e. Jiang, Y. Zhang, S. V. Dubonos, I. V. Grigorieva, and A. A. Firsov, "Electric field effect in atomically thin carbon films," *science,* vol. 306, no. 5696, pp. 666-669, 2004.

[21]   A. Bianco, H.-M. Cheng, T. Enoki, Y. Gogotsi, R. H. Hurt, N. Koratkar, T. Kyotani, M. Monthioux, C. R. Park, and J. M. Tascon, "All in the graphene family–A recommended nomenclature for two-dimensional carbon materials," vol. 65, ed: Elsevier, 2013, pp. 1-6.

[22]   A. Castellanos-Gomez, M. Buscema, R. Molenaar, V. Singh, L. Janssen, H. S. Van Der Zant, and G. A. Steele, "Deterministic transfer of two-dimensional materials by all-dry viscoelastic stamping," *2D Materials,* vol. 1, no. 1, p. 011002, 2014.

[23]   G. F. Schneider, V. E. Calado, H. Zandbergen, L. M. Vandersypen, and C. Dekker, "Wedging transfer of nanostructures," *Nano letters,* vol. 10, no. 5, pp. 1912-1916, 2010.

[24]   P. Blake, E. Hill, A. Castro Neto, K. Novoselov, D. Jiang, R. Yang, T. Booth, and A. Geim, "Making graphene visible," *Applied physics letters,* vol. 91, no. 6, p. 063124, 2007.

[25]   G. A. McQuade, A. S. Plaut, A. Usher, and J. Martin, "The thermal expansion coefficient of monolayer, bilayer, and trilayer graphene

derived from the strain induced by cooling to cryogenic temperatures," *Applied Physics Letters,* vol. 118, no. 20, p. 203101, 2021.

[26]   G. Deokar, J. Avila, I. Razado-Colambo, J.-L. Codron, C. Boyaval, E. Galopin, M.-C. Asensio, and D. Vignaud, "Towards high quality CVD graphene growth and transfer," *Carbon,* vol. 89, pp. 82-92, 2015.

[27]   B. Deng, Z. Liu, and H. Peng, "Toward mass production of CVD graphene films," *Advanced Materials,* vol. 31, no. 9, p. 1800996, 2019.

[28]   R. Munoz and C. Gómez-Aleixandre, "Review of CVD synthesis of graphene," *Chemical Vapor Deposition,* vol. 19, no. 10-11-12, pp. 297-322, 2013.

[29]   W. Gao, L. B. Alemany, L. Ci, and P. M. Ajayan, "New insights into the structure and reduction of graphite oxide," *Nature chemistry,* vol. 1, no. 5, pp. 403-408, 2009.

[30]   W. Gao, "The chemistry of graphene oxide," in *Graphene oxide*: Springer, 2015, pp. 61-95.

[31]   E. Moreau, F. Ferrer, D. Vignaud, S. Godey, and X. Wallart, "Graphene growth by molecular beam epitaxy using a solid carbon source," *physica status solidi (a),* vol. 207, no. 2, pp. 300-303, 2010.

[32]   J. M. Garcia, U. Wurstbauer, A. Levy, L. N. Pfeiffer, A. Pinczuk, A. S. Plaut, L. Wang, C. R. Dean, R. Buizza, and A. M. Van Der Zande, "Graphene growth on h-BN by molecular beam epitaxy," *Solid State Communications,* vol. 152, no. 12, pp. 975-978, 2012.

[33]   M. Gao, Y. Pan, L. Huang, H. Hu, L. Zhang, H. Guo, S. Du, and H.-J. Gao, "Epitaxial growth and structural property of graphene on Pt (111)," *Applied Physics Letters,* vol. 98, no. 3, p. 033101, 2011.

[34] V. L. Nguyen and Y. H. Lee, "Towards wafer-scale monocrystalline graphene growth and characterization," *Small,* vol. 11, no. 29, pp. 3512-3528, 2015.

[35] Z. Su, X. Sun, X. Liu, J. Zhang, L. Sun, X. Zhang, Z. Liu, F. Yu, Y. Li, and X. Cheng, "A strategy to prepare high-quality monocrystalline graphene: Inducing graphene growth with seeding chemical vapor deposition and its mechanism," *ACS applied materials & interfaces,* vol. 12, no. 1, pp. 1306-1314, 2019.

[36] W. Wiszniewski, R. Collins, and B. Pailthorpe, "Mechanical light modulator fabricated on a silicon chip using SIMOX technology," *Sensors and Actuators A: Physical,* vol. 43, no. 1-3, pp. 170-174, 1994.

[37] D. W. Carr, L. Sekaric, and H. G. Craighead, "Measurement of nanomechanical resonant structures in single-crystal silicon," *Journal of Vacuum Science & Technology B: Microelectronics and Nanometer Structures Processing, Measurement, and Phenomena,* vol. 16, no. 6, pp. 3821-3824, 1998.

[38] D. Karabacak, T. Kouh, and K. Ekinci, "Analysis of optical interferometric displacement detection in nanoelectromechanical systems," *Journal of Applied Physics,* vol. 98, no. 12, p. 124309, 2005.

[39] J. S. Bunch, A. M. Van Der Zande, S. S. Verbridge, I. W. Frank, D. M. Tanenbaum, J. M. Parpia, H. G. Craighead, and P. L. McEuen, "Electromechanical resonators from graphene sheets," *Science,* vol. 315, no. 5811, pp. 490-493, 2007.

[40] R. J. Dolleman, D. Davidovikj, S. J. Cartamil-Bueno, H. S. van der Zant, and P. G. Steeneken, "Graphene squeeze-film pressure sensors," *Nano letters,* vol. 16, no. 1, pp. 568-571, 2015.

[41]   J. S. Bunch, *Mechanical and electrical properties of graphene sheets*. Citeseer, 2008.

[42]   A. Castellanos-Gomez, R. van Leeuwen, M. Buscema, H. S. van der Zant, G. A. Steele, and W. J. Venstra, "Single-Layer MoS2 Mechanical Resonators," *Advanced Materials,* vol. 25, no. 46, pp. 6719-6723, 2013.

[43]   H. Anders, "Thin films in optics," *London: Focal Press,* 1967.

[44]   T. G. Mackay and A. Lakhtakia, "The transfer-matrix method in electromagnetics and optics," *Synthesis lectures on electromagnetics,* vol. 1, no. 1, pp. 1-126, 2020.

[45]   N. H. Asmar, *Partial differential equations with Fourier series and boundary value problems*. Courier Dover Publications, 2016.

[46]   S. S. Rao, *Vibration of continuous systems*. John Wiley & Sons, 2019.

[47]   C. Lee, X. Wei, J. W. Kysar, and J. Hone, "Measurement of the elastic properties and intrinsic strength of monolayer graphene," *science,* vol. 321, no. 5887, pp. 385-388, 2008.

[48]   J. Lee, Z. Wang, K. He, J. Shan, and P. X.-L. Feng, "High frequency MoS2 nanomechanical resonators," *ACS nano,* vol. 7, no. 7, pp. 6086-6091, 2013.

[49]   Y. Ma, G. Wang, Y. Chen, D. Long, Y. Guan, L. Liu, and Z. Zhang, "Extended Hencky solution for the blister test of nanomembrane," *Extreme Mechanics Letters,* vol. 22, pp. 69-78, 2018.

[50]   J.-U. Lee, D. Yoon, and H. Cheong, "Estimation of Young's modulus of graphene by Raman spectroscopy," *Nano letters,* vol. 12, no. 9, pp. 4444-4448, 2012.

[51]   J.-W. Jiang, J.-S. Wang, and B. Li, "Young's modulus of graphene: a molecular dynamics study," *Physical Review B,* vol. 80, no. 11, p. 113405, 2009.

[52] F. Memarian, A. Fereidoon, and M. D. Ganji, "Graphene Young's modulus: Molecular mechanics and DFT treatments," *Superlattices and Microstructures,* vol. 85, pp. 348-356, 2015.

[53] A. Sakhaee-Pour, "Elastic properties of single-layered graphene sheet," *Solid State Communications,* vol. 149, no. 1-2, pp. 91-95, 2009.

[54] E. R. Davies, *Machine vision: theory, algorithms, practicalities*. Elsevier, 2004.

[55] T. J. Atherton and D. J. Kerbyson, "Size invariant circle detection," *Image and Vision computing,* vol. 17, no. 11, pp. 795-803, 1999.

[56] J. M. Geusebroek, F. Cornelissen, A. W. Smeulders, and H. Geerts, "Robust autofocusing in microscopy," *Cytometry: The Journal of the International Society for Analytical Cytology,* vol. 39, no. 1, pp. 1-9, 2000.

[57] D. T. Pierce and W. E. Spicer, "Electronic structure of amorphous Si from photoemission and optical studies," *Physical Review B,* vol. 5, no. 8, p. 3017, 1972.

[58] L. V. Rodríguez-de Marcos, J. I. Larruquert, J. A. Méndez, and J. A. Aznárez, "Self-consistent optical constants of SiO2 and Ta2O5 films," *Optical Materials Express,* vol. 6, no. 11, pp. 3622-3637, 2016.

[59] Y.-X. Liu, H. R. Ambjørner, T. G. Bonczyk, E. Dollekamp, L. M. Kaas, and P. C. K. Vesborg, "Gas Permeation Rates of Ultrathin Graphite Sealed SiO2 Cavities," *The Journal of Chemical Physics,* Submitted.

[60] P. Sun, Q. Yang, W. Kuang, Y. Stebunov, W. Xiong, J. Yu, R. Nair, M. Katsnelson, S. Yuan, I. Grigorieva, M. Lozada-Hidalgo, F. Wang, and A. Geim, "Limits on gas impermeability of graphene," *Nature,* vol. 579, no. 7798, pp. 229-232, 2020.

[61] V. Berry, "Impermeability of graphene and its applications," *Carbon,* vol. 62, pp. 1-10, 2013.

[62] O. Leenaerts, B. Partoens, and F. Peeters, "Graphene: A perfect nanoballoon," *Applied Physics Letters,* vol. 93, no. 19, p. 193107, 2008.

[63] Y. Manzanares-Negro, P. Ares, M. Jaafar, G. Lopez-Polin, C. Gomez-Navarro, and J. Gomez-Herrero, "Improved graphene blisters by ultrahigh pressure sealing," *ACS Applied Materials & Interfaces,* vol. 12, no. 33, pp. 37750-37756, 2020.

[64] T. Tsuru, R. Igi, M. Kanezashi, T. Yoshioka, S. Fujisaki, and Y. Iwamoto, "Permeation properties of hydrogen and water vapor through porous silica membranes at high temperatures," *AIChE journal,* vol. 57, no. 3, pp. 618-629, 2011.

[65] R. Lee, R. Frank, and D. Swets, "Diffusion of hydrogen and deuterium in fused quartz," *The Journal of Chemical Physics,* vol. 36, no. 4, pp. 1062-1071, 1962.

[66] S. Blankenburg, M. Bieri, R. Fasel, K. Müllen, C. A. Pignedoli, and D. Passerone, "Porous graphene as an atmospheric nanofilter," *Small,* vol. 6, no. 20, pp. 2266-2271, 2010.

[67] A. Shelekhin, A. Dixon, and Y. Ma, "Theory of gas diffusion and permeation in inorganic molecular-sieve membranes," *AIChE Journal,* vol. 41, no. 1, pp. 58-67, 1995.

[68] J. P. Thiruraman, S. A. Dar, P. Masih Das, N. Hassani, M. Neek-Amal, A. Keerthi, M. Drndić, and B. Radha, "Gas flow through atomic-scale apertures," *Science Advances,* vol. 6, no. 51, p. eabc7927, 2020.

[69] D. R. Lide, *CRC handbook of chemistry and physics*. CRC press, 2004.

[70]   C. Leiby Jr and C. Chen, "Diffusion coefficients, solubilities, and permeabilities for He, Ne, H2, and N2 in Vycor Glass," *Journal of Applied Physics,* vol. 31, no. 2, pp. 268-274, 1960.

[71]   K. S. Novoselov, D. Jiang, F. Schedin, T. Booth, V. Khotkevich, S. Morozov, and A. K. Geim, "Two-dimensional atomic crystals," *Proceedings of the National Academy of Sciences,* vol. 102, no. 30, pp. 10451-10453, 2005.

[72]   D. Davidovikj, M. Poot, S. J. Cartamil-Bueno, H. S. van der Zant, and P. G. Steeneken, "On-chip heaters for tension tuning of graphene nanodrums," *Nano letters,* vol. 18, no. 5, pp. 2852-2858, 2018.

[73]   D. Yoon, Y.-W. Son, and H. Cheong, "Negative thermal expansion coefficient of graphene measured by Raman spectroscopy," *Nano letters,* vol. 11, no. 8, pp. 3227-3231, 2011.

[74]   H. Sobreira, C. M. Costa, I. Sousa, L. Rocha, J. Lima, P. Farias, P. Costa, and A. P. Moreira, "Map-matching algorithms for robot self-localization: a comparison between perfect match, iterative closest point and normal distributions transform," *Journal of Intelligent & Robotic Systems,* vol. 93, no. 3, pp. 533-546, 2019.

[75]   P. Biber and W. Straßer, "The normal distributions transform: A new approach to laser scan matching," in *Proceedings 2003 IEEE/RSJ International Conference on Intelligent Robots and Systems (IROS 2003)(Cat. No. 03CH37453),* 2003, vol. 3: IEEE, pp. 2743-2748.

[76]   M. Lauer, S. Lange, and M. Riedmiller, "Calculating the perfect match: an efficient and accurate approach for robot self-localization," in *Robot Soccer World Cup*, 2005: Springer, pp. 142-153.

[77]   M. Magnusson, A. Lilienthal, and T. Duckett, "Scan registration for autonomous mining vehicles using 3D-NDT," *Journal of Field Robotics,* vol. 24, no. 10, pp. 803-827, 2007.

[78]   M. Magnusson, "The three-dimensional normal-distributions transform: an efficient representation for registration, surface analysis, and loop detection," Örebro universitet, 2009.

[79]   M. Jogan and A. Leonardis, "Robust localization using panoramic view-based recognition," in *Proceedings 15th International Conference on Pattern Recognition. ICPR-2000*, 2000, vol. 4: IEEE, pp. 136-139.

Included Paper

Gas Permeation Rates of Ultrathin Graphite Sealed SiO2 Cavities

Yan-Xin Liu[1], Hjalte Rørbech Ambjørner[1,2], Tobias G. Bonczyk[1], Edwin Dollekamp[1], Lau M. Kaas[1,2], Peter C. K. Vesborg[1,2]

[1]Surface Physics and Catalysis (SURFCAT), Department of Physics, Technical University of Denmark, DK-2800 Kgs. Lyngby, Denmark

[2]Center for Visualizing Catalytic Processes (VISION), Department of Physics, Technical University of Denmark, DK-2800 Kgs. Lyngby, Denmark

ABSTRACT

Despite the proven impermeability of graphene towards most standard gasses, graphene/graphite sealed SiO_2 cavities always exhibit a non-zero leak rate, and the physical leakage mechanism is still unclear. By measuring leak rates of different gases for the same cavities sealed by ultrathin graphite under identical conditions, we find that the leak rates generally depend on the kinetic diameter of the gas molecules, which implies that the leakage is caused by a molecular sieving mechanism. By comparing different samples, we find that the leak rate of any gas in a particular sample is well predicted by the leak rate of N_2 in that sample. In addition, we observe enhanced leak rates of water-soluble molecules. We infer that the leakage path (i.e., the graphene/graphite-SiO_2 interface) favors hydrophilic species.

In the past decade, several studies have shown that a graphene membrane is impermeable to most standard gasses[1-6], except for H_2 which may transfer through monolayer graphene[4]. When a cavity with gas is sealed by graphene on a SiO_2 substrate, with a typical mechanical exfoliation transfer method, the gas leakage path is most likely through the interface between the graphene membrane and the SiO_2 substrate[1, 7-9], although we note that for He and H_2, additional diffusion through the SiO_2 substrate is possible[1, 10].

Previous experiments showed initial evidence that the leak rates of different gas species depend on the kinetic diameter (denoted by d) of the gas molecules[2, 3]. Koenig et al.[2] measured the leak rates of H_2, CO_2, Ar, N_2 and CH_4. There was a leak rate difference of a factor of ~100 between N_2 ($d = 364$ pm) and H_2 ($d = 289$ pm), i.e. a leak rate selectivity of 100 between H_2 and N_2. Wang et al.[3] presented data of He, Ne, H_2, N_2O, CO_2, and Ar. The maximal selectivity in their dataset was between He ($d = 260$ pm) and Ar ($d = 340$ pm), which was about three orders of magnitudes. In this work, we expand the set of investigated gasses (N_2, O_2, CO, CO_2, Ar, H_2, He, CH_4, C_3H_6, NH_3, and SO_2) and make two primary findings: 1) For highly leak-tight samples there is a spread in the leak rates of multiple orders of magnitude from the least leaky gasses to the most leaky gasses, but they all scale in a deterministic way so a measurement of one gas allows estimation of the rest. 2) Water-soluble gasses tend to have enhanced leak rates and "memory effects". We see that exposure to reactive gasses can affect the future leak rate of un-reactive gasses.

In order to track the leak rates, we used a laser interference setup similar to those used in previously reported studies[1, 2, 7, 11-18] (see Supporting Information for details). Briefly, the laser setup uses an intensity modulated blue diode laser (405 nm) to excite a mechanical vibration of the suspended ultrathin graphite sheet covering a cavity, and

it also uses the interference of reflected light from a continuous-wave red HeNe laser (633 nm) to detect the resonance frequency of the graphite membrane. The resonance frequency is correlated to the tension of the graphite membrane, which depends on the pressure difference across it[1]. By measuring the pressure outside the cavity, we can thus obtain the pressure inside the cavity indirectly and observe how it changes over time.

Here, we present four samples (referred to as sample 1-4) to examine the leak rates of different gases. All the samples were fabricated from a single (100) silicon wafer but were cut into individual chips. Firstly, a 300 nm SiO_2 layer was grown by a wet thermal oxidation process. Then the structures of the cavities (4µm-diameter circle for sample 3, 5µm-diameter circle for sample 1, 2 and 4) were defined by a UV lithography process and the cavities were fabricated by performing a 300 nm deep reactive ion etch through the SiO_2 layer. The graphite membrane on sample 1, 2 and 3 were deposited by the typical mechanical exfoliation method[19, 20]. For sample 4, the graphite flake was transferred by the PDMS stamp method[21]. The thicknesses of the graphite flakes on the four samples are 5.9, 3.3, 1.6 and 3.6 nm respectively, as measured by an atomic force microscope operated in tapping mode across the edge of the flakes. The flake on sample 3 may be also called "multi-layer graphene"[22], but for consistency we use "ultrathin graphite" to refer to all the samples. Details of the transfer/exfoliation methods can be found in the Supporting Information.

Figure 1 illustrates our experimental process. After sealing in ambient air, the sample was measured in external vacuum, and a resonance frequency f_1 is obtained (Figure 1a). Then the samples were stored under vacuum for sufficiently long time (varying from days to a month, depending on their leak rates) in order to fully evacuate the cavities. A resonance frequency f_2 was then measured at 1 bar absolute external pressure (Figure 1b). Cavities must be essentially empty (i.e., full internal vacuum) if

f_2 and f_1 are roughly identical since in both cases there is 1 bar pressure difference across the graphite membrane. After this confirmation, the sample chamber was filled with the gas of interest to 1 bar absolute pressure. As the gas subsequently leaks in, the pressure difference, and thus the resonance frequency, is reduced. The total amount of gas leaked into the cavity can be calculated as a function of time from the frequency change $f_2 - f_3$(t) (Figure 1c). Between the measurement of the leak rate of different gases from the samples, the samples were stored under vacuum for sufficiently long time to ensure that the cavities were essentially empty at the start of each measurement.
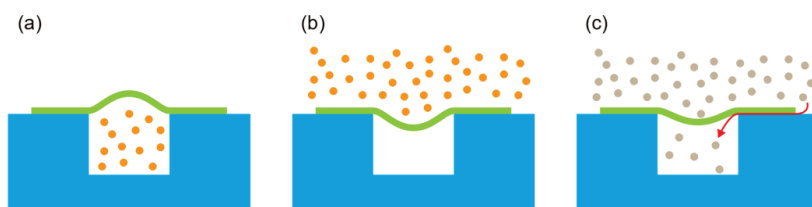

Figure 1. Schematic of the experiment process. (a) The initial state of the cavity, with 1 bar internal pressure where measurement of the resonance frequency under external vacuum gives f_1 corresponding to 1 bar Δp. (b) After evacuating the cavity, the cavity is measured with 1 bar external pressure, which yields a resonance frequency $f_2 \approx f_1$. (c) As time passes, gas leaks into the cavity and a new frequency f_3 is measured as a function of time.

To map the measured resonance frequency to the actual internal pressure inside the cavities, a simple calibration was used: Firstly, the gases in the samples were fully evacuated as verified by the method described above. Then, the sample chamber was filled with N_2 gas* to a given pressure between 0 bar to 1 bar absolute. A set of pressure-resonance frequency data were collected for the determination of the internal cavity

---

* N_2 is chosen for this calibration since it generally leaks very slowly and doesn't chemisorb or otherwise exhibit exotic behavior.

pressure via the resonance frequency[*]. Thanks to a small chamber volume (<10 cm^3) and an automatic tracking program, the entire pressure sweep calibration process can be done in less than one minute. For relatively slow-leaking samples, the leak during this calibration measurement is negligible since the samples need a much longer time (from one hour to one month) to be evacuated or to re-fill. For a fast-leaking sample (i.e., sample 4), we use average data from those slow-leaking samples with the same cavity dimension and similar graphite thickness as an estimate for the pressure-frequency relation (20 ± 5 mbar/MHz). Figure 2 shows an example of the correlation between the pressure difference and the resonance frequency of the suspended graphite membrane. The resonance frequency of the graphite membrane is theoretically proportional to the cubic root of the pressure difference across the graphite membrane[1], and indeed the 3rd-order fitting (green curve) matches the raw data well (see the green curve in Figure 2). However, since, by design, the experiments were mostly conducted at an Δp interval between 700 to 1000 mbar, a first order linear fit gives a good mapping of the frequency data to Δp as the red line shows. As we have both low-leak-rate samples and high-leak-rate samples whose third order fit cannot be obtained, for consistency reasons, we used the first order fit to calibrate the pressure and frequency for all the samples. In cases where we have to use data outside of the 700 to 1000 mbar interval (e.g., measuring a fast-leaking sample which can leak more than 300 mbar in a few seconds), the error of the fitting is included in the uncertainty of the leak rate calculation.

---

[*] For some samples, when the pressure difference is below a certain level (e.g., 400 mbar), the graphite membrane tension is low and sometimes an unambiguous resonance frequency signal cannot be obtained.
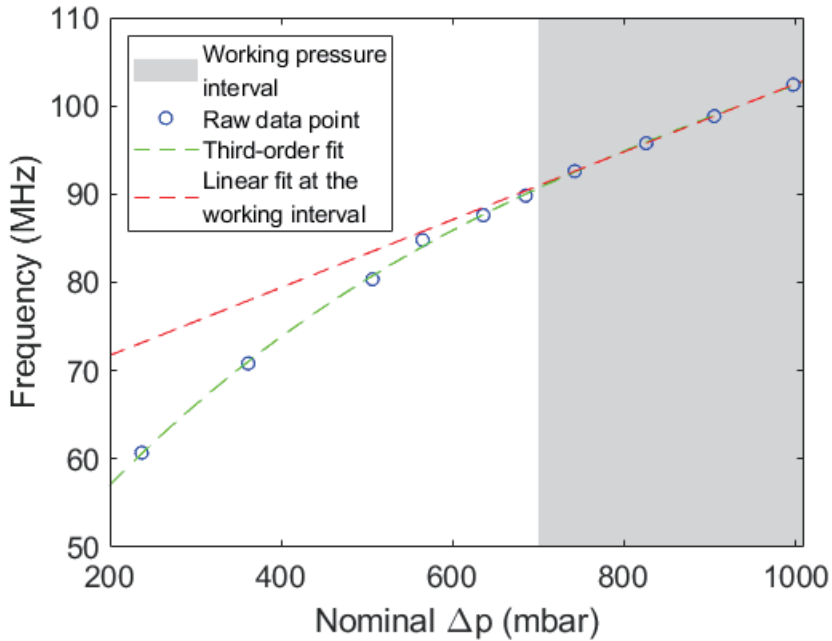
Figure 2. Pressure sweep of the cavity of sample 1 obtained by filling the sample chamber with N_2 at different pressures. The cavity was fully evacuated in the beginning of the sweep. Since the time constant for leakage is much longer than the pressure sweep experiment, the total N_2 ingression during the calibration data collection process is estimated to be less than 10 mbar.

In Figure 3, we present the measurements of N_2 leakage of sample 1 to illustrate how we calculated the leak rates from the raw data. Figure 3a shows how the resonance frequency changed over time. Figure 3b shows the leak rates calculated by both the first order fit and third order fit described above. Here, two different methods of calculating changes of pressure are also compared. The thin curves represent leak rates calculated from the pressure changes of adjacent points, and thus indicate real-time leak rates. The leak rates depicted with thick curves are calculated using the pressure difference between the first measurement and the measurement obtained at the point in time denoted by the x-axis, which indicates an average leak rate over the full period. The leak rate of a diffusion process is expected to be proportional to the (partial) pressure

difference[3, 9, 23], and thus there should be an exponential decay of the pressure difference when gas leaks into the cavity. However, from Figure 3b we can see that there is generally little change of the real-time leak rate as Δp covers interval from 1000 mbar to 700 mbar. The average leak rate evolves more smoothly than the real-time leak rate, while providing basically the same figure as the real-time leak rate. Furthermore, the results calculated for the first order fit and third order fit are comparable for the first 20 minutes (corresponding to the working pressure interval), which implies that it is reasonable to use the first order fit. The leak rates were calculated based on the average pressure change from t_0 as it provides a noise-free result.
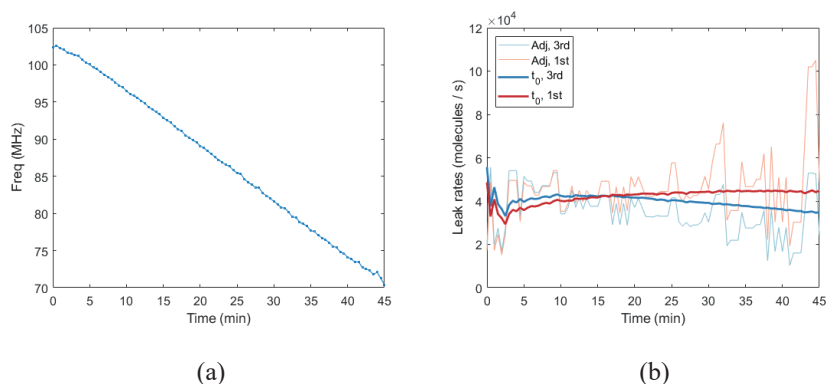

(a)   (b)

Figure 3. Measurement of N_2 leak rate of cavity 1. (a) The raw resonance frequency over time. (b) Calculated leak rates based on the frequency data. Adj, 3rd: calculated based on differences between adjacent data points with the third order fit. Adj, 1st: calculated based on differences between adjacent data points with the first order fit. t_0, 3rd: calculated based on differences from t_0 to the current data point with third order fit. t_0, 1st: calculated based on differences from t_0 to the current data point with first order fit.

Figure 4 shows the leak rates measured from the four samples. For sample 1, measurement of the leak rate of air (ca. 1.000 molecules/s, green point in Figure 4) before and after exposure to NH_3 showed a significant increase in leak rate for air (to ca. 40.000 molecules/s). At this point all gasses (N_2, O_2, etc.) were measured (blue

points in Figure 4). Then the sample was exposed to an SO_2/O_2 mix which again caused an increase in the leak rate of all gasses (orange points in Figure 4). Hence, both the leak rates before and after the O_2/SO_2 exposure are plotted here[*]. This memory effect of NH_3 or SO_2 exposure, however, is not universal since the other samples did not exhibit a significant change in leak rate after the same exposure. Details of the exposures and re-measurement can be seen in the Supporting Information.

For an overview of all the samples, by taking N_2 as a reference, we can see sample 1 (Figure 4a) is initially moderately leaky ($\sim 10^4$ molecules/s), sample 2 (Figure 4b), sample 3 (Figure 4c) are barely leaky (~ 100 molecules/s), and sample 4 (Figure 4d) is highly leaky ($\sim 10^6$ molecules/s). For the barely leaky samples, the leak rates of gases generally drop exponentially with increasing kinetic diameters of the gas molecules, except for the outlier SO_2 which exhibits much higher leak rates than the kinetic diameter-trend would suggest. Furthermore, we can also see a large span of leak rates (approximately 4 to 5 orders of magnitude) from the least leaky gas to the most leaky gas. For the moderately leaky sample 1, the correlation between leak rates and kinetic diameters is much weaker as NH_3, CO_2, SO_2, CH_4, and C_3H_6 leak faster than their counterparts with similar diameters or the general trend. In comparison with the barely leaky samples, the leak-rate span of sample 1 is reduced to 2 orders of magnitude. Lastly, for the highly leaky sample 4, the correlation between leak rates and kinetic diameters is further weakened by some outliers, such as SO_2, CH_4, and especially C_3H_6. Despite having the largest kinetic diameter of the gases tested, C_3H_6 somehow has the second-highest leak rate on this sample. In general, the leak-rate span of sample 4 is the lowest among all the samples with every gas equal to within a factor of 4.

---

[*] The SO_2 leak rate data shown in Figure 4 is from 99.98% SO_2 after the exposure of the O_2/SO_2 mixture.
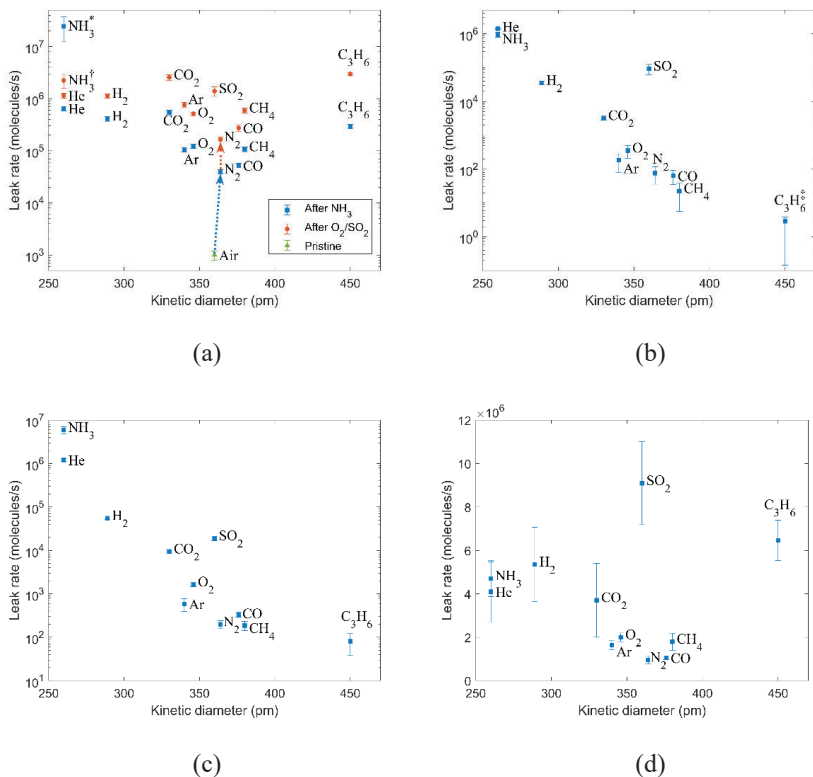
Figure 4. Leak rates of measured gases. Error bars are calculated based on the uncertainty of the frequency measurement. (a) Sample 1 (mechanical exfoliation). The leak rates changed significantly after being exposed to NH_3 and the O_2/SO_2 mixture. (b) sample 2 (mechanical exfoliation), (c) sample 3 (mechanical exfoliation), (d) sample 4 (PDMS)

Notes for special data points:

*: When measuring the NH_3 leak rate of sample 1 (before O_2/SO_2 exposure), the ΔP changed by 1 bar in less than the sampling time (~3s). Thus the plot represents a leak rate corresponding to 1 bar / 3 s.

†: The NH_3 leak of sample 1 (after O_2/SO_2 exposure) has an induction period. The leak rate was calculated based on the slope after the induction period.

‡: For the C_3H_6 leak rate of sample 2, we could detect no frequency change for 5 days. The point on the plot thus is based on the maximal uncertainty of the resonance frequency measurement and it is possible that the true leak rate is zero.

9

Limited data about the molecular leak rate selectivity of graphene/graphite sealed cavities can be found in literature[2, 3], as a benchmark of porous graphene sheets for molecular sieving studies. In these previous works, however, only a single cavity or cavities covered by a single flake was presented so sample-to-sample variation could not be assessed. Here, by comparing the results of four individual samples with different baseline leak rates (N_2), we can see a cavity whose N_2 leak rate is low tends to provide higher molecular selectivity for insoluble gases, and vice versa. We use N_2 as the baseline because it is inert and leaks relatively slowly. Although leaking faster than N_2, we see that O_2 also has a stable relative position in the trend line for relative leak rates. This means that for a freshly sealed new sample, a simple measurement of the air leak rate should be able to provide a good prediction of its leak rates for the standard gases.

The correlation between the leak rates and the kinetic diameters also indicates that the leakage may follow the molecular sieve mechanism[2, 3, 9, 24]. The permeability coefficient of the molecular sieve mechanism can be described by the following equation[9, 24]:

$$P = k_0 \left(\frac{8}{\pi M R T}\right)^{\frac{1}{2}} e^{\frac{-E_{gas}}{RT}} \tag{1}$$

where k_0 is the structural parameter related to the geometry of the pores and the sizes of the molecules (i.e., kinetic diameters), E_{gas} is the activation energy of the gas, which describes the interaction between the gas molecule and the pore wall (i.e., graphite and SiO_2), M is the molecular mass, T is the temperature, and R is the gas constant. In fact, the permeability coefficient is highly dominated by the parameters k_0 and E_{gas}. When the equation is applied to thin, porous membranes, E_{gas} can be estimated by the density functional theory calculations[23, 25]. In the case of leakage through the graphite-SiO_2 interface, it is however extremely challenging to calculate both k_0 and E_{gas}, as the leakage path can be long (a few μm), and the exact structure is unknown.

As the samples were exposed to reactive gases (e.g., SO_2 and NH_3), we repeated the measurements of certain gases to check if the gas species is the only factor that affects the leak rate. Details of the measurement sequence can be found in the Supporting Information. We observed that the leak rates of samples 2, 3, and 4 remain unchanged, whereas the leak rates of sample 1 had a dramatic change after exposure to NH_3 and SO_2.

Sample 1 showed a special phenomenon which differs from other samples shown here. As mentioned above, it initially had a relatively low air leak rate (~1000 molecules/s). However, after it was exposed to NH_3, its leak rate was increased by about an order of magnitude (taking N_2 and O_2 for comparison with the air leak rate). We were not able to track its exact NH_3 leak rate because NH_3 filled the cavity too fast, in less than 3 seconds, which is a comparable time for filling the sample chamber and performing the first measurement. After it was exposed to SO_2, we observed that the leak rate of NH_3 was reduced into a range that we can measure, whereas the leak rates of other gases had increased dramatically. The relative leak rates (i.e., the ratio of one gas to another gas) of all gases (other than NH_3) are, however, still comparable to their original rates. Such lasting effects of NH_3 and/or SO_2 exposure could perhaps be explained by a residual species inside the graphite-SiO_2 interface which are affected by NH_3 and SO_2. The alkaline or acidic gasses might for example interact with hydroxyl species on the SiO_2 surface and affect the van der Waal interaction between the chip and ultrathin graphite. Another noteworthy behavior of sample 1 is an induction period when NH_3 leaks into the cavity, which can be seen in Figure 5a. This was also observed in sample 2, after the O_2/SO_2 exposure. In Figure 5a, which shows data from sample 1, we can see that after the chamber was filled with NH_3, the resonance frequency of sample 1 (i.e., the internal pressure) remained stable for about 1.5 minutes (the

induction period) before starting a rapid decline. After the cavity was filled with 1 bar NH_3, we pumped down the chamber at $t = 4$ minutes. The NH_3 then started to leak out of the cavity, but in this case, there was no induction period so NH_3 started to leak out immediately. When we repeated this experiment, again filling the sample chamber with NH_3 shortly after the first experiment, the induction period for NH_3 ingression was reduced very significantly as Figure 5b shows. However, if instead of repeating the NH_3 exposure quickly, the sample is first kept under vacuum for an extended period (days), the original induction period occurs again. Clearly, the sample "remembers" the NH_3 exposure for some time - possibly due to NH_3 remaining bound under the graphite sheet interacting with the SiO_2 surface.
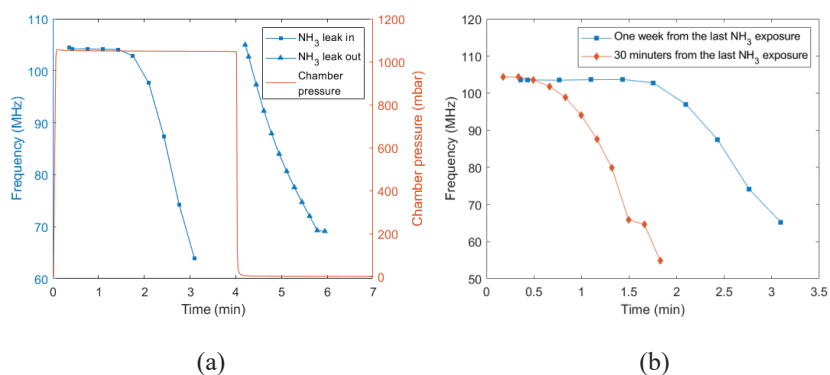

(a)   (b)

Figure 5. Induction behavior of sample 1 under NH_3 exposure. (a) co-plot of frequency and chamber pressure showing that (the first time after vacuum storage) there is a 1.5-minute delay from NH_3 exposure before frequency drop starts. (b) Comparison of the induction period recovery phenomenon for two different recovering times (vacuum storage). t=0 refers to the introduction of NH_3 in the sample chamber.

The enhanced leak rates of NH_3 and SO_2 (i.e., much higher than those of other gases with similar kinetic diameters), and the induction period of NH_3 could indicate that some kind of water-like layer or conduit network exists at the graphite-SiO_2 interface. At the time of graphite sealing, the SiO_2 surface is hydrophilic due to the oxygen plasma treatment. As we can see in these samples, water soluble gases (i.e.,

NH$_3$, SO$_2$ and perhaps CO$_2$) have higher leak rates than the non-soluble gases with similar kinetic diameters. Such gases might be able to "dissolve" into the graphite-SiO$_2$ interlayer at the chamber side, and re-evaporate at the cavity side facilitating mass-transport into the cavity. Such a water-like interlayer could explain the induction period seen for NH$_3$ leaks into the cavity and the changes of the leak rates. To recap the induction behavior, we start from the initial NH$_3$ leakage (Figure 6a). When the water-like interlayer is exposed to NH$_3$, NH$_3$ is dissolved at the chamber side, diffuses to the cavity side through the interlayer, and evaporates at the cavity side. After the sample was exposed to SO$_2$, HSO_3^- stays in the interlayer (Figure 6b). When NH$_3$ is dissolved in the interlayer, the acidic solution drives its dissociation balance ($NH_3 + H_2O \rightleftharpoons NH_4^+ + OH^-$) to the NH_4^+ side. During the induction period, most of the dissolved NH$_3$ molecules are converted to NH_4^+, which cannot evaporate into the cavity. Once all the sulfurous acid has been neutralized, the NH$_3$ concentration in the interlayer rises, and enhanced diffusion into the cavity can therefore be established (Figure 6c).
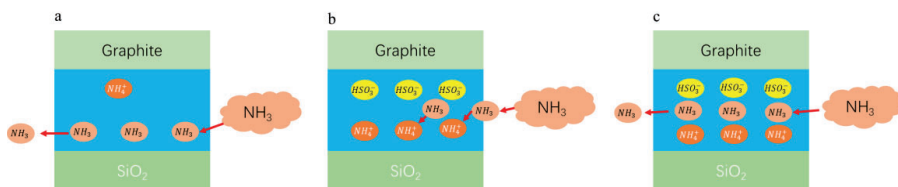

Figure 6. The interaction between NH$_3$ and SO$_2$. (a) The initial NH$_3$ leakage mechanism. NH$_3$ is dissolved at the chamber side and evaporates at the cavity side. Only a small amount of NH$_3$ is converted to NH_4^+. (b) After the SO$_2$ exposure, a significant amount of HSO_3^- stays in the water layer. Dissolved NH$_3$ is converted to NH_4^+, which causes the induction behavior. (c) When a balance between HSO_3^- and NH_4^+ is reached, NH$_3$ starts to evaporate at the cavity side.

In conclusion, we observed that the leak rates of most gas molecules permeating into graphite sealed SiO$_2$ cavities correlate with the kinetic diameters of the gas molecules. The molecular selectivity can be correlated with the N$_2$ leak rates, which

implies that the selectivity can be tunable by adjusting the baseline leak rate, for instance by changing graphite transfer method. In addition, we observe that water soluble molecules tend to have enhanced leak rates, which indicates that hydrated channels likely exist at the graphite-SiO_2 interface. Whether the water assists the sealing should be investigated in future research. Finally, hydrocarbon gases which ordinarily have very low leak rates showed high leak rates in certain cases. The reason for the occasional high hydrocarbon leak rate is unclear.

ACKNOWLEDGEMENTS

REFERENCES

1.   J. S. Bunch, S. S. Verbridge, J. S. Alden, A. M. Van Der Zande, J. M. Parpia, H. G. Craighead and P. L. McEuen, Nano letters **8** (8), 2458 (2008).

2.   S. P. Koenig, L. Wang, J. Pellegrino and J. S. Bunch, Nature nanotechnology **7** (11), 728 (2012).

3.   L. Wang, L. W. Drahushuk, L. Cantley, S. P. Koenig, X. Liu, J. Pellegrino, M. S. Strano and J. S. Bunch, Nature nanotechnology **10** (9), 785 (2015).

4.   P. Sun, Q. Yang, W. Kuang, Y. Stebunov, W. Xiong, J. Yu, R. Nair, M. Katsnelson, S. Yuan, I. Grigorieva, M. Lozada-Hidalgo, F. Wang and A. Geim, Nature **579** (7798), 229 (2020).

5.   V. Berry, Carbon **62**, 1 (2013).

6.   O. Leenaerts, B. Partoens and F. Peeters, Applied Physics Letters **93** (19), 193107 (2008).

7.   M. Lee, D. Davidovikj, B. Sajadi, M. Šiškins, F. Alijani, H. S. van der Zant and P. G. Steeneken, Nano letters **19** (8), 5313 (2019).

8.   Y. Manzanares-Negro, P. Ares, M. Jaafar, G. Lopez-Polin, C. Gomez-Navarro and J. Gomez-Herrero, ACS Applied Materials & Interfaces **12** (33), 37750 (2020).

9.   T. Tsuru, R. Igi, M. Kanezashi, T. Yoshioka, S. Fujisaki and Y. Iwamoto, AIChE journal **57** (3), 618 (2011).

10.   R. Lee, R. Frank and D. Swets, The Journal of Chemical Physics **36** (4), 1062 (1962).

11.   J. S. Bunch, A. M. Van Der Zande, S. S. Verbridge, I. W. Frank, D. M. Tanenbaum, J. M. Parpia, H. G. Craighead and P. L. McEuen, Science **315** (5811), 490 (2007).

12.   S. P. Koenig, N. G. Boddeti, M. L. Dunn and J. S. Bunch, Nature

nanotechnology **6** (9), 543 (2011).

13.   A. Castellanos‑Gomez, R. van Leeuwen, M. Buscema, H. S. van der Zant, G. A. Steele and W. J. Venstra, Advanced Materials **25** (46), 6719 (2013).

14.   D. Davidovikj, M. Poot, S. J. Cartamil-Bueno, H. S. van der Zant and P. G. Steeneken, Nano letters **18** (5), 2852 (2018).

15.   D. Davidovikj, J. J. Slim, S. J. Cartamil-Bueno, H. S. van der Zant, P. G. Steeneken and W. J. Venstra, Nano letters **16** (4), 2768 (2016).

16.   R. J. Dolleman, D. Davidovikj, S. J. Cartamil-Bueno, H. S. van der Zant and P. G. Steeneken, Nano letters **16** (1), 568 (2015).

17.   R. J. Dolleman, S. Houri, D. Davidovikj, S. J. Cartamil-Bueno, Y. M. Blanter, H. S. van der Zant and P. G. Steeneken, Physical Review B **96** (16), 165421 (2017).

18.   R. J. Dolleman, S. J. Cartamil-Bueno, H. S. van der Zant and P. G. Steeneken, 2D Materials **4** (1), 011002 (2016).

19.   K. S. Novoselov, A. K. Geim, S. V. Morozov, D.-e. Jiang, Y. Zhang, S. V. Dubonos, I. V. Grigorieva and A. A. Firsov, science **306** (5696), 666 (2004).

20.   K. S. Novoselov, D. Jiang, F. Schedin, T. Booth, V. Khotkevich, S. Morozov and A. K. Geim, Proceedings of the National Academy of Sciences **102** (30), 10451 (2005).

21.   A. Castellanos-Gomez, M. Buscema, R. Molenaar, V. Singh, L. Janssen, H. S. Van Der Zant and G. A. Steele, 2D Materials **1** (1), 011002 (2014).

22.   A. Bianco, H.-M. Cheng, T. Enoki, Y. Gogotsi, R. H. Hurt, N. Koratkar, T. Kyotani, M. Monthioux, C. R. Park, J. M. D. Tascon and J. Zhang, Carbon **65**, 1 (2013).

23.   S. Blankenburg, M. Bieri, R. Fasel, K. Müllen, C. A. Pignedoli and D. Passerone, Small **6** (20), 2266 (2010).

24.   A. Shelekhin, A. Dixon and Y. Ma, AIChE Journal **41** (1), 58 (1995).

25.   J. P. Thiruraman, S. A. Dar, P. Masih Das, N. Hassani, M. Neek-Amal, A. Keerthi, M. Drndić and B. Radha, Science Advances **6** (51), eabc7927 (2020).

Supporting Information

Gas Permeation Rates of Ultrathin Graphite Sealed SiO₂ Cavities

Yan-Xin Liu[1], Hjalte Rørbech Ambjørner[1,2], Tobias G. Bonczyk[1], Edwin Dollekamp[1], Lau M. Kaas[1,2], Peter C. K. Vesborg[1,2]

[1]Surface Physics and Catalysis (SURFCAT), Department of Physics, Technical University of Denmark, DK-2800 Kgs. Lyngby, Denmark

[2]Center for Visualizing Catalytic Processes (VISION), Department of Physics, Technical University of Denmark, DK-2800 Kgs. Lyngby, Denmark

S1.   Optical images of the samples

Figure S1. Optical image of the four samples. The pictures were taken after the final SO_2 and NH_3 measurement. Residuals resulting from the two gases can be seen on the surface of sample 1.

S2. Graphite transfer

The graphite on sample 1-3 was transferred by the mechanical exfoliation method[1,2]. The samples were first cleaned in an acetone sonication bath. Then we used an oxygen plasma cleaner (Plasma Etch, PE-50) to further remove residuals on the sample surface. Graphite flakes were cleaved from natural graphite crystals (NGS Graphite, flaggy flakes) by using Scotch tape. Then the graphite flakes were exfoliated onto the sample substrate directly after the oxygen plasma cleaning process by pressing the piece of scotch tape with graphite flakes against the sample surface using a thumb.

Sample 4 has a graphite flake transferred to it using a polydimethylsiloxane (PDMS) stamp method[3], which provides an all-dry and deterministic transfer. The sample was not cleaned by sonication or oxygen plasma. A graphite flake was cleaved from the same graphite source as used for sample 1-3, but with Nitto tape instead of Scotch tape. A stamp was made by placing a piece of PDMS gel (Gel-Pak®) on a clean microscope slide. The graphite flake was exfoliated onto the PDMS stamp by contacting the Nitto tape with the stamp. Then the stamp and the sample were aligned under an optical microscope. Finally, the graphite flake was transferred to the sample substrate by slowly lowering the stamp to the sample surface until a firm contact was formed.

S3. Optical setup

Figure S2 depicts our laser interferometry setup. It uses a 633 nm HeNe laser to detect the vibration of the graphite membrane. The laser beam passes through a polarizing beam splitter and a quarter-wave plate, which forms an isolator and can redirect the reflected beam to an avalanche photodetector (Thorlabs APD430A). A 405 nm blue laser (Sanyo DL-5146-101S) is used to excite the vibration of the graphite membrane. The frequency of the violet laser is

modulated by a spectrum analyzer (Rohde & Schwartz FPC1500). The red and violet laser

beams are coupled by a dichroic mirror. An electrical shutter is placed after the dichroic mirror

to control the laser exposure. A 50x objective lens focuses the beam on the sample which is

placed in a sample chamber. The pressure in the chamber is monitored by a pressure transducer.

The chamber can also be evacuated by a vacuum pump and filled with different gases from the
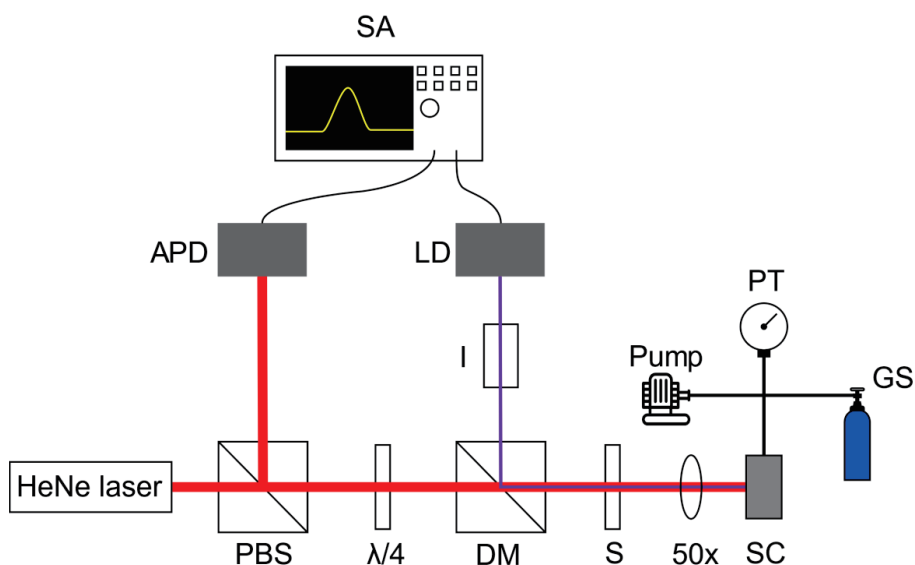
gas supply.

Figure S2. The laser interferometry setup. SA: spectrum analyzer, APD: avalanche photodetector, LD: laser diode,
PBS: polarizing beam splitter, DM: dichroic mirror, S: shutter, SC: sample chamber, PT: pressure transducer, GS:
gas supply, I: Isolator.

S4. Consistency of the samples leak rate during the measurement period

The measurements of all the samples and gases were taken over a period of four months. To

ensure the leak rates are consistent over time, we repeated the measurements of certain gases.

Table S1 shows the full sequence of our measurement of all the gases. The O_2/SO_2 mixture

was made by heating sulfur in O_2 at 250 °C for 60 minutes. The actual proportion of the mixture was not examined but we verified that a significant amount of SO_2 was generated by testing the pH of the product gas in a water solution. Figure S3 shows the leak rates of the gases that were measured multiple times. Sample 2, 3, and 4 have generally no drift of the leak rates over the period, whereas sample 1 has significant change as described in the main article. However, all samples tend to produce a lower resonance signal after the final NH_3 and SO_2 measurement. This might result from the reaction of NH_3 and SO_2 with moisture, which deposited ammonium sulfite on the graphite membrane and damped the resonance.

Table S1. Measurement sequence of the gases and samples. Experimental chronology is from top to bottom. Dataset 1 is the original sample. Dataset 2 is after NH_3 exposure. Dataset 3 is after O_2/SO_2 mixture exposure (the same gas mixture is used for all the four samples). Dataset 4 is after SO_2 exposure.

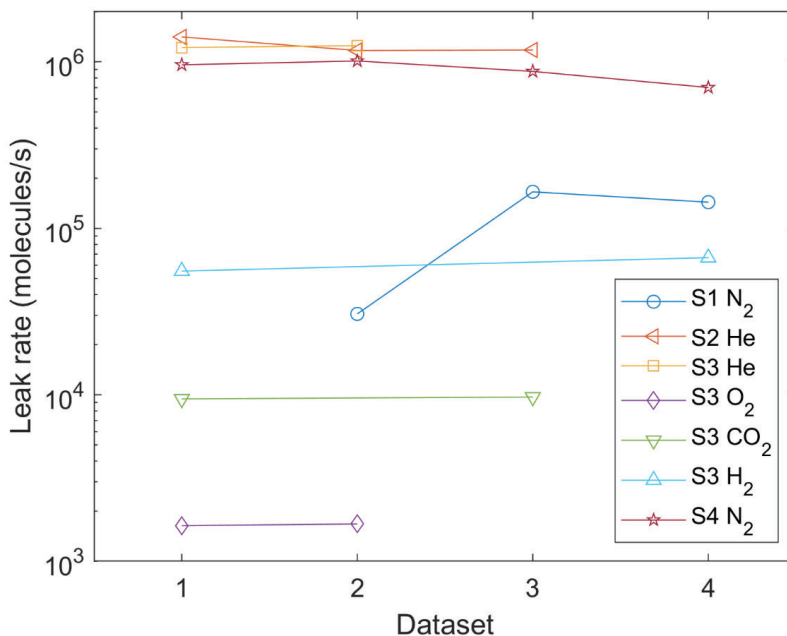|		Sample			Dataset
	1	2	3	4	
	air	C_3H_6	He	N_2	
		CH_4	H_2	CO	
		CO_2	N_2	O_2	
		N_2	C_3H_6	CO_2	
		O_2	CH_4	Ar	1
		CO	O_2	CH_4	
		Ar	CO	H_2	
		He	Ar	He	
		H_2	CO_2		
	NH_3	**NH_3**	**NH_3**	**NH_3**	
	Air				
	N_2	He	He	C_3H_6	
	O_2			N_2	
	CO				
	CO_2				
Gas	Ar				2
	H_2				
	He				
	CH_4				
	C_3H_6				
	O_2/SO_2	**O_2/SO_2**	**O_2/SO_2**	**O_2/SO_2**	
	N_2	NH_3	NH_3	N_2	
	NH_3	He	CO_2		
	O_2	H_2			
	CO				
	CO_2				3
	Ar				
	H_2				
	He				
	CH_4				
	C_3H_6				
	SO_2	**SO_2**	**SO_2**	**SO_2**	
	N_2	NH_3	H_2	N_2	4
	NH_3		NH_3	NH_3	

Figure S3. Comparison of the leak rates from different measurements. S*x* in the legend represents sample *x*.

S5.   Data Availability

The data that supports the findings of this study are available at the DTU data repository[4].

S6.   References

1   Kostya S Novoselov, Andre K Geim, Sergei V Morozov, De-eng Jiang, Yanshui Zhang, Sergey V Dubonos, Irina V Grigorieva, and Alexandr A Firsov, science **306** (5696), 666 (2004).

2   Kostya S Novoselov, D Jiang, F Schedin, TJ Booth, VV Khotkevich, SV Morozov, and Andre K Geim, Proceedings of the National Academy of Sciences **102** (30), 10451 (2005).

3   Andres Castellanos-Gomez, Michele Buscema, Rianda Molenaar, Vibhor Singh,

Laurens Janssen, Herre SJ Van Der Zant, and Gary A Steele, 2D Materials **1** (1), 011002 (2014).

4   DOI:10.11583/DTU.20536053